

Utah State University

DigitalCommons@USU

All Graduate Theses and Dissertations

Graduate Studies

12-2008

Pulse-Laser Infrared Photothermal Spectrometry of Condensed-Phase Aerosols Based on Photothermal Deflection Spectroscopy

Oluwatosin Olubunmi Dada
Utah State University

Follow this and additional works at: <https://digitalcommons.usu.edu/etd>

 Part of the [Analytical Chemistry Commons](#)

Recommended Citation

Dada, Oluwatosin Olubunmi, "Pulse-Laser Infrared Photothermal Spectrometry of Condensed-Phase Aerosols Based on Photothermal Deflection Spectroscopy" (2008). *All Graduate Theses and Dissertations*. 52.

<https://digitalcommons.usu.edu/etd/52>

This Dissertation is brought to you for free and open access by the Graduate Studies at DigitalCommons@USU. It has been accepted for inclusion in All Graduate Theses and Dissertations by an authorized administrator of DigitalCommons@USU. For more information, please contact digitalcommons@usu.edu.



PULSE-LASER INFRARED PHOTOTHERMAL SPECTROMETRY OF
CONDENSED-PHASE AEROSOLS BASED ON PHOTOTHERMAL
DEFLECTION SPECTROSCOPY

by

Oluwatosin O. Dada

A dissertation submitted in partial fulfillment
of the requirements for the degree

of

DOCTOR OF PHILOSOPHY

in

Chemistry

Approval signatures:

Stephen E. Bialkowski
Major Professor

Roger A. Coulombe
Committee Member

Alvan C. Hengge
Committee Member

Robert S. Brown
Committee Member

Philip J. Silva
Committee Member

Byron Burnham
Dean of Graduate Studies

UTAH STATE UNIVERSITY
Logan, Utah
2008

Copyright © Oluwatosin O. Dada
All rights Reserved

ABSTRACT

Pulse-Laser Infrared Photothermal Detection of Condensed-Phase Aerosols Based on
Photothermal Deflection Spectroscopy

by

Oluwatosin O. Dada, Doctor of Philosophy

Utah State University, 2008

Major Professor: Stephen E. Bialkowski
Department: Chemistry and Biochemistry

The research reported in this dissertation is aimed at development of photothermal deflection detector that is consistent with constraints imposed by aerosols sampling and analysis. The main objectives of this project are: 1) the design and evaluation of initial apparatus prototypes and 2) a test of the prototype apparatus with surrogate substances using conventional mid-infrared gas lasers.

Experimental evaluation of reduced size photothermal apparatus is first performed with gaseous samples. Analysis of trichlorofluoromethane (CFC-11) and ethanol vapors is performed with both conventional large apparatus and the prototype small apparatus. Comparison studies in terms of photothermal signal from both apparatuses are carried out to examine how apparatus downscaling affects photothermal signal. The main result indicates that the small apparatus performs about the same as the conventional laboratory-size apparatus.

For better understanding of heat transport from aerosols collect on a flat substrate and its surrounding media, a numerical methodology based on finite element analysis is used to investigate the heat transfer between aerosol, substrate, and air. The numerical modeling is extended to prediction of photothermal signals from laser excited optical beam deflection due to temperature gradient inside the air above aerosols. The modeling results help to understand how aerosol properties such as size, shape, thermo-optical properties, and particles arrangement affect photothermal signal. The model is also used to investigate the influence of substrate properties on photothermal signal.

A photothermal deflection apparatus is then used to examine the potential of mid-infrared photothermal spectroscopy for aerosol analysis. Laboratory-generated ammonium nitrate aerosols are deposited on germanium substrate by using Micro-Orifice Uniform Deposits Impactor (MOUDI). Photothermal spectroscopy, based on optical beam deflection (mirage effect), is used to analyze the collected aerosols. The measurements are carried out in terms of aerosol number concentration and aerosol mass concentration. Based on standard 30 minutes sampling time and 30 L/min flow rate, the limit of detection obtained for our instrument are 18 particles, equivalence of $0.2 \mu\text{g m}^{-3}$ mass concentrations for $3 \mu\text{m}$ particles diameter) for aerosol number concentration measurement and $0.65 \mu\text{g m}^{-3}$ for aerosol mass concentration measurement.

Out of curiosity on whether standard materials could be used to calibrate a photothermal lens apparatus without having to make up liquid samples, it was thought that colored glass filters would serve as such standards. Photothermal lens measurements and finite element modeling are used to examine the physical changes taking place in

optical filter glasses. Colored-glass and neutral density filters are found to have a strong positive temperature-dependent refractive index change.

(194 pages)

ACKNOWLEDGMENTS

My first appreciation goes to the almighty God for His grace and mercy throughout the entire period of my graduate studies. The success of this research (PhD program) is largely due to the support and encouragement from my major advisor, Prof. Stephen Bialkowski. He is the best kind of mentor I could imagine. Without his smartness, patience, and kindness, it would have been difficult for me to scale through the huddles associated with PhD program. The vast of the ideas reported in this dissertation are facilitated by him. I think I have enjoyed chemistry, especially analytical chemical spectroscopy, because of the freedom he gave me as a student in his laboratory. Thank you, Stephen, for allowing me to grow and learn under your supervision.

I am very grateful to all my advisory committee members, Prof. Alvan Hengge, Prof. Roger Coulombe, Dr. Robert Brown, and Dr. Philip Silva. I thank you all for your time and effective guidance during my education at Utah State University. I would especially thank Dr. Silva for giving me the access to his laboratory equipment. This kind gesture made his laboratory look to me like my second research laboratory. I must thank Dr. Brown for those times he spent sharing his ideas, which today has contributed to my knowledge in analytical chemistry. I cannot forget the tremendous role played by Prof. Alvan Hengge during the process of my coming to Utah State University in 2004. His correspondence with the United States embassy in Nigeria really helped me in that same year. Prof. Coulombe is one of the coolest professors I have met. From Environmental Toxicology (ADVS 6400) class to graduate committee meetings, he has shown to me

how nice it is to know someone like him. I am honored to say that all of you in my graduate committee are unique and have contributed immensely to my achievement.

I would also like to thank Prof. Joel Harris of the Chemistry Department, the University of Utah, for the use of his laboratory equipment, especially the use of his Confocal Microscope. I want to thank Prof. Ikenna Onyido for his fatherly care during my PhD research. I thank him especially for the confidence he had in me and his advice whenever he visited Logan.

The closest person to me during the course of my PhD work is my wife, Oluwatosin Omolara Dada. Honey, you are precious and invaluable. Without your cooperation I would not enjoy chemistry as much as I do. Women like you are scarce. I appreciate your understanding, endurance, and support throughout the period of my studies at Utah State University. I would like this sincere gratitude to flow from you to my children, Mercy Dada and Grace Dada. I love you all.

I cannot but mention the people who initiated my education, I mean my parents, Mr. Adebayo Dada and Mrs. Modupe Dada. I thank them for their support for making me who I am today. I also use this opportunity to express my gratitude to the people I spent most of my childhood with. I wish they (the late Madam Felicia Olurin and the late Madam Abigail Olurin) were alive to witness what they have labored so much for. The values they impacted in me have helped me to be above those circumstances that could have jeopardized my achievement.

I would like to thank many people who have helped in making this dissertation research a success, especially Ron and Karen Flessner for offering their great service of

love to look after my babies when my wife and I are not available. Ron and Karen were there to answer my calls anytime I need help with my schedule. I say special thank you to them. I must acknowledge my co-graduate students in the Chemistry and Biochemistry department, especially Prokash Joshi and Mark Erupe for their companionship and time we spent together discussing science.

Finally I would like to thank the Department of Chemistry and Biochemistry, Utah State University for the opportunity to study at Utah State University and their support in the form of a teaching assistantship and research assistantship, 2004-2008. I wish to acknowledge the Space Dynamic Laboratory Enabling Technologies Program for supporting this project.

I can truly say I have enjoyed the entire period of my program in the department of Chemistry and Biochemistry, Utah State University. I know there are many people to thank that I could not mention their names; I hope they still know that I owe them one.

To all of you, I say thank you.

Oluwatosin O. Dada

CONTENTS

	Page
ABSTRACT.....	iii
ACKNOWLEDGMENTS.....	vi
CONTENTS.....	ix
LIST OF TABLES.....	xiii
LIST OF FIGURES.....	xiv
LIST OF ABBREVIATIONS.....	xxii
CHAPTERS	
1. INTRODUCTION.....	1
AEROSOLS.....	2
Basic Information.....	2
Regulatory Standards.....	4
Cache Valley Particle Pollution.....	4
Photothermal Spectroscopy.....	4
FINITE ELEMENT ANALYSIS MODELING OF PHOTOTHERMAL PHENOMENON.....	9
ORGANIZATION OF THE REMAINING CHAPTERS.....	10
REFERENCE.....	12
2. CONSTRUCTION AND EVALUATION OF PROTOTYPED PHOTOTHERMAL APPARATUS BASED ON PHOTOTHERMAL DEFLECTION IN A SMALL CONFIGURATION.....	15
ABSTRACT.....	15
INTRODUCTION.....	15
THEORY.....	19
EXPERIMENTAL.....	21
Large Size Apparatus.....	21
Small Size Apparatus.....	24
Samples.....	26
Procedures for Finite Element Analysis Modeling.....	26

RESULTS AND DISCUSSION.....	27
CONCLUSION.....	34
REFERENCES.....	35
3. FINITE ELEMENT ANALYSIS MODELING OF PULSE-LASER EXCITED PHOTOTHERMAL DEFLECTION (MIRAGE EFFECT) FROM AEROSOLS.....	38
ABSTRACT.....	38
INTRODUCTION.....	39
MATERIALS AND METHOD.....	43
Temperature Change Profile.....	43
Optical Beam Deflection.....	47
RESULTS AND DISCUSSION.....	48
Aerosols Optical Absorption.....	50
Thermal Diffusion.....	51
Aerosols Size and Shape.....	55
Aerosols Thermal Properties.....	60
Substrate Thermal Properties.....	65
Multiple Particle Deposit.....	69
Chopped Continuous Wave Excitation.....	75
CONCLUSION.....	81
REFERENCES.....	81
4. AEROSOLS GENERATION AND SAMPLING.....	84
ABSTRACT.....	84
INTRODUCTION.....	84
MATERIALS AND METHOD.....	86
Aerosol Generation Apparatus.....	86
Impactor Sampling in Photothermal Spectroscopy.....	88
RESULTS AND DISCUSSION.....	91
Rotating and Non-Rotating Impaction.....	91
Chemical Identification of Aerosols with Confocal Raman Microscopy.....	94

	Confocal Microscope.....	95
	Results from Raman Measurement.....	97
	CONCLUSION.....	99
	REFERENCES.....	99
5.	DEVELOPMENT OF INFRARED PHOTOTHERMAL DEFLECTION SPECTROSCOPY (MIRAGE EFFECT) FOR ANALYSIS OF CONDENSED-PHASE AEROSOLS COLLECTED IN A MICRO-ORIFICE UNIFORM DEPOSIT IMPACTOR.....	101
	ABSTRACT.....	101
	INTRODUCTION.....	102
	THEORY.....	104
	EXPERIMENTAL.....	105
	RESULTS AND DISCUSSION.....	108
	Aerosols Mass Concentration Measurements.....	108
	Rotating and Non-rotating Sampling.....	109
	Aerosols Mass Calibration.....	114
	Aerosols Number Concentration Measurements.....	120
	Aerosol “Pile-up” Correction.....	124
	Aerosols Number Calibration.....	126
	CONCLUSION.....	128
	REFERENCES.....	129
6.	CONTINUOUS LASER-EXCITED PHOTOTHERMAL SPECTROMETRY OF CdS _x Se _{1-x} DOPED GLASSES.....	133
	ABSTRACT.....	133
	INTRODUCTION.....	134
	THEORY.....	136
	EXPERIMENTAL.....	140
	Thermal Lens Apparatus.....	140
	Finite Element Analysis.....	143
	Samples.....	145

RESULTS AND DISCUSSION	145
CONCLUSION.....	153
REFERENCES.....	154
7. SUMMARY.....	156
APPENDIX.....	160
APPENDIX A: Figure Data.....	161
APPENDIX B: Dynamic Gas Mixer Operation.....	162
APPENDIX C: Comsol Multiphysics Files.....	164
APPENDIX D: Step-by-step Procedure for Aerosol Generation.....	165
APPENDIX E: Permission Letters.....	167
CURRICULUM VITAE.....	169

LIST OF TABLES

Table	Page
3-1. Materials and their thermal properties as found in literature.....	47
4-1. Nominal cut-off size and number of nozzles of MOUDI stages.....	89
6-1. Thermo-optical constants for glass filters.....	151

LIST OF FIGURES

Figure	Page
1-1. An early photothermal deflection apparatus for measuring absorbance of earth's surface. Reprinted with permission from S. E. Bialkowski, 1996. Copyright 1996, John Wiley and Sons.....	8
2-1. Schematic diagram of conventional large size photothermal deflection apparatus: Apparatus foot print is about 1 square meter not including the CO ₂ laser. Distance from the centre of the sample cell to the PSD is about 254 mm. L-Lens, EM-Energy monitor, PSD-Position sensor detector, BS-Beam splitter, BA-Beam attenuator, A/D-Analog-to-Digital Converter.....	22
2-2. Schematic diagram of small size photothermal deflection apparatus: OPM-Off axis parabolic mirror, EM-Energy monitor, PSD-Position sensing detector, BS-Beam splitter, BA-Beam attenuator, A/D-Analog-to-Digital converter. Distance from the center of the sample cell to the PSD is about 30 mm.....	24
2-3. Image of the prototype small-size photothermal deflection apparatus with footprint of about 0.01 m ²	25
2-4. Finite element analysis result for time dependent photothermal deflection signal: — large size apparatus model signal, — small size apparatus model signal with a gaussian irradiance. Analyte concentrations are assumed the same.....	29
2-5. Large size apparatus energy dependent photothermal signal for: (a) 1 ppmv CFC-11 buffered in nitrogen. (b) 1.5 ppmv 200 % proof ethanol vapor buffered in nitrogen. Excitation wavelength is at 9.3 μm for CFC-11 and 9.54 μm for ethanol. Sample pathlength is 100 mm.....	31
2-6. Small size apparatus energy dependent photothermal signal for: (a) 5 ppmv CFC-11 buffered in nitrogen, (b) 10 ppmv 200 % proof ethanol vapors in nitrogen. Excitation wavelength is at 9.3 μm for CFC-11 and 9.54 μm for ethanol. Sample pathlength is 37 mm.....	32

2-7.	Experimental time dependent photothermal deflection signal for: large size apparatus time dependent photothermal deflection angle for 1ppmv CFC-11 in nitrogen at 9.3 μm excitation wavelength (black curve), and small size apparatus time dependent photothermal deflection angle for 5 ppmv CFC-11 buffered in nitrogen at 9.3 μm excitation wavelength (gray curve). Pulse energy is 0.8 mJ.....	34
3-1.	Air-aerosol-substrate layers thermal field geometry: The backing is a flat germanium plate which is used to collect aerosols. The deflection angle is measured with a bi-cell position sensing detector.....	43
3-2.	Finite element model 3D geometry representing air, aerosol, substrate layers. The geometry shows a spherical aerosol deposited on a flat substrate and the surrounding air.....	44
3-3.	Plot of probed time-dependent temperature change along x -axis for ammonium nitrate aerosols on germanium plate. The inset is the corresponding photothermal deflection signal (path integral of temperature change first derivative with respect to z).....	49
3-4.	(A) Time-dependent temperature change and, (B) the resulting time-dependent photothermal deflection signal at 10 μm above aerosol following first seven excitation pulses with irradiance $E = 3000 \text{ W m}^{-2}$ at 50 kHz repetition rate. The real signal magnitude is about six orders of magnitude larger than the temperature change magnitude.....	50
3-5.	Plot of theoretical photothermal deflection signal (maximum time-dependent photothermal deflection magnitude) with aerosols optical absorption coefficient.....	51
3-6.	Time-dependent temperature change for ammonium nitrate aerosols on germanium substrate at the aerosol's entrance surface ($z = -1 \mu\text{m}$, $x = y = 0$).....	52
3-7.	Time-dependent temperature change for ammonium nitrate aerosols on germanium substrate at distance $z = 10 \mu\text{m}$ above aerosol and $z = 10 \mu\text{m}$ into substrate from top down.....	53
3-8.	Adjusted temperature profile along z -axis at $t = 2 \mu\text{s}$ following pulse laser heating, distance $z = -1 \mu\text{m}$ is aerosol's top surface for: I. high absorbance aerosol, $\alpha = 2.676 \times 10^7 \text{ m}^{-1}$; II. low absorbance aerosol, $\alpha = 2676 \text{ m}^{-1}$. (particle diameter = 2 μm , irradiance, $E = 3000 \text{ W m}^{-2}$).....	54

- 3-9. Transverse temperature change profile along x -axis at $z = 6 \mu\text{m}$ above aerosol for both high absorbance aerosol $\alpha = 2.676 \times 10^7 \text{ m}^{-1}$ and low absorbance aerosol $\alpha = 2676 \text{ m}^{-1}$ (particle diameter = $2 \mu\text{m}$, irradiance, $E = 3000 \text{ W m}^{-2}$).....55
- 3-10. The plot of theoretical photothermal deflection signal (maximum time-dependent photothermal deflection magnitude) with aerosol's diameter for ammonium nitrate aerosols on germanium plate showing the effects of aerosol's size on photothermal signal for low absorbance, $\alpha = 2676 \text{ m}^{-1}$, aerosol. Irradiance, $E = 3000 \text{ W m}^{-2}$57
- 3-11. Plot of theoretical photothermal deflection signal (maximum time-dependent photothermal deflection magnitude) with aerosol's diameter for ammonium nitrate aerosols on germanium plate showing the effects of aerosol's size on photothermal signal for high absorbance, $\alpha = 2.676 \times 10^7 \text{ m}^{-1}$, aerosol. Irradiance, $E = 3000 \text{ W m}^{-2}$58
- 3-12. Time-dependent photothermal deflection signal for: ■ Spherical aerosol
 Δ prolate aerosol, ● oblate aerosol.....59
- 3-13. The plot of time-dependent photothermal deflection signal showing the effects of aerosol's heat capacity for different ratio of aerosol's heat capacity to heat capacity of air with low absorbance aerosols; — 0.1, ■ 0.5, Δ 1, ● 5, \square 10 ($k_s = 59.8 \text{ W m}^{-1}\text{K}^{-1}$, $C_{ps} = 320 \text{ J kg}^{-1} \text{ K}^{-1}$, $\rho_s = 5330 \text{ kg m}^{-3}$, $k_p = 1.8 \text{ W m}^{-1} \text{ K}^{-1}$, $\rho_p = 1720 \text{ kg m}^{-3}$, $k_a = 0.0261 \text{ W m}^{-1} \text{ K}^{-1}$, $C_{pa} = 1010 \text{ J kg}^{-1} \text{ K}^{-1}$, and C_{pp} is varied relative to C_a . where subscripts p , s , and a stand for particle, substrate, and air. Irradiance, $E = 3000 \text{ W m}^{-2}$).....61
- 3-14. The plot of time-dependent photothermal deflection signal showing the effects of aerosol's thermal conductivity for different ratio of aerosol's thermal conductivity to thermal conductivity of air with low absorbance aerosols; \square 1, ● 10, Δ 100, ■ 1000, — 10000 ($k_s = 59.8 \text{ W m}^{-1}\text{K}^{-1}$, $C_{ps} = 320 \text{ J kg}^{-1} \text{ K}^{-1}$, $\rho_s = 5330 \text{ kg m}^{-3}$, $C_{pp} = 1740 \text{ J kg}^{-1} \text{ K}^{-1}$, $\rho_p = 1720 \text{ kg m}^{-3}$, $k_a = 0.0261 \text{ W m}^{-1} \text{ K}^{-1}$, $C_{pa} = 1010 \text{ J kg}^{-1} \text{ K}^{-1}$, and k_p is varied relative to k_a . where subscripts p , s , and a stand for particle, substrate, and air. Irradiance, $E = 3000 \text{ W m}^{-2}$).....62

- 3-15. The plot of time-dependent photothermal deflection signal showing the effects of aerosol's heat capacity for different ratio of aerosol's heat capacity to heat capacity of air with high absorbance aerosols; \square 0.1, \blacksquare 0.5, Δ 1, \bullet 5, \square 10 ($k_s = 59.8 \text{ W m}^{-1}\text{K}^{-1}$, $C_{ps} = 320 \text{ J kg}^{-1} \text{ K}^{-1}$, $\rho_s = 5330 \text{ kg m}^{-3}$, $k_p = 1.8 \text{ W m}^{-1} \text{ K}^{-1}$, $\rho_p = 1720 \text{ kg m}^{-3}$, $k_a = 0.0261 \text{ W m}^{-1} \text{ K}^{-1}$, $C_{pa} = 1010 \text{ J kg}^{-1} \text{ K}^{-1}$, and C_{pp} is varied relative to C_a . where subscripts p , s , and a stand for particle, substrate, and air. Irradiance, $E = 3000 \text{ W m}^{-2}$).....63
- 3-16. The plot of time-dependent photothermal deflection signal showing the effects of aerosol's thermal conductivity for different ratio of aerosol's thermal conductivity to thermal conductivity of air with high absorbance aerosols; \square 1, \bullet 10, Δ 100, \blacksquare 1000, --- 10000 ($k_s = 59.8 \text{ W m}^{-1}\text{K}^{-1}$, $C_{ps} = 320 \text{ J kg}^{-1} \text{ K}^{-1}$, $\rho_s = 5330 \text{ kg m}^{-3}$, $C_{pp} = 1740 \text{ J kg}^{-1} \text{ K}^{-1}$, $\rho_p = 1720 \text{ kg m}^{-3}$, $k_a = 0.0261 \text{ W m}^{-1} \text{ K}^{-1}$, $C_{pa} = 1010 \text{ J kg}^{-1} \text{ K}^{-1}$, and k_p is varied relative to k_a . where subscripts p , s , and a stand for particle, substrate, and air. Irradiance, $E = 3000 \text{ W m}^{-2}$).....64
- 3-17. Plot of time-dependent photothermal deflection signal showing how substrate's thermal properties influence photothermal signal for different substrate's heat capacity relative to heat capacity of air with low absorbing aerosol; \square 0.1, \circ 0.5, \blacktriangle 1, --- 5, \blacksquare 10 ($k_p = 1.8 \text{ W m}^{-1} \text{ K}^{-1}$, $C_{pp} = 1740 \text{ J kg}^{-1} \text{ K}^{-1}$, $\rho_p = 1720 \text{ kg m}^{-3}$, $k_s = 59.8 \text{ W m}^{-1} \text{ K}^{-1}$, $\rho_s = 5330 \text{ kg m}^{-3}$, $k_a = 0.0261 \text{ W m}^{-1} \text{ K}^{-1}$, $C_{pa} = 1010 \text{ J kg}^{-1} \text{ K}^{-1}$, and C_{ps} is varied relative to C_{pa} . where subscripts p , s , and a stand for particle, substrate, and air. Irradiance, $E = 3000 \text{ W m}^{-2}$).....66
- 3-18. Plot of time-dependent photothermal deflection signal showing how substrate's thermal properties influence photothermal signal for different ratio of substrate's thermal conductivity to thermal conductivity of air with high absorbing aerosol; \square 1, \bullet 10, Δ 100, \blacksquare 1000, --- 10000 ($k_p = 1.8 \text{ W m}^{-1} \text{ K}^{-1}$, $C_{pp} = 1740 \text{ J kg}^{-1} \text{ K}^{-1}$, $\rho_p = 1720 \text{ kg m}^{-3}$, $C_{ps} = 320 \text{ J kg}^{-1} \text{ K}^{-1}$, and $C_{pa} = 1010 \text{ J kg}^{-1} \text{ K}^{-1}$, $k_a = 0.0261 \text{ W m}^{-1} \text{ K}^{-1}$, $\rho_s = 5330 \text{ kg m}^{-3}$, k_s is varied relative to k_a where subscripts p , s , and a stand for particle, substrate, and air. Irradiance, $E = 3000 \text{ W m}^{-2}$).....67
- 3-19. Plot of time-dependent photothermal deflection signal showing how substrate's thermal properties influence photothermal signal for different substrate's thermal conductivity relative to thermal conductivity of air with low absorbing aerosol; \square 1, \bullet 10, Δ 100, \blacksquare 1000, --- 10000 ($k_p = 1.8 \text{ W m}^{-1} \text{ K}^{-1}$, $C_{pp} = 1740 \text{ J kg}^{-1} \text{ K}^{-1}$, $\rho_p = 1720 \text{ kg m}^{-3}$, $C_{ps} = 320 \text{ J kg}^{-1} \text{ K}^{-1}$, and $C_{pa} = 1010 \text{ J kg}^{-1} \text{ K}^{-1}$, $k_a = 0.0261 \text{ W m}^{-1} \text{ K}^{-1}$, $\rho_s = 5330 \text{ kg m}^{-3}$, k_s is varied relative to k_a where subscripts p , s , and a stand for particle, substrate, and air. Irradiance, $E = 3000 \text{ W m}^{-2}$).....68

3-20.	Three dimensional geometry of non-uniform aerosols deposited on flat substrate and the probe beam propagation.....	69
3-21.	Spatial temperature change profile showing the effects of surface texture on temperature gradient above aerosol for: I. uniform aerosols (all aerosols equal in size and shape), II. non-uniform aerosols. <i>Prolate</i> ($z = 1.5625 \mu\text{m}$, $a = b = 0.8 \mu\text{m}$ in Eq. 2), <i>spherical</i> ($z = a = b = 1 \mu\text{m}$ in Eq. 2), and <i>oblate</i> ($z = 0.4096 \mu\text{m}$, $a = b = 1.5625 \mu\text{m}$ in Eq. 2) with equal absorbance of 2676 m^{-1}	70
3-22.	Time-dependent photothermal signal for: I. uniform aerosols (all aerosols equal in size and shape), II. non-uniform aerosols. <i>Prolate</i> ($z = 1.5625 \mu\text{m}$, $a = b = 0.8 \mu\text{m}$ in Eq. 2), <i>spherical</i> ($z = a = b = 1 \mu\text{m}$ in Eq. 2), and <i>oblate</i> ($z = 0.4096 \mu\text{m}$, $a = b = 1.5625 \mu\text{m}$ in Eq. 2) with equal absorbance of 2676 m^{-1}	71
3-23.	Time-dependent photothermal deflection signals showing the effects of inter-particle contact on signal for, \square low absorbance aerosol model, \bullet high absorbance aerosol model.....	72
3-24.	Plot of theoretical photothermal signal with number of aerosols with constant irradiance source and gaussian irradiance source (assuming gaussian laser beam radius of $100 \mu\text{m}$) for ammonium nitrate aerosols on germanium substrate; $\text{---}\blacklozenge\text{---}$ gaussian irradiance, $\text{---}\circ\text{---}$ constant irradiance.....	73
3-25.	Three dimension geometry for three-2 μm aerosol with different probe beam propagation direction.....	74
3-26.	Effect of probe beam direction on photothermal signal for ammonium nitrate aerosols on germanium plate; \blacktriangle 180° to x -axis, \circ 45° to x -axis, \blacklozenge 90° to x -axis.....	75
3-27.	Time-dependent photothermal deflection signal with CW excitation showing the effects of aerosols heat capacity for different ratio of heat capacity to heat capacity of air. \square 0.1, $+$ 0.5, \blacksquare 1, Δ 5, \bullet 10. No difference in the profile for low and high absorbance aerosols except for their magnitude ($k_s = 59.8 \text{ W m}^{-1}\text{K}^{-1}$, $C_{ps} = 320 \text{ J kg}^{-1} \text{ K}^{-1}$, $\rho_s = 5330 \text{ kg m}^{-3}$, $k_p = 1.8 \text{ W m}^{-1} \text{ K}^{-1}$, $\rho_p = 1720 \text{ kg m}^{-3}$, $k_a = 0.0261 \text{ W m}^{-1} \text{ K}^{-1}$, $C_{pa} = 1010 \text{ J kg}^{-1} \text{ K}^{-1}$, and C_{pp} is varied relative to C_a . where subscripts p , s , and a stand for particle, substrate, and air. Irradiance, $E = 3000 \text{ W m}^{-2}$).....	77

- 3-28. Time-dependent photothermal deflection signal with CW excitation showing the effects of aerosols thermal conductivity for different ratio of aerosol's thermal conductivity to thermal conductivity of air. □ 1, + 10, ■ 100, Δ 1000, ● 10000. No difference in the profile for low and high absorbance aerosols except for their magnitude ($k_s = 59.8 \text{ W m}^{-1}\text{K}^{-1}$, $C_{ps} = 320 \text{ J kg}^{-1} \text{ K}^{-1}$, $\rho_s = 5330 \text{ kg m}^{-3}$, $C_{pp} = 1740 \text{ J kg}^{-1} \text{ K}^{-1}$, $\rho_p = 1720 \text{ kg m}^{-3}$, $k_a = 0.0261 \text{ W m}^{-1} \text{ K}^{-1}$, $C_{pa} = 1010 \text{ J kg}^{-1} \text{ K}^{-1}$, and k_p is varied relative to k_a . where subscripts p , s , and a stand for particle, substrate, and air. Irradiance, $E = 3000 \text{ W m}^{-2}$).....78
- 3-29. Time-dependent photothermal deflection signal with CW excitation showing the effects of substrate's heat capacity for different ratio of substrate's heat capacity to heat capacity of air. □ 0.1, + 0.5, ■ 1, Δ 5, ● 10. No difference in the profile for low and high absorbance aerosols except for their magnitude ($k_p = 1.8 \text{ W m}^{-1} \text{ K}^{-1}$, $C_{pp} = 1740 \text{ J kg}^{-1} \text{ K}^{-1}$, $\rho_p = 1720 \text{ kg m}^{-3}$, $k_s = 59.8 \text{ W m}^{-1} \text{ K}^{-1}$, $\rho_s = 5330 \text{ kg m}^{-3}$, $k_a = 0.0261 \text{ W m}^{-1} \text{ K}^{-1}$, $C_{pa} = 1010 \text{ J kg}^{-1} \text{ K}^{-1}$, and C_{ps} is varied relative to C_{pa} . where subscripts p , s , and a stand for particle, substrate, and air. Irradiance, $E = 3000 \text{ W m}^{-2}$).....79
- 3-30. Time-dependent photothermal deflection signal with CW excitation showing the effects of substrate thermal conductivity for different ratio of thermal conductivity to thermal conductivity of air. □ 1, + 10, ■ 100, Δ 1000, ● 10000. No difference in the profile for low and high absorbance aerosols except for their magnitude ($k_p = 1.8 \text{ W m}^{-1} \text{ K}^{-1}$, $C_{pp} = 1740 \text{ J kg}^{-1} \text{ K}^{-1}$, $\rho_p = 1720 \text{ kg m}^{-3}$, $C_{ps} = 320 \text{ J kg}^{-1} \text{ K}^{-1}$, and $C_{pa} = 1010 \text{ J kg}^{-1} \text{ K}^{-1}$, $k_a = 0.0261 \text{ W m}^{-1} \text{ K}^{-1}$, $\rho_s = 5330 \text{ kg m}^{-3}$, k_s is varied relative to k_a where subscripts p , s , and a stand for particle, substrate, and air. Irradiance, $E = 3000 \text{ W m}^{-2}$).....80
- 4-1. Schematic diagram of a single impaction stage.....86
- 4-2. Aerosol sampling apparatus: 1. Air source, 2. Valve, 3. Air filter, 4. BGI Collison Atomizer, 5. Pressure Gauge, 6. Drier, 7. 5L-Volume mixing chamber, 8. 4 m X 0.15 m Cylindrical slow-Flow tube, 9. 10 stage MOUDI Impactor, 10. Vacuum Pump, 11. Valve, 12. Air filter.....87
- 4-3. Laboratory setup of equipment for generation and collection of ammonium nitrate aerosols. A. Collison atomizer and drier, B. Micro-Orifice Uniform Deposit Impactor (MOUDI), C. MOUDI single stage and impaction plate.....90
- 4-4. Non-rotating impaction deposit collected on stage 6 of MOUDI, and pixel intensity profile of individual spot (emphasized).....92

4-5.	Image of rotating impaction deposit collected on stage 6 of MOUDI.....	93
4-6.	Experimental setup for Confocal Raman Microscopy Measurement.....	96
4-7.	Image of spatially diffused ammonium nitrate aerosols collected on #1 thickness microcover glass for Confocal Raman microscopy. Each particle diameter is about 1 μm	97
4-8.	Measured Raman shift of single ammonium nitrate aerosol (1 μm aerodynamic diameter) using Convocal Raman Microscopy. Ammonium nitrate particle has major shifts at 726 cm^{-1} , 1050 cm^{-1} , and 1440 cm^{-1}	98
5-1.	Photothermal mirage apparatus: The excitation beam is focused by a 100 mm focal length reflective off-axis parabolic mirror. The probe laser, propagating just above the sample's surface in a horizontal axis perpendicular to the pump beam axis, was focused by a 100 mm fused silica lens. The deflection signal is detected by a bi-cell position sensing detector. Excitation pulse energy is simultaneously measured with the deflection signal using RjP-735 pyroelectric energy monitor.....	106
5-2.	Pulse-to-pulse photothermal mirage signals from collected aerosols for individual spot from non-rotating impaction deposit.....	110
5-3.	Pulse-to-pulse photothermal deflection signals from collected aerosols for radial scanning from rotating impaction deposit.....	111
5-4.	Time dependent photothermal mirage signal from collected aerosols for — rotating impaction deposit measured at a space region with high aerosol's deposit, — individual spot from non-rotating impaction deposit.....	112
5-5.	Energy dependent photothermal mirage signal from collected aerosols for ♦ individual spot in non-rotating impaction, and * rotating impaction deposit.....	113
5-6.	MOUDI mass calibration curve with rotating impaction plate. ♦ Stage 7, Δ Stage 8, + Stage 6.....	115
5-7.	Mass – Collection time plot for non-rotating impaction deposits on: ♦ Stage 6, + Stage 5 of MOUDI.....	116
5-8.	Standard curve for average mass loading of individual spot from stage 6 of MOUDI at different time.....	117

5-9.	Signal-Collection time plot for photothermal deflection of aerosols collected on stage 6 of MOUDI with non-rotating impaction plate.....	118
5-10.	Standard plot of photothermal deflection signal with predicted mass loading for individual aerosol spot.....	119
5-11.	Images of aerosols on #1 micro plate collected for 10 seconds and 20 seconds.....	122
5-12.	Images of aerosols on #1 micro plate collected for 60 seconds and 120 seconds.....	123
5-13.	Counts-Loading time curve for impactor calibration. ◆ Adjusted counts, * measured count.....	126
5-14.	Relative standard deviation in count-time relationship.....	127
5-15.	Photothermal deflection with number concentration standard curve.....	129
6-1.	Apparatus for transmission thermal lens experiment. Detector 1 measures variation in He-Ne laser beam intensity. Detector 2 is set to measure the reference beam. The operational divider is used to process the signal as ratio of the real signal to the reference multiply by 10.....	141
6-2.	Experimental thermal lens signals for standard quartz cuvette containing a FeCp ₂ ethanol solution in a quartz cuvette.....	147
6-3.	Experimental thermal lens signals for 5 mm thickness CdS _x Se _{1-x} doped Corning glass filter.....	148
6-4.	Experimental thermal lens signals for 1 mm thickness metal-ion doped Schott NG 11 glass filter.....	149
6-5.	Finite element analysis thermal lens signal for: (a) ◆ 5 mm thickness Corning glass CS-3-79, ◆ 1 mm thickness Schott NG 11.....	150
6-6.	Finite element analysis thermal lens signal for ethanol in 5 mm pathlength cuvette.....	152
6-7.	The plot of Inverse focal length versus inverse beam waist. ▪ (1/f Infinite Cylinder), — (Linear Infinite Cylinder), ● (1/f Modeling), ----- (Linear Modeling).....	153

LIST OF ABBREVIATIONS

Abbreviations	Definition
PM	Particulate Matter
NAAQS	National Ambient Air Quality Standards
PDEs	Partial Differential Equations
CAD	Computer-Aided Design
CW	Continuous Wave
PSD	Position Sensing Detection
BS	Beam Splitter
EM	Energy Monitor
BA	Beam Attenuator
A/D	Analog-to-Digital
L	Lens
HeNe	Helium Neon
CFC-11	Trichloromonofluoromethane
OPM	Off-axis Barabolic Mirror
TEM	Transverse Electromagnetic Mode
FEA	Finite Element Analysis
U.D.E.Q	Utah Department of Environmental Quality
U.S.EPA	United States Environmental Protection Agency
EPA	Environmental Protection Agency
NA	Numerical Aperture

CCD	Charged Coupled Device
UV-VIS	Ultraviolet-Vissible Spectrometer
NIR	Near Infrared
Mid-IR	Mid-Infrared
CNC	Condensation Nuclei Counter
CCNC	Cloud Condensation Nuclei Counter
LBA-PC	Laser Beam analyzer for Personal Computer
RSA	Random Sequential Adsorption

CHAPTER 1

INTRODUCTION

Concentration measurement of atmospheric aerosols is of high interest in environmental science and setting regulatory standards. This dissertation presents development and demonstration of a sensitive photothermal spectrometry method, based on optical beam deflection, for the analysis of aerosols. The study was originally proposed for organophosphate pesticides in particulate form. However, it was thought that application to wider range of samples will be of more importance; so that the aerosol to be measured will determine the laser wavelength chosen for the excitation and probe beam. The remaining part of the detector (optical system and electronics) will be independent of the aerosol sample.

First a small size apparatus is constructed to evaluate its performance compared to conventional laboratory bench apparatus. The effects of scaling down the apparatus are largely unknown though the results are promising for idealized conditions. The prototype small apparatus is tested with gaseous and vapor phase samples for sensitivity. Then an infrared photothermal deflection apparatus in small configuration is developed for aerosols application. Many of the measurements in this dissertation are performed on laboratory generated ammonium nitrate aerosols, which are also major components of atmospheric aerosols especially in Cache Valley, Utah. The aerosols are produced with a homemade generation and sampling apparatus. This apparatus is coupled with commercial micro-orifice uniform deposit impactor (MOUDI) that collects separated aerosols based on aerodynamic size.

Photothermal measurements are carried out in terms of aerosol number concentration and aerosol mass concentration. The measurement laser used is a single line CO₂ laser. This has limitations in determining chemical compositions of aerosols. Another method will be required to determine aerosol components when the photothermal method does not use broad band excitation source. In this research, chemical composition of aerosols is examined with Raman microscopy. For all the reported experiments, apparatus optimization and heat flow modeling is performed with finite element analysis. The finite element differential equation software is used to evaluate choice of materials and apparatus geometry. The modeling also predicts more accurate heat flow as sample and apparatus sizes are scaled down.

AEROSOLS

Basic Information. An aerosol may be defined as suspension of solid or liquid particles in air. By this definition, aerosols should include both the particles and all vapor or gas phase components of air. A full definition of aerosol would include the description of the chemical composition, morphology, and size of each particle, as well as the relative abundance of each particle type as a function of particle size.¹⁻³ However, the term aerosol is sometimes used to refer to the suspended particles only. Atmospheric particles possess various physical, chemical, morphological, and thermodynamic properties. The diameter of a spherical particle, which is the most often encountered physical property, may be determined by various means. Because atmospheric particles are often not spherical therefore their diameters are described by an equivalent diameter.

Aerodynamic diameter, mostly used to describe particulate matters, is the diameter of a spherical particle with material density of 1 gcm^{-3} and equivalent gravitational settling velocity.^{4, 5}

Particulate matter (PM), also known as particle pollution, is a complex mixture of extremely small dust and soot particles. PM is divided into two categories, “PM₁₀” and “PM_{2.5}.” PM₁₀ refers to particles with 10 μm diameter or less. That would be about one-seventh the width of a strand of human hair. PM_{2.5} is even smaller - measuring 2.5 μm or less. Particle pollution is made up of a number of components, including acids (such as nitrates and sulfates), organic chemicals, metals, and soil or dust particles. Origin of some particles known as primary particles are directly from sources, such as construction sites, unpaved roads, fields, smokestacks or fires. Others are produced from complicated atmospheric chemical reactions of chemicals such as SO₂ and nitrogen oxides (NO_x) that are emitted from power plants, industries, automobiles, agriculture facilities. These particles, referred to as secondary particles, make up most of the fine particle pollution in the United State. These particles are so small that they can penetrate human lung tissue, causing or exacerbating respiratory diseases and cardiovascular problems. Numerous studies have linked particle pollution to many health problems including: increased respiratory symptoms; such as irritation of the airways, coughing, or difficulty breathing, decreased lung function; aggravated asthma; development of chronic bronchitis; irregular heartbeat; nonfatal heart attacks; and premature death in people with heart or lung disease.^{6, 7}

Regulatory Standards. U.S. EPA revised the National Ambient Air Quality Standards (NAAQS) for PM pollution on September 21, 2006.^{8,9} The final standards address the two categories of particle pollution: fine particles ($PM_{2.5}$), and coarse particles (PM_{10}). U.S. EPA strengthened the 24-hour $PM_{2.5}$ standard from the 1997 level of $65 \mu\text{g m}^{-3}$ to $35 \mu\text{g m}^{-3}$, and retained the current annual $PM_{2.5}$ standard at $15 \mu\text{g m}^{-3}$. U.S. EPA also retained the existing national 24-hour PM_{10} standard of $150 \mu\text{g m}^{-3}$ but revoked the annual PM_{10} standard. These new standards became effective on December 17, 2006.

Cache Valley Particle Pollution. Cache Valley, located in northern Utah, USA, is about 4535 ft (1382 m) elevation above sea level. In cache valley, where Utah State University is situated; particle pollution has been of great concern in recent years. During winter temperature inversions, Cache Valley has historically exceeded national standard levels. Reports suggest that particulate matter compositions in this region are mainly secondary type, that is, particles that are formed from chemical reactions in the air.¹⁰ One of the products formed is ammonium nitrate which is believed may be due to primary emissions from on-road automobile and agriculture facilities. Following promulgation of the revised standard by EPA, Cache Valley is one of the three areas designated as nonattainment for $PM_{2.5}$ by the State of Utah.¹¹

PHOTOTHERMAL SPECTROSCOPY

Size distributions by particle number used to calculate surface area and volume distributions often are determined by physical means, such as electrical mobility,

aerodynamic behavior, or light scattering. Chemical composition usually is determined by analysis of collected sample. The need for low cost sensitive and accurate monitoring of local air quality is essential to insure people's health. One potential method for obtaining trace chemical analysis of aerosols is laser excited photothermal spectroscopy.

Photothermal spectroscopy has been used to measure extremely small absorbance in homogeneous gas and liquid samples, in the bulk of solid materials, and on surfaces. Previously reported studies claims that photothermal spectrometry can have a detection limit of 10^{-10} absorbance unit for gas-phase species with laser excited photothermal spectroscopy.¹²⁻¹⁵ Photothermal spectrometry is closely related to photoacoustic except for the method of detecting the sample heating. In photoacoustic the sample is heated by a source of light which is either lamp or laser. The absorbed energy heats up the sample and the subsequent temperature change in the surrounding gas causes the gas to expand and contract according to the modulation frequency of the light. The associated pressure variation intensity is then measured with a microphone.¹⁶⁻²⁵ In contrary, photothermal sample heating is detected by measuring the change in refractive index of the surrounding medium due to the temperature gradient in the medium. Photothermal spectroscopy is theoretically and measurably 100 times, or more, sensitive than the photoacoustic signal for equivalent laser-based detectors. Most common photothermal techniques are photothermal deflection spectrometry and thermal lensing spectrometry.

Operating principles for photothermal spectrometry are known for pulsed and continuous laser excitation under variety of sample and coupling matrix conditions. In photothermal deflection the gradient of the refractive index profile is probed by a probe

laser beam, and the photothermal signal is defined in terms of deflection angle. In thermal lensing, which was first discovered by Gordon *et al.*,^{26,27} the curvature of the refractive index profile is probed and the signal is defined in terms of focal length. However, the common difficult task associated with all methods of photothermal spectroscopy is constructing a sensitive, accurate and predicible apparatus.

Pulse-laser photothermal deflection spectroscopy is an ultra-sensitive technique used for measurement of small optical absorbance in solid, liquid, and gaseous samples.^{28,29} Photothermal deflection spectroscopy is performed by using a probe laser to monitor the temperature dependent refractive index gradient produced by the excitation source. Most schemes for obtaining electronic signal from the probe laser are based on monitoring a change in position of the probe laser beam spot at some distance past the sample cell. The two main methods for performing these position measurements are to use a linear aperture which bisects the beam image, such as razor blade, followed by a detector, or to use a commercial bi-cell or lateral position-sensing detector with associated electronic processing modules.

Two types of apparatus setup are common in doing photothermal deflection spectroscopy: collinear and transverse setup.^{25,30} Collinear geometry is that for the probe laser beam propagating parallel to the excitation laser. In transverse geometry or crossed-beam probe geometry, the probe laser beam propagation axis is perpendicular to that of the excitation laser. However, the probe beam in crossed-probe geometry can either propagate through the center of the sample or through the fluid above the surface of the sample such as in photothermal deflection in mirage geometry.

Photothermal deflection in mirage configuration (mirage effect) is the most applicable photothermal technique when samples that are not transparent in the probe beam wavelength are to be analyzed. It was first demonstrated by Boccara *et al.*³¹ that temperature gradient field close to a sample surface can be monitored with photothermal deflection. This method has had many theoretical, experimental developments and was found to be sensitive and very easy to set up. The “mirage effect” is a special form of photothermal deflection spectroscopy that probes the heat diffusion within a sample in an indirect way. A sample is illuminated with a modulated electromagnetic radiation of laser source and the thermal waves produced propagate through the sample into the surrounding fluid. This process produces a temperature gradient that causes a change in refractive index of the surrounding fluid, which subsequently alters the propagation of a probe beam that passes through the fluid. Thermo-optical properties, as well as the concentration of the sample can be obtained by measuring the phase change in the deflected probe beam.

A good illustration of photothermal deflection in mirage configuration is the shimmering surface or optical mirage effect shown in Figure 1-1. A hot highway sometimes looks like a reflective surface which apparently not due to reflection. Following absorption of solar radiation by the asphalt or concrete, a temperature gradient is produced in the air near the surface due to thermal energy transfer to the air above the surface.

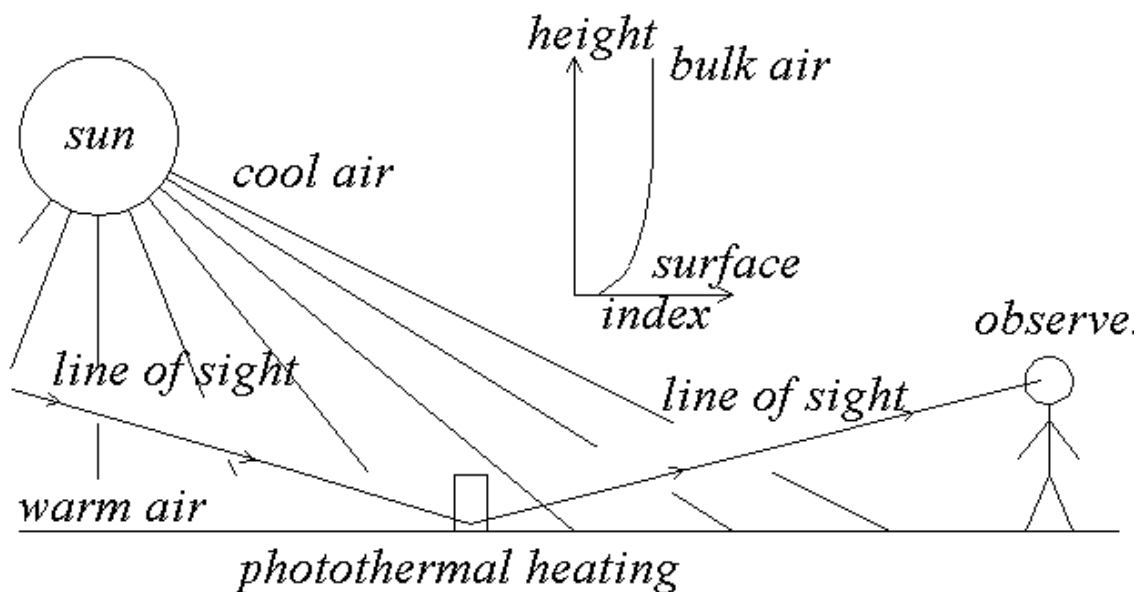


Figure 1-1. An early photothermal deflection apparatus for measuring absorbance of the earth's surface. Reprinted with permission from S. E. Bialkowski (1996).³⁰ Copyright 1996, John Wiley and Sons.

This causes a decrease in the refractive index of the air near the surface. Since light travels faster in low refractive index media, light incident at an acute tangent angle is refracted upward. An observer looking at the surface at an acute tangent angle does not see the surface but rather sees the deflected solar radiation at the surface.

Application of photothermal deflection to studying bulk of various materials is well known but no previous work has been reported on aerosols. This dissertation is focused on the development of photothermal spectroscopy apparatus based on photothermal deflection spectrometry in mirage configuration for aerosols analysis.

FINITE ELEMENT ANALYSIS MODELING OF PHOTOTHERMAL PHENOMENON

Finite element analysis (FEA) is a method used to obtain numeric solutions of complex differential equations. While FEA has been used in engineering applications for some time, advances in software and computer technology have made this method easier to use while also improving the accuracy (determined by the number of sub-domains or elements the boundary value problem is broken up into). Commercial software is available to streamline the process, allowing the user to define the geometry and boundary conditions in a Computer-Aided Design (CAD) environment.

COMSOL Multiphysics v 3.3 (Comsol Inc.) is a powerful interactive environment for modeling and solving all kinds of scientific and engineering problems based on partial differential equations (PDEs). With this product it is possible to build models by defining the relevant physical quantities - such as material properties, loads, constraints, sources, and fluxes - rather than by defining the underlying equations. COMSOL Multiphysics then internally compiles a set of PDEs representing the entire model. As noted, the underlying mathematical structure in COMSOL Multiphysics is a system of partial differential equations. Using the application modes in COMSOL Multiphysics, various types of analysis including: Stationary and time-dependent analysis, Linear and nonlinear analysis, and Eigen frequency and modal analysis can be performed.³²

To solve the PDEs, COMSOL Multiphysics uses the proven FEA method. The software runs the finite element analysis together with adaptive meshing and error control using a variety of numerical solvers. Models of all types can be built in the COMSOL

Multiphysics user interface. For additional flexibility, COMSOL also provides its own scripting language, COMSOL Script, where the model can be accessed as a Model M-file or a data structure. In this dissertation, models of heat transfer process in various samples are performed with Comsol Multiphysics v 3.3.

The analysis steps in finite element modeling are:

1. Defining Multiphysics - Definition of the desired physics mode (heat transfer by conduction, convection, and/or radiation) and types of solution (steady state or transient).
2. Geometry Modeling - Definition of sample geometry and materials, boundary conditions, heat sources and sinks.
3. Meshing- Breaking the geometry into sub-domains or elements meshing.
4. Solve the model - Solving the model by choosing appropriate solver parameter.
5. Post processing - The solution is plotted using a variety of visualization techniques. The data from these plots can also be exported for further analysis in spreadsheet software such as Excel.

ORGANIZATION OF THE REMAINING CHAPTERS

The remaining chapters in this dissertation contain detailed researches that answer scientific questions on potential of photothermal deflection method for in situ analysis of atmospheric aerosols. In Chapter 2, small size photothermal apparatus that is expected to have about the same performance with conventional laboratory scale apparatus is evaluated. The archetypical small apparatus is compared with the conventional type in

terms of sensitivity performance. Chapter 3 contains numerical modeling of heat transport and photothermal signal from aerosols deposited on flat substrate based on the famous finite element analysis method for solving complex differential equations. The models are used to predict photothermal signals as a function of aerosol and substrate properties such as size, shape, absorption coefficient, heat capacity, thermal conductivity, and arrangement of particles. In Chapter 4, a homemade aerosol generation and sampling equipment is presented. The apparatus is used to produce standard aerosols with known size and composition for the photothermal measurement presented in Chapter 5. The photothermal experiment reported in Chapter 5 details the potential of mid-infrared photothermal deflection spectrometry for analysis of condensed-phase aerosols collected on germanium disc. Standard aerosols generated by using the apparatus developed in Chapter 4 are used to calibrate the photothermal apparatus. Aerosol quantitation is carried out for number concentration and mass concentration. Chapter 6 reports the outcome of thermal lensing spectrometry of colored glass filters that were expected to be used as calibration standards for photothermal measurements. It turns out that the glasses produce positive refractive index change contrary to the expected negative index of refraction change. Chapter 7 is a brief summary of the results in Chapters 2-6. The term aerosol and particle are used interchangeably in the whole of this document. All the figures data are available in Appendix A.

REFERENCES

- 1 S. K. Friedlander, *Journal of Aerosol Science* **1**, (4), 295-305 (1970).
- 2 S. K. Friedlander, *Journal of Aerosol Science* **2**, (3), 331-340 (1971).
- 3 S. K. Friedlander, *Environmental Science and Technology* **7**, (3), 235-240 (1973).
- 4 U.S. EPA, *Air Quality Criteria for Particulate Matter*, 2004; Vol. I.
- 5 U.S. EPA, *Air Quality Criteria for Particulate Matter*, 2004; Vol. II.
- 6 T. Cheng, J. Hwang, P. Wang, C. Tsai, C. Chen, S. Lin, and C. Chan, *Environmental Health Perspectives* **111**, (2), 147-150 (2003).
- 7 D. Upadhyay, V. Panduri, A. Ghio, and D. W. Kamp, *American Journal of Respiratory Cell and Molecular Biology* **29**, 180-187 (2003).
- 8 U.S. EPA, *Revision to Ambient Air Monitoring Regulations: Final rule, Part III*. 2006; Vol. 71.
- 9 U.S. EPA, *National ambient Air quality Standards for Particulate Matter: Final Rule, Part II*. 2006; Vol. 71.
- 10 E. Malek, T. Davis, R. S. Martins, and P. J. Silva, *Atmospheric Research* **79**, 108-122 (2006).
- 11 U.D.E.Q, *Utah Area Designation Recommendation for the 2006 PM_{2.5} NAAQS*. 2008.
- 12 N. J. Dovichi, and J. M. Harris, *Analytical Chemistry* **51**, 728-731 (1979).
- 13 N. J. Dovichi, and J. M. Harris, *Analytical Chemistry* **53**, 106-109 (1981).
- 14 N. J. Dovichi, and S. E. Bialkowski, *Critical Reviews in Analytical Chemistry* **17**, (4), 357-423 (1987).

- 15 N. J. Dovichi, *Review of Scientific Instrument*, **61**, (12), 3653-3668 (1990).
- 16 J. V. Beitz, M. M. Doxtader, V. A. Maroni, S. Okajima, and D. T. Reed, *Review of Scientific Instrument*, **61**, 1395-1403 (1990).
- 17 E. L. Kerr, and J. G. Atwood, *Applied Optics* **7**, 915-922 (1968).
- 18 L. B. Kreuzer, *Journal of Applied Physics* **42**, 2934-2943 (1971).
- 19 L. B. Kreuzer, N. D. Kenyon, and C. K. N. Patel, *Science* **177**, 347-349 (1972).
- 20 C. K. Patel, R. J. Kerl, and E. G. Burkhardt, *Physical Review Letter* **38**, 1204-1207 (1977).
- 21 C. K. Patel, and A. C. Tam, *Reviews of Modern Physics* **53**, 517-550 (1981).
- 22 A. Rosencwaig, *Opto-Acoustic Spectroscopy and Detection*. Academic Press, New York, 1977.
- 23 A. Rosencwaig, *Photoacoustics and Photoacoustic Spectroscopy*. John Wiley and Sons, New York, 1980.
- 24 A. C. Tam, in *Ultrasensitive Laser Spectroscopy*. Academic Press, New York, 1983.
- 25 A. C. Tam, *Reviews of Modern Physics* **58**, 381-431 (1986).
- 26 J. P. Gordon, R. C. C. Leite, R. S. More, S. P. S. Porto, and J. R. Whinnery, *Bulletin of American Physical Society*, **9**, 501 (1964).
- 27 J. P. Gordon, R. C. C. Leite, R. S. More, S. P. S. Porto, and J. R. Whinnery, *Applied Physics* **36**, 3-8 (1965).
- 28 A. J. Twarowski, and D. S. Kliger, *Chemical Physics* **20**, (2), 253-258 (1977).
- 29 A. J. Twarowski, and D. S. Kliger, *Chemical Physics* **20**, 259-264 (1977).

- 30 S. E. Bialkowski, *Photothermal Spectroscopy Methods for Chemical Analysis*.
John Wiley and Sons, New York, 1996.
- 31 A. C. Boccara, D. Fournier, and J. Badoz, *Applied Physics Letters* **36**, 130-132
(1980).
- 32 *Comsol Inc. Comsol Multiphysics 3.3 User's Guide*.

CHAPTER 2

CONSTRUCTION AND EVALUATION OF PROTOTYPE PHOTOTHERMAL APPARATUS BASED ON PHOTOTHERMAL DEFLECTION IN A SMALL CONFIGURATION

ABSTRACT

In this chapter, a prototype small photothermal deflection apparatus was constructed on a laboratory bench. Not including excitation laser, data collection computer, and gas pumps, the apparatus fits on a bench space with a footprint of about 10 cm x 10 cm. This is a prototype apparatus that will be miniaturized in future assemblies. The apparatus was tested relative to the conventional laboratory-scale photothermal apparatus. Digital filtering procedures developed in this laboratory were used to collect and analyze the data. The main result is that the small apparatus performs about the same as the larger laboratory-sized one in terms of sensitivity. The apparatus also exhibits a linear response for linear absorbers indicating a high dynamic range. Future improvements will include miniaturization and rugged construction. This will allow for portable use. Data processing will be adapted to modern operating systems. An electronics module containing the timing and data collection electronics will also be prototyped.

INTRODUCTION

Increasing awareness of the threats posed by atmospheric pollutants calls for sensitive and easy-to-use detection methods for hazardous atmospheric species. When

very small absorptions are encountered, photothermal spectroscopy is often the viable alternative. Pulse laser photothermal deflection spectroscopy is a sensitive technique for measuring small optical absorbance in solid, liquid, and gaseous samples.¹⁻¹⁰

Photothermal deflection spectroscopy is performed by using a probe laser to monitor the temperature dependent refractive index gradient produced when the optical energy absorbed by the sample is converted to heat via non-radiative relaxation mechanism.

Most schemes for obtaining electronic signal from the probe laser are based on monitoring a change in position of the probe laser beam spot at some distance past the sample cell. The two main methods for performing these position measurements are to use a linear aperture which bisects the beam image, such as razor blade, followed by a detector, or to use a commercial bi-cell lateral position-sensing detector with associated electronic processing modules.

In photothermal deflection, deflection angle is proportional to optical absorption, sample pathlength, analyte concentration, and the excitation source intensity. A measure of deflection angle is a function of analyte absorbance and concentration.¹ Since the probe laser beam which is normally focused at the position where the refractive index perturbation occurs is also diverging, the deflection angle cannot be enhanced by increasing the distance between the probe-region and the detector. In other words down-scaling the apparatus should produce equal, if not higher, signal as the conventional big apparatus. The deflection angle measured is also proportional to the thermo-optical properties of the analyte and the buffer-gas.

Advantages of using pulsed infrared lasers have been previously discussed in the literature.^{8, 11-13} Tunability of pulsed gas infrared lasers allows for spectra discrimination among most polyatomic molecules. Most of these species have vibrational absorption spectra with finite absorbance within the tuning range. At moderate gas pressure, probability of energy relaxation of excited species via quenching is higher than fluorescence due to long fluorescence lifetime and efficient quenching mechanism. Considering pulse and continuous wave excitation, pulsed photothermal signal rise times are faster than that of the related continuous wave (CW) laser excitation. Pulse-laser excitation prevents the analytical signal from being degraded by gas samples dynamics particularly in flowing samples. Although pulsed lasers have overall advantages in photothermal spectroscopy yet there are still difficulties associated with their use in photothermal spectroscopy. Most pulsed lasers have poor longitudinal and transverse (TEM) mode stability and their pointing noise characteristics are generally poorer than continuous wave lasers. Another source of error due to use of pulsed lasers is owing to pulse-to-pulse energy variance.

The hallmark of an analytical instrument is high sensitivity coupled with availability, simple operating procedure and reduced size. From the viewpoint of photothermal apparatuses, the main development issue for minimizing the apparatus size is to develop an ultra-short focus laser beam. Therefore, reductions in the photothermal apparatus have not been achieved over the last few years. Usually, the laser beams are focused with refractive lenses in convex and concave shapes that are obtained by polishing glass lenses. Aiming at achieving the required performance, the apparatus is

composed of multiple lenses with long focal length in order to control the beam spot position and aberration values. Reducing the focal distance significantly causes increased aberrations and compatibility has been very hard to achieve.

A reflective optical system that uses no refractive lens components at all is considered to be an ideal solution for obtaining a dramatic reduction in the focal distance and the correction of aberrations that may be caused by the reduction.^{14, 15} Reflective lenses use mirrors and are popularly used in the optics of telescopes including astronomical ones.^{14, 15} The mirror lens features an absence of color aberration because it is free from the waveform dependency of refractivity that becomes basically important with refractive glass lenses. The advantages of metal reflectors have led to widespread use of aspheric surfaces (off-axis parabolas). Off-axis parabolic mirror, if properly made, will theoretically give diffraction-limited performance.

This chapter of this dissertation is focused on the construction and evaluation of photothermal deflection apparatus in a small configuration. Off-axis parabolic mirror is used as the focusing optics in order to achieve the required short focal length with less variance in laser beam imaging. The need to understand the effect of downsizing the apparatus on the photothermal signal produced by the probed volume is the major content of this chapter. Photothermal deflection spectrometry of gaseous analyte is performed with large and reduced size apparatuses and the results are compared. The two apparatuses are compared with each other by obtaining the time dependent and energy dependent signal from both setups. The effects of scaling down the apparatus on photothermal signal are also investigated with numerical modeling based on finite

element analysis method. Finite element differential solution analysis was performed using COMSOL Multiphysics v 3.3 commercial software. This more accurately predict heat flow dynamics as sample cell and apparatus geometries are scaled down. The solution to the temperature profile within the sample is used to calculate the theoretical photothermal deflection signals.

THEORY

The operating principle of photothermal deflection is well known. Theories for most photothermal methods are based on the solution to the heat transfer processes that follows when the sample is heated.^{1-13, 16-27} For a TEM₀₀ pulse excitation beam with an integrated irradiance $H(r, t)$ (Jm⁻²) defined as

$$H(r, t) = \frac{2Q}{\pi w^2} e^{-2r^2/w^2} \quad (2-1)$$

where Q (J) is the laser pulse energy, w (m) is the pump laser waist radius, and r is the radial distance from the center of the pump laser beam. For the probe laser beam propagating the same axis with the excitation laser beam, with semi-infinite cylinder approximation, the temperature change that occurs upon optical absorption of the pump laser beam is

$$\delta T(r, t) = \frac{2\alpha Q Y_H}{\pi w^2 \rho C_p (1 + 2t/t_c)} e^{\left[\frac{-2r^2}{w^2 (1 + 2t/t_c)} \right]} \quad (2-2)$$

where α (m^{-1}) is the optical absorptivity, t (s) is time, t_c (s) = $w^2/4D_T$ is the characteristic thermal diffusion time, D_T ($\text{m}^2 \text{s}^{-1}$) is the thermal diffusion coefficient, ρ (kg m^{-3}) is the density, Y_H is quantum yield assumed to be 1, C_p ($\text{J kg}^{-1} \text{K}^{-1}$) is the heat capacity.

Assuming that the absorbed energy is transferred to the solvent shortly after pulsed irradiation, and that the photothermal signal is detected prior to thermal diffusion, the temperature change is related to the energy density and the heat capacity of the sample through Eq. 2-2. The photothermal spectroscopy signal strength is related to the temperature changes that occur due to optical absorption. The main optical element utilized in photothermal deflection spectroscopy is the prism. The effects that this element has on the propagation of the probe laser beam are given by the deflection angle produced by the prism. This element is obtained from the relationship:

$$\theta(r, t) = \left[\frac{dn}{dT} \right] \int_{path} \nabla_{\perp} \delta T(r, t) dS \quad (2-3)$$

where $\theta(r, t)$ is the probe beam deflection angle, n is the refractive index of the perturbed media, and S is the optical path through the sample. The differentials are found for the coordinates perpendicular to the pump beam propagation axis. With collinear excitation-probe laser geometry, this corresponds to the radial dimension, r . Combining Eq. 2-2 and 2-3 results in,

$$\theta(r, t) = - \left[\frac{dn}{dT} \right] \left[\frac{8r\alpha I Q}{\pi w^2 \rho C_p} \right] e^{-2r^2/w^2(1+2t/t_c)} \quad (2-4)$$

Eq. 2-4 shows that the deflection angle is a function of the radial offset, r , of the probe laser beam from the origin of the pump laser beam, and increases with the sample's pathlength, l , and inverse of the pump laser beam waist radius.

The maximum deflection angle occurs just after excited state relation at a radial offset of $r_{max} = w/2$, hence the maximum deflection angle is given as

$$\theta_{max} = -\frac{1}{n} \left[\frac{dn}{dT} \right] \left[\frac{8r\alpha l Q}{\pi w^4 \rho C_p} \right] \quad (2-5)$$

EXPERIMENTAL

Large Size Apparatus. Collinear pump-probe beam geometry, the most common case known for photothermal deflection apparatus with high sensitivity, is used in this experiment. For the conventional large-sized photothermal deflection spectrometry, the apparatus was constructed with standard Newport (City, CA) optical mounts on a 4' x 8' Modern Optics optical bench. The footprint of this apparatus was about 1 square meter, not including the gas handling equipment and the excitation laser. As illustrated in Figure 2-1, the apparatus consists of four major components: the pump laser and associated optics, the probe laser optics and detectors, signal collection and processing electronics, and the sample handling apparatus.

The pump laser was a Tachisto, pulsed, line-tunable CO₂ laser (9-11 μm wavelength). The output of this laser was a TEM₀₀ mode-pulse of 120-ns duration.

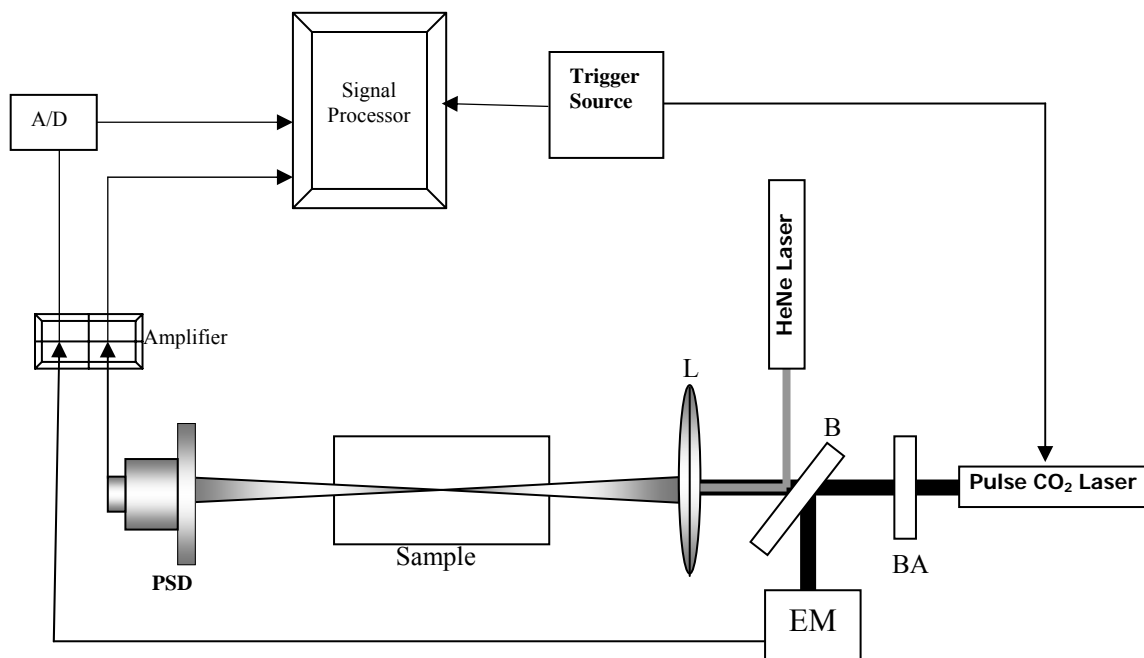


Figure 2-1. Schematic diagram of conventional large size photothermal deflection apparatus: Apparatus foot print is about 1 square meter not including the CO₂ laser. Distance from the centre of the sample cell to the PSD is about 254 mm. L-Lens, EM-Energy monitor, PSD-Position sensor detector, BS-Beam splitter, BA-Beam attenuator, A/D-Analog-to-Digital Converter.

Using low N₂ partial pressures in the CO₂ laser gas mixture minimized the relative energy in the “tail” portion of the pulse. The pulse laser energy was attenuated by placing a “Venetian blind” style infrared attenuator in the beam path prior to the focusing optics. CO₂ laser wavelengths were determined with an Optical Engineering CO₂ spectrum analyzer, Model 16-A.

The probe laser was a polarized 4-mW continuous-wave HeNe laser (632.8 nm wavelength), Uniphase Model 1205-1. The pump beam and the probe beam were mixed by using a germanium beam splitter. The combined beams were then focused with a 127 mm focal length BaF₂ lens before the sample. The sample position is adjusted so that the combined beam spot is right at the center of the sample cell. The beam waist of the focused CO₂ laser at the spot position was measured with a razor blade edge on a micrometer driven translation stage. The electric field beam waist calculated from the razor blade excursion resulting in 10% to 90% of the maximum pulse energy was 150 μm. Photothermal deflection was monitored by using a United Detector Technology Model 301-DIV single axis position-sensing detector. Signals from the detector were amplified and electronically filtered with a Tektronix model AM-502 differential amplifier.

The integrated pulsed laser energies were measured with a Laser Precision Model RjP-735 pyroelectric energy monitor and digitized with a 12-bit analog to digital converter (A/D). The integrated pulse energy is directly proportional to the intensity since the laser pulse duration and the focus spot size of the pump beam does not change from pulse to pulse. Data collection and processing were performed on a PC with matched filter smoothing software that was developed in this laboratory.²⁸⁻³⁰ The distance from the pump beam spot position and the detector is 254 mm. The large size sample cell radius is 15 mm with pathlength of 100 mm.

Small Size Apparatus. The schematic diagram and the image of the small size apparatus is shown in Figure 2-2 and Figure 2-3. The foot print of the small apparatus

prototype is about 0.01 square meters not including the excitation laser, the gas handling equipment, and signal processing electronic device. The excitation source is the same as the one used for the large apparatus.

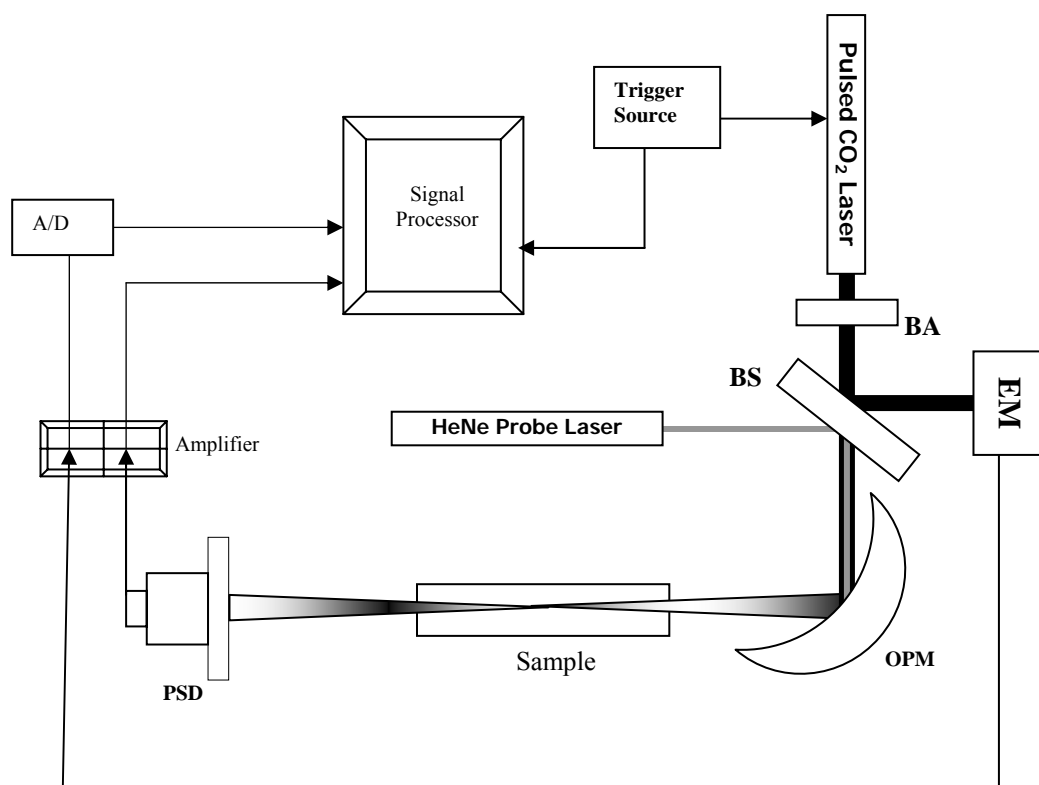


Figure 2-2. Schematic diagram of small size photothermal deflection apparatus: OPM-Off axis parabolic mirror, EM-Energy monitor, PSD-Position sensing detector, BS-Beam splitter, BA-Beam attenuator, A/D-Analog-to-Digital converter. Distance from the center of the sample cell to the PSD is about 30 mm.

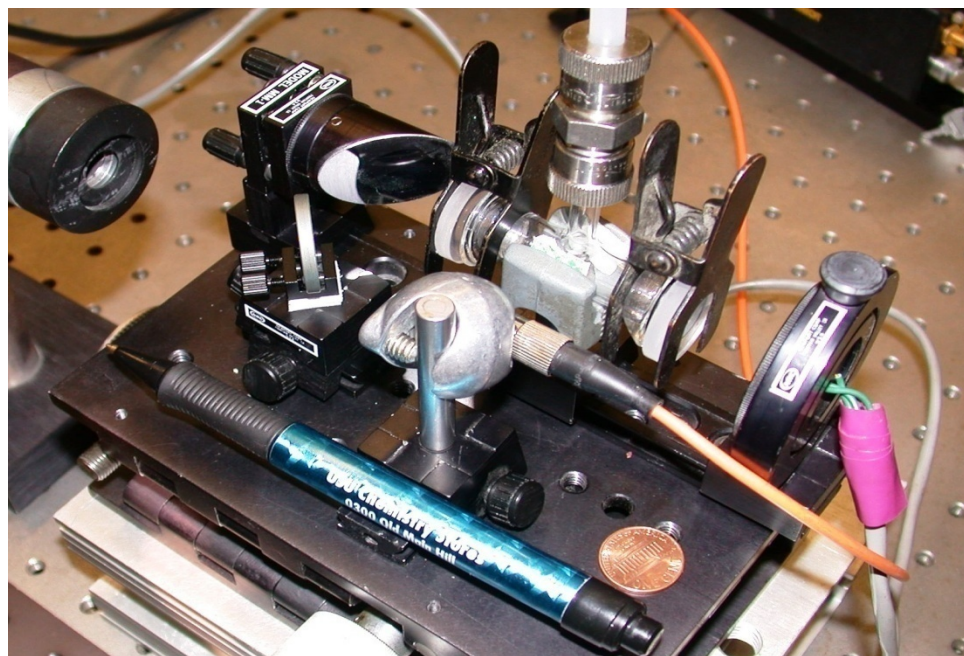


Figure 2-3. Image of the prototype small-size photothermal deflection apparatus with footprint of about 0.01 m^2 .

The detector and signal processing electronic devices are also the same. The probe beam is a Model 57ICS006/PS/HS Melles Griot fiber optics diode laser operating at 630 nm wavelength. Both pump and probe laser beams are first mixed with a 25 mm diameter germanium disc beam splitter, then focused into the center of the sample cell by a 50 mm focal length off-axis parabolic focusing mirror. The two beams are focused at the center of the sample cell and propagate through the sample cell in the same direction. The measured pump beam waist was measured to be $60 \text{ }\mu\text{m}$. The distance from the pump beam spot position, that is, the center of the sample cell, to the detector is 30 mm. The small sized sample cell radius is 4.5 mm and the pathlength is 37 mm.

Samples. The samples used are chosen to represent the gaseous and vapor phase atmospheric pollutants. The gaseous sample is 10 ppm trichlorofluoromethane (CFC-11) Matheson standard premixed gas balanced in nitrogen. The vapor phase sample is 200 % proof ethanol vapors. Lower concentration of the analyte is obtained by using ultrahigh vacuum dynamic gas mixer (see Appendix B). Linear dilution was done carefully to obtain lower partial pressure of both analytes in high grade nitrogen. The R25 line of the $9.30\ \mu\text{m}$ and $9.54\ \mu\text{m}$ CO_2 transitions are used for CFC-11 and ethanol vapor, respectively.

Procedures for Finite Element Analysis Modeling. The procedure for finite element analysis method to investigate photothermal phenomenon has been previously reported.³¹ In this case, the small and large apparatus are modeled in terms of sample cell geometry and pump laser-beam spot radius to represent the actual geometries for the experimental setup. Large apparatus modeled sample cell is 33 mm by 4.5 mm cylinder and the pump beam width is $120\ \mu\text{m}$. The small apparatus modeling is performed by scaling down the large apparatus sample cell geometry by a factor of 3, and the pump laser-beam spot radius by a factor of 2. The value of the pump laser power is 3 mW for all models. However the sample cell thickness is made constant and the heat source is only applied to the content of the cylinder. Two dimensional axial symmetry of the cylindrical sample cells is modeled so that the pump laser beam propagates along the symmetry axis, z-axis. The real excitation laser beam width changes with axial distance, z , hence w from Eq. 1 is given as

$$w^2 = w_o^2 \left[1 + (z/z_R)^2 \right] \quad (2-6)$$

where w_o is the beam spot radius, Z_R is the Raighley range of the focused laser beam defined as $\pi w_o^2/\lambda$. λ is the wavelength of the excitation laser.

The transient analysis of heat diffusion within the sample cell was obtained by having the FEA software solve the heat equation with the boundaries set at zero temperature (assuming no heat transfer through the sample cell wall) and heat input along the z -axis defined by Eq. 2-1. This way, the temperature solution represents δT . The relative photothermal lens signal strength is calculated from Eq. 2-3. The dn/dT is taken as being $-9.0 \times 10^{-7} \text{ (K}^{-1}\text{)}$ for nitrogen gas and $\alpha = 5.19 \text{ m}^{-1}$ for the analyte. The path integral of the first radial derivative was found by using integration coupling variable in Comsol Multiphysics to calculate the path integral of the first derivative of the temperature change with respect to r .

RESULTS AND DISCUSSIONS

Photothermal deflection spectrometry in a small configuration apparatus is presented for the first time. With collinear pump-probe beam geometry, as discussed in the theory, the magnitude of deflection angle is a function of the radial distance from the origin of the pump laser beam spot. This relationship requires that the spatial overlap between the pump and probe laser beams be known or at least reproducible. Misalignment of the overlap between the excitation and probe laser beam will not only

result in changes in the maximum detector signal proportional to the deflection angle but will also result in a change in the temporal characteristics of the signal.

Obtaining maximum sensitivity also requires that the pump and probe beams are focused into the sample cell. The reduced size photothermal apparatus uses aspheric (off-axis parabola) focusing mirror, which removes the longitudinal aberration normally encountered when wavelength dependent refracted material such as lens is used. Since reflective optics are not wavelength dependent, pump and probe laser beams spatial overlap enhancement and reproducibility are achieved by focusing both beams with the same parabolic mirror. Using short focal length mirror also takes the advantage of short Rayleigh range because it produces less convergent beam at the sample cell windows resulting in less windows heating that occurs when long focal length optics is used. The small apparatus also reduces the noise source due to atmospheric absorption that can occur in big apparatus.

Finite element analysis results (Figure 2-4) show that the net effect of scaling down the apparatus on the photothermal signal is insignificant. The signal for the small apparatus is about the same with that of big apparatus. However, the characteristic time constant for small apparatus is about 3 times less than that of large apparatus. Although small focal length optics produces small beam spot size and the signal is expected to increase with reduced beam spot size, the short pathlength due to small sample cell geometry limits the expected increased signal from small apparatus.

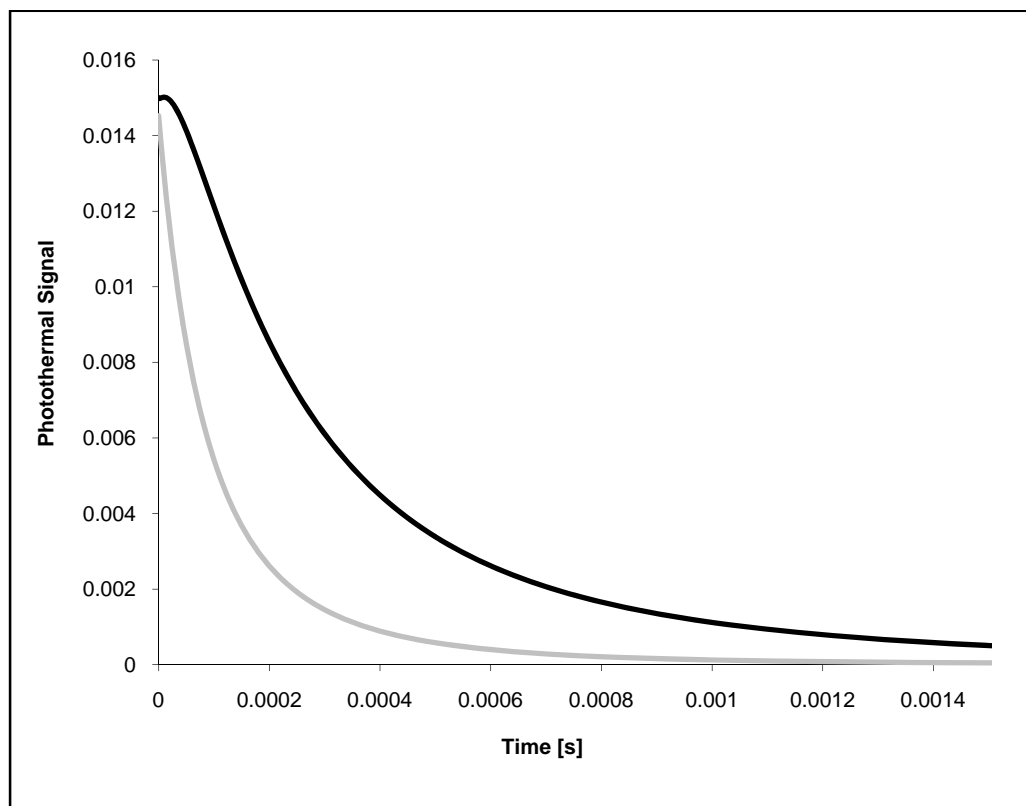


Figure 2-4. Finite element analysis result for time dependent photothermal deflection signal with a gaussian irradiance: — large size apparatus model signal, — small size apparatus model signal. Analyte concentration is assumed the same.

Theory of photothermal deflection shows that the deflection angle also increases with decreased probe beam spot size. This model does not account for varying beam size along excitation axis, the beam size is constant along the pathlength. In other words, the signal for small size apparatus can be increased by further decreasing the probe beam waist.

Data obtained from laboratory measurement were analyzed primarily in terms of the pump laser pulse energy dependence of the photothermal signal and time dependent signal magnitude. Energy dependent signal is an important measurement that shows the correlation between the signal magnitude and the excitation pulse energy by the use of regression techniques. Photothermal signal increases with excitation pulse energy however, nonlinear absorption may also occur due to high irradiance particularly in compounds like fluorocarbons.²⁷ This experiment is performed with relatively low fluence which greatly reduces the nonlinear-absorption effect. Previous studies have shown that nonlinear absorption is reduced in small molecules comprising of big atoms.²⁷ CFC-11 produces linear energy-signal relationship because of its big atomic components coupled with low pulse energy excitation.

Figure 2-5 and Figure 2-6, respectively, show the energy-signal regression curve for large and small size apparatuses. Upon each pulse of the pump laser the photothermal deflection signal magnitude was estimated by using the matched filter and the CO₂ laser energy was monitored with the A/D converter. Two separate data files were recorded during the energy dependent signal experiment; one being the pump laser energy and the other the signal estimate per pulse.

Signals for CFC-11 and ethanol vapors indicate linear relation with both apparatuses for pulse energy of up to about 1 mJ, indicating that the linear range and sensitivity of the small apparatus is comparable with conventional types. The sensitivity and linear range can also be increased by increasing the excitation source intensity.

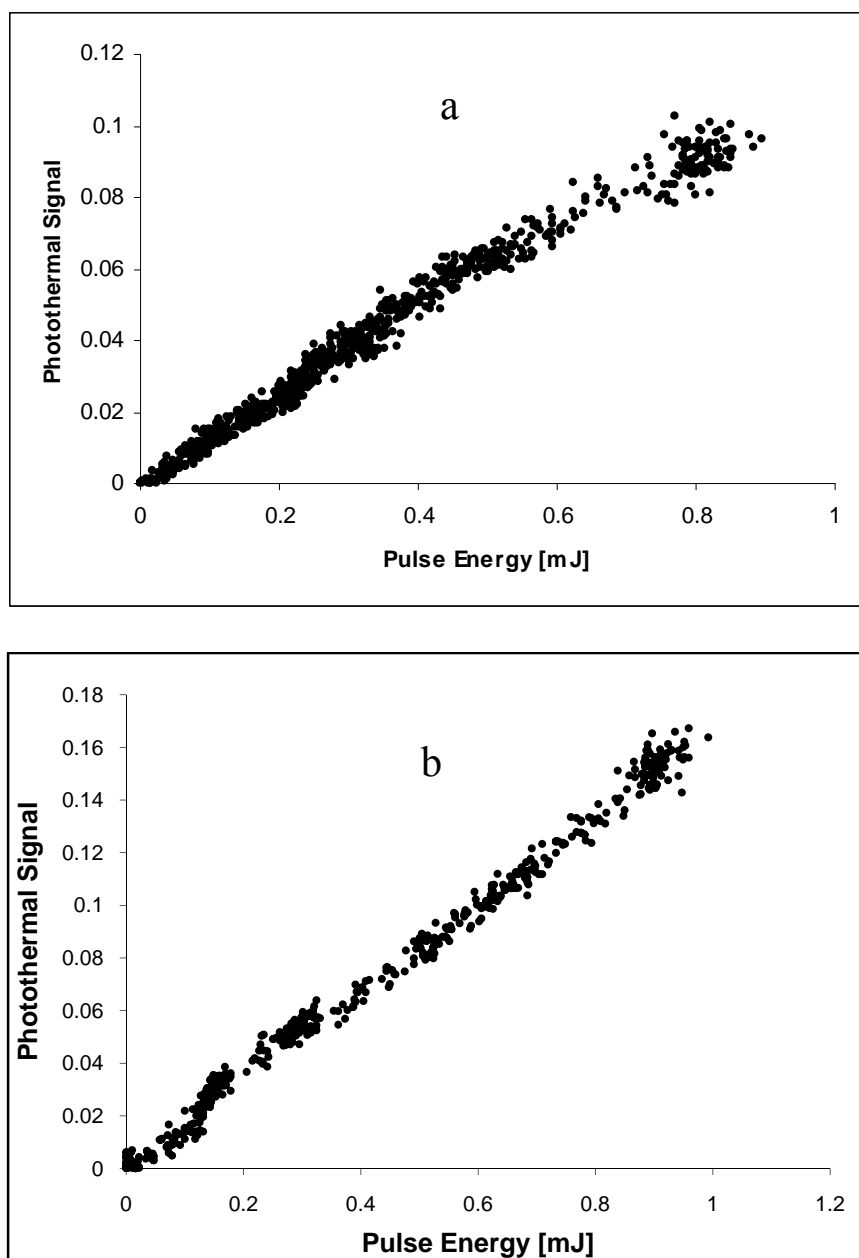


Figure 2-5. Large size apparatus energy dependent photothermal signal for (a) 1 ppmv CFC-11 buffered in nitrogen, (b) 1.5 ppmv 200 % proof ethanol vapor buffered in nitrogen. Excitation wavelength is at 9.3 μm for CFC-11 and 9.54 μm for ethanol. Sample pathlength is 100 mm.

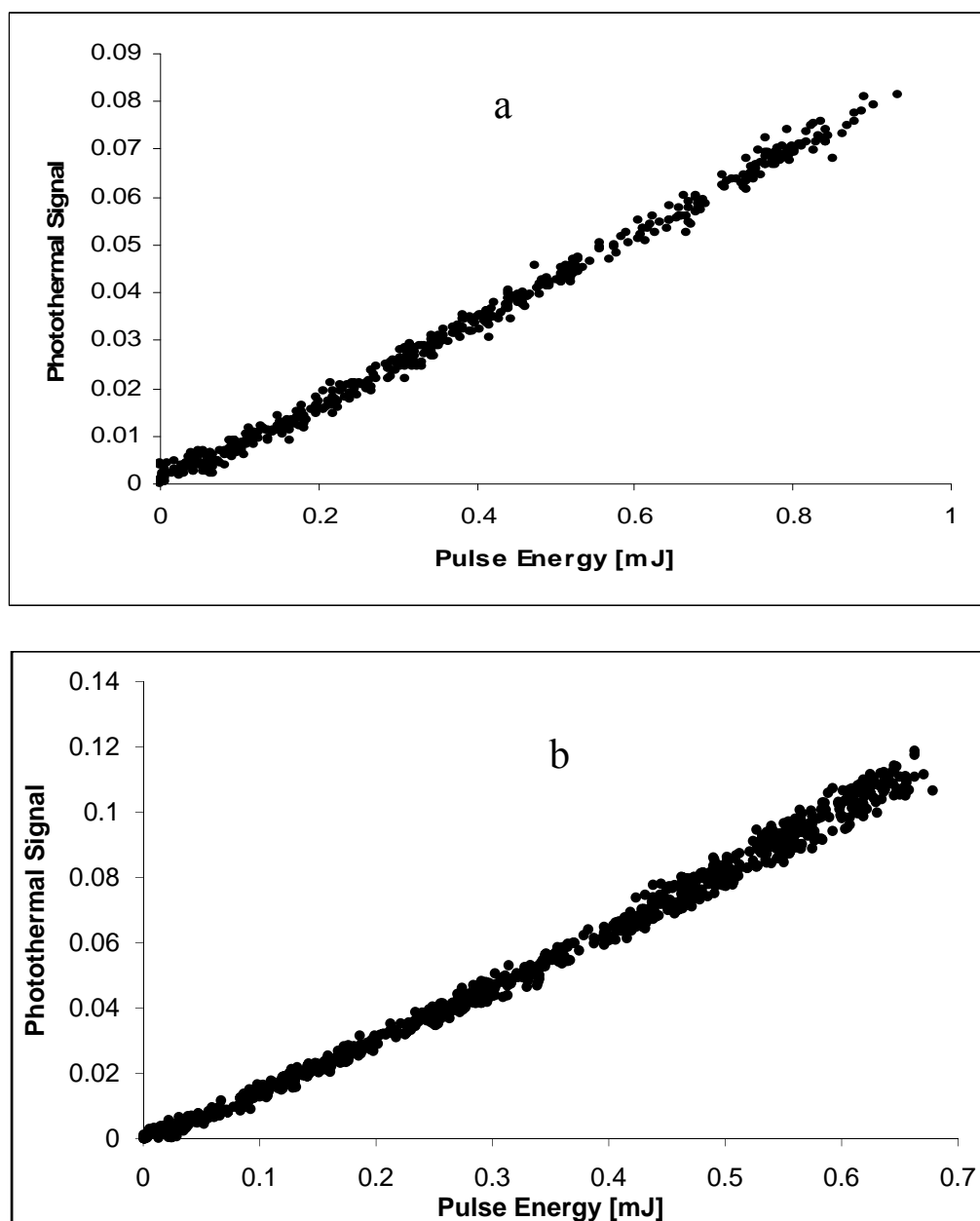


Figure 2-6. Small size apparatus energy dependent photothermal signal for (a) 5 ppmv CFC-11 buffered in nitrogen, (b) 10 ppmv 200 % proof ethanol vapors in nitrogen. Excitation wavelength is at 9.3 μm for CFC-11 and 9.54 μm for ethanol. Sample pathlength is 37 mm.

The signals for small apparatus also show an improvement in terms of signal-to-noise ratio. The S/N for small apparatus is about twice that of large apparatus. Since photothermal deflection angle increases with decreased pump beam spot size, it is expected that the signal from smaller apparatus should be equal, if not higher, to that of the large apparatus because of the short focal length optics used in the smaller apparatus. The relatively lower signal magnitude observed from the small apparatus is primarily due to reduced sample pathlength. The sample pathlength in the small apparatus is about three times less than that of the large apparatus.

Temporal photothermal deflection signals for CFC-11 with both apparatuses are shown in Figure 2-7. The characteristic time constant is short with small apparatus compared with the large apparatus. These results agree with the modeling predicted signal. The advantage of short focal distance optics is that it reduces the time constant and also compensates for the reduced photothermal signal due to short pathlength. The delay in signal rise time for large apparatus is an inherent characteristic of the pump-probe beam offset.

It was mentioned earlier that some difficulties are associated with the use of pulsed infrared lasers when utilized in photothermal spectrometry. The overall results suggest that the small apparatus thus perform well as the conventional laboratory scale apparatus. The results indicate that better improvement can be obtained with the small apparatus by using optimized geometry with appropriate detection and electronics devices.

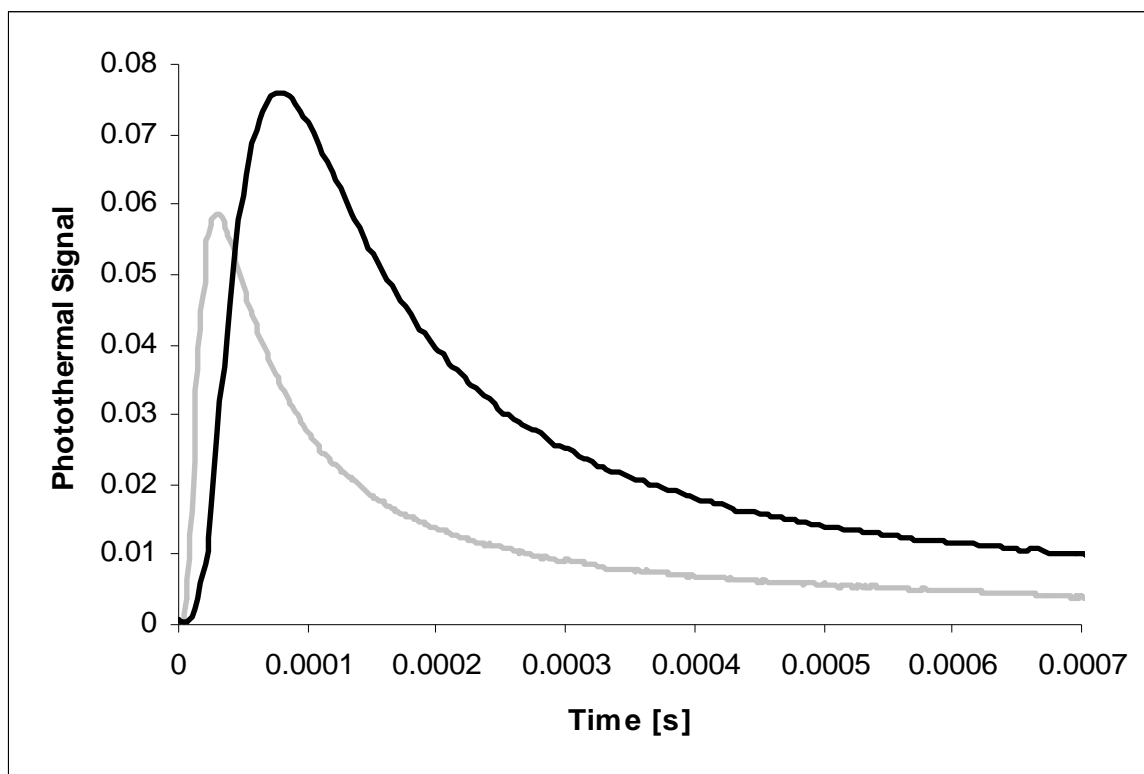


Figure 2-7. Experimental time dependent photothermal deflection signal for large size apparatus time dependent photothermal deflection angle for 1ppmv CFC-11 in nitrogen at 9.3 μm excitation wavelength (black curve), and small size apparatus time dependent photothermal deflection angle for 5 ppmv CFC-11 buffered in nitrogen at 9.3 μm excitation wavelength (gray curve). Pulse energy is 0.8 mJ.

CONCLUSION

A prototype of reduced size photothermal deflection apparatus based on collinear configuration is constructed. The device uses reflective focusing optics. The overall results suggest that prototyped apparatus will perform comparably with convention type.

The apparatus is expected to perform better with well-behaved excitation source and appropriate optical component and signal detection.

REFERENCES

- 1 S. E. Bialkowski, *Photothermal Spectroscopy Methods for Chemical Analysis*. John Wiley and Sons, New York, 1996.
- 2 L. C. Aamodt, and J. C. Murphy, *Journal of Applied Physics*, **52**, (8), 4903-4914 (1981).
- 3 L. C. Aamodt, and J. C. Murphy, *Journal of Applied Physics*, **54**, (2), 581-591 (1983).
- 4 D. Bicanic, S. Kruger, P. Tores, B. Bein, and F. Harren, *Applied Spectroscopy* **43**, (1), 148-153 (1989).
- 5 D. Fournier, and A. C. Boccara, *Photothermal Investigations in Solids and Fluids*. Academic Press, New York, 1989.
- 6 W. B. Jackson, N. M. Amer, A. C. Boccara, and D. Fournier, *Applied Optics* **20**, 1333-1343 (1981).
- 7 J. C. Murphy, and L. C. Aamodt, *Journal of Applied Physics*, **51**, (9), 4580-4588 (1980).
- 8 S. L. Nickolaisen, and S. E. Bialkowski, *Analytical Chemistry* **57**, 758-762 (1985).
- 9 J. A. Sell, *Photothermal Investigation of Solids and Fluids*. Academic Press, New York, 1989.

- 10 O. O. Dada, and S. E. Bialkowski, *Applied Spectroscopy*, **61**, (12) 1373-1378 (2007).
- 11 G. R. Long, and S. E. Bialkowski, *Analytical Chemistry* **57**, 1079-1083 (1985).
- 12 G. R. Long, and S. E. Bialkowski, *Analytical Chemistry* **57**, (6), 1079-1083 (1985).
- 13 G. R. Long, and S. E. Bialkowski, *Analytical Chemistry* **58**, 80-86 (1986).
- 14 D. Korsch, *Reflective Optics*. Academic Press, New York, 1991.
- 15 D. J. Schroeder, *Astronomical Optics*, Second ed., Academic Press, New York, 1999.
- 16 D. T. Allen, E. J. Palen, M. I. Haimov, S. V. Hering, and J. R. Young, *Aerosol Science and Technology* **21**, 325-342 (1994).
- 17 W. P. Arnott, H. Moosmuller, R. E. Abbott, and M. D. Osssofsky, *Review of Scientific Instrument*, **66**, (10), 4827-4833 (1995).
- 18 A. Chartier, and S. E. Bialkowski, *Analytical Chemistry* **67**, 2672-2684 (1995).
- 19 A. Harata, Q. Shen, and T. Sawada, *Annual Review of Physics and Chemistry*, **50**, 193-219 (1999).
- 20 E. L. Lasalle, F. Lepoutre, and J. P. Roger, *Journal of Applied Physics*, **64**, 1-5 (1988).
- 21 A. Mandelis, and R. F. Power, *Applied Optics* **27**, (16), 3397-3407 (1988).
- 22 J. F. Power, and A. Mandelis, *Applied Optics* **27**, (16), 3408-3417 (1988).
- 23 M. A. Schweitzer, and J. F. Power, *Applied Spectroscopy* **48**, (9), 1054-1075 (1994).

- 24 M. A. Schweitzer, and J. F. Power, *Applied Spectroscopy* **48**, (9), 1076-1087 (1994).
- 25 M. A. Shannon, A. A. Rostami, and R. E. Russo, *Journal of Applied Physics*, **71**, (1), 53-63 (1992).
- 26 M. J. Smith, and R. A. Palmer, *Applied Spectroscopy* **41**, (7), 1106-1113 (1987).
- 27 S. E. Bialkowski, and G. R. Long, *Analytical Chemistry* **59**, 873-879 (1987).
- 28 S. E. Bialkowski, *Review of Scientific Instrument*, **58**, (4), 687-695 (1987).
- 29 S. E. Bialkowski, *Analytical Chemistry* **61**, 2479-2483 (1989).
- 30 S. E. Bialkowski, *Analytical Chemistry* **61**, 2483-2489 (1989).
- 31 O. O. Dada, and S. E. Bialkowski, *Applied Spectroscopy* **61**, (12), 1373 (2007).

CHAPTER 3

FINITE ELEMENT ANALYSIS MODELING OF PULSE-LASER EXCITED
PHOTOTHERMAL DEFLECTION (MIRAGE EFFECT) FROM AEROSOLS^b

ABSTRACT

A finite element modeling of photothermal deflection from aerosols collected on a plane surface substrate in air medium is presented in this chapter. The simulation is used to model the heat transfer in air, aerosol, and substrate layers and to predict the temperature gradient in the air above the aerosol. The model is extended to prediction of photothermal deflection signal from laser excited optical beam deflection caused by temperature gradient inside the air above the aerosol. The modeling results show that the dynamics of the temperature gradient in the surrounding air, above aerosol, is dependent on the aerosol's size, shape, and thermo-optical properties as well as the substrate's thermal properties. The results also show that time-dependent photothermal deflection signal amplitude does change with inter-particle heat transfer especially for highly absorbing aerosols. Thus, aerosol analysis with photothermal deflection may require calibration with standard aerosol.

^b Temperature change animation from modeling results are stored in MGD media device that accompanies this dissertation.

INTRODUCTION

Photothermal spectrometry is a novel optical technique that is used to measure low absorbance by probing the refractive index change created in the sample when absorption of electromagnetic radiation and subsequent thermal relaxation occur.¹ When very small absorptions are encountered, photothermal spectroscopy is often the viable alternative.

Photothermal deflection with crossed pump-probe beam geometry (mirage effect) probes the heat diffusion within a sample in an indirect way. A sample is illuminated with modulated electromagnetic radiation of laser source and the thermal waves produced propagate through the sample into the surrounding fluid. This process produces a temperature gradient that causes a change in refractive index of the coupling fluid (air as in this case), which subsequently alters the propagation of a probe beam that passes through the fluid. This phenomenon is analogous to solar heating of a road that creates a temperature gradient inducing the bending of light at oblique angles causing mirages.¹ Thermo-optical properties, as well as the concentration of the sample can be obtained by measuring the phase change in the deflected probe beam. Application of photothermal mirage to studying bulk of various materials is well known but no previous work has been reported on aerosols.

Aerosols are defined as suspensions of liquid or solid particulate matters in a gaseous medium.² Aerosols with aerodynamic diameters less than 2.5 μm are of special concern because they can penetrate deeply into the lung and cause severe health hazards.³ Aerosols are produced by many industrial processes, as well as vehicle emissions. Our

major interest is to chemically characterize aerosols using the “mirage effect” method in laboratory-conducted experiments.

The temperature field for three-layer sample and the associated boundary conditions have been reported in details.^{1,4-11} Schweitzer *et al.* reported the impulse mirage effect detection for optical depth profiling of thin films. The solution to both transverse and normal component of the temperature profile in the coupling fluid was reported for infinite medium as well as thermally discontinuous system. Similar studies with different applications have been reported for layered samples with flat contact with the substrate,^{4-7, 10, 12-17} but the heat transfer processes assumed do not take into consideration spherical sample geometry, as in the case of aerosols, and the analytical signals reported in these studies are mass dependent. It is not clear whether the photothermal deflection signal is aerosol’s mass dependent or surface particle density dependent.

The operating principles of photothermal deflection are well known, but the major uncertainties are: 1) the effects of different particle morphology and surface textures on the analytical signal, 2) dynamics of heat transfer process from the aerosol to the air and the backing substrate. Earliest photothermal investigation of aerosols arose from the thermal blooming problem encountered when high-power laser beam propagates through the atmosphere. Chan¹⁸ showed that the effective absorption coefficient due to aerosols is time dependent. The study reported the analytical solution for the temperature change in the surrounding air by solving the heat conduction equation. However the model is not

applicable to aerosols collected on plane surface because of the discontinuity in the medium, and the spherical symmetry system is no longer valid.

Previous reports on aerosols have focused on the associated heat and mass transfer processes that occur with regards to their influence on the atmosphere when aerosols are heated with a source of light such as lasers.¹⁸⁻²¹ Heating an aerosol with a laser beam induces temperature gradients in the fluid surrounding the particle causing change in fluid's index of refraction in the vicinity of the particle. The amount of energy an aerosol absorbs from the incident light beam depends on the particle's complex index of refraction as well as on its optical size (where the optical size x is given by $x = 2\pi r/\lambda$, r and λ being the particle's radius and laser wavelength, respectively). In this work, the light wavelength considered is much larger than the particle radius; thus the energy absorbed by the particle can be obtained from Rayleigh theory.²²

Aerosols are either in liquid or solid phase but the particles considered are homogeneous condensed-phase aerosol. Therefore the mass transfer phenomenon due to evaporation can be neglected. When the pump beam strikes the particle (which is assumed to be in thermal equilibrium with its surrounding) the excitation energy is deposited into the particle and thus raises the particle's temperature. In the case of short-pulse laser excitation, energy transfer into the particle is instantaneous and the particles can be assumed to possess constant size during the short excitation time. When the laser is turned off, the particle is no longer in equilibrium with its surroundings, and it begins to cool by heat conduction effect (assuming no convective or radiative heat transfer).

Eventually, the particle reaches a new equilibrium at which point its temperature returns to that of its surroundings.

This chapter is focused on the use of numerical modeling to examine the transient heat transfer processes and the subsequent temperature gradient that occur in the surrounding fluid when aerosols deposited on a solid substrate are heated with a pulsed laser. Finite element modeling of temperature distribution of three-layer media comprising coupling fluid (air as in this case), aerosols and the substrate (collection plate) is studied with commercial finite element analysis software (Comsol Multiphysics v 3.3). The system is thermally discontinuous; hence the heat flux propagation from the aerosol into the surrounding air is dependent on the thermal properties of the three media. The solution to the transient temperature change within the media is used to calculate the resulting time-dependent photothermal deflection signal.

First, models of single aerosol are used to investigate the heat transfer process from the aerosol to the surrounding media. The models examine how the aerosol's characteristics such as size, shape, and thermo-optical properties influence the photothermal deflection signal. The models for single aerosol are used also to examine effects of substrate thermal properties on photothermal deflection. Second, multi-aerosol modeling is performed to examine how inter-particle heat transfer, surface particle density and non-uniform surface texture produced by ensembles of particles changes the photothermal deflection.

For the air-aerosol-substrate layers, as shown in Figure 3-1, the following assumptions are made: convective and radiative heat transfer is negligible, the sample is

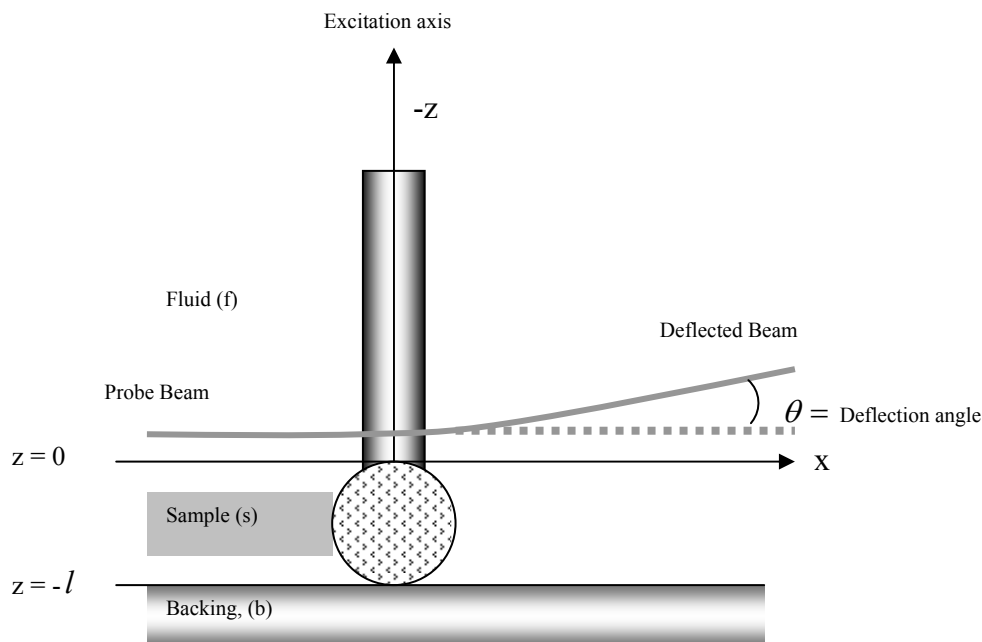


Figure 3-1. Air-aerosol-substrate layers thermal field geometry: The backing is a flat germanium plate which is used to collect aerosols. The deflection angle is measured with a bi-cell position sensing detector.

thermally and elastically isotropic and in good thermal contact with both the fluid and the substrate. It is assumed that the coupling fluid and the backing substrate are optically transparent to the irradiation source and that the contribution from the acoustic wave to the thermal field is negligible.

MATERIALS AND METHOD

Temperature Change Profile. Finite element analysis (FEA) method is used to model the photothermal deflection from aerosols deposited on flat substrate. In all photothermal

methods the key problem is to obtain the differential solution of the temperature change, which depends mostly on the thermo-optical properties of a sample and its thermal and optical structure. To solve this problem, this model uses heat conduction and convection application mode in the Comsol Multiphysics software for the steady and transient heat transfer calculation. Figure 3-2 shows the three-dimensional sub-domain geometry that represents a spherical aerosol deposited on a plane-disc. The substrate and aerosol are assumed to be surrounded by an open ended air medium.

The heat diffusion equation solved by Comsol Multiphysics software in the convection and conduction application is given as

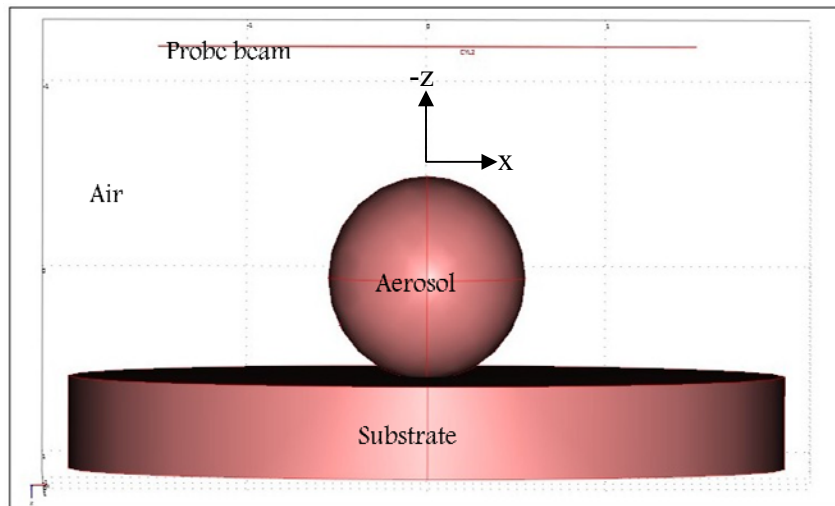


Figure 3-2. Finite element model 3D geometry representing air, aerosol, substrate layers. The geometry shows a spherical aerosol deposited on a flat substrate and the surrounding air.

$$\rho C_p \frac{\partial \delta T}{\partial t} - (k \nabla^2 \delta T) = Q - \rho C_p u \cdot \nabla \delta T \quad (3-1)$$

where ρ (kg m^{-3}) is the density, C_p ($\text{J kg}^{-1} \text{K}^{-1}$) is the heat capacity, δT (K) is the temperature change, k ($\text{W m}^{-1} \text{K}^{-1}$) is the thermal conductivity, u (m s^{-1}) is the flow velocity, and Q (W m^{-3}) is the heat source. This model assumes an incompressible fluid, which means that $\nabla \cdot u = 0$. The aerosol is heated with constant irradiance source and the energy deposited in the aerosol is given as

$$Q = \alpha E e^{(-\alpha l)} \cdot f(t) \quad (3-2)$$

where E (W m^{-2}) is the light source irradiance, α (m^{-1}) is the absorption coefficient for the aerosol at given wavelength. The values of $\alpha = 2676 \text{ m}^{-1}$ (molar absorptivity for ammonium nitrate at $9.56 \mu\text{m}$ wavelength) and $\alpha = 2.676 \times 10^7 \text{ m}^{-1}$ (4th order of low absorption coefficient) are used for low absorbance and high absorbance aerosols respectively. In pulse source case, a gaussian pulse profile is considered and the temporal shape of the pulse is characterized by a function of time $f(t) = \exp[-(t-t_p)^2/t_w^2]$ for $0 \leq t_w \leq t_p$ with pulse width, $t_w = 120 \text{ ns}$. In the case of chopped continuous wave excitation, $f(t)$ is the characteristic modulation profile and is given as

$$f(t) = \begin{cases} 0 \leq t \leq t_o, & 1 \\ t_o \leq t \leq t_{cw}, & 0 \end{cases} \quad (3-3)$$

where $t_{cw} = 2t_o$. The heating source was applied only to the aerosol domain with assumption that the coupling fluid and the substrate have a negligible coefficient of absorption for the electromagnetic radiation. For single spheroid aerosol defined by

$$\frac{x^2}{a^2} + \frac{y^2}{b^2} + \frac{z^2}{c^2} = 1 \quad (3-4)$$

and excitation source propagating along the z -axis in the positive direction, the sample pathlength, $l = z_o + z$. This is to account for varying pathlength across the aerosol. Where z_o is the value of z at the entrance surface of the particle and is given as

$$z_o = \sqrt{c^2 \left(1 - \left(\frac{x^2}{a^2} + \frac{y^2}{b^2} \right) \right)} \quad (3-5)$$

From Eq. 3-4 and 3-5, c is the semi-axis length along z axis, a and b are the semi-axis length along x and y direction, respectively. The diameter and thickness of the substrate are 20 mm and 2 mm respectively for all the models reported. Unless specified, thermal properties of solid ammonium nitrate are used for the aerosols and those of germanium for the substrate (Table 3-1).²³⁻²⁵

The time-dependent temperature profile in the surrounding air is obtained by having the Comsol Multiphysics software solve the thermal diffusion equation (Eq. 3-1) with boundaries conditions set at zero temperature (assuming no convective heat transfer at the surfaces of the aerosol and the substrate).

Table 3-1. Materials and their thermal properties as found in literature.

Material	Heat Capacity [J kg ⁻¹ K ⁻¹]	Thermal Conductivity [W m ⁻¹ K ⁻¹]	Density [kg m ⁻³]
Air	1010	0.0261	1.17
Germanium	320	59.8	5330
Ammonium Nitrate	1740	1.98	1720

This way, the temperature solution represents δT . Since the heat source is made available only in the aerosol-domain, the temperature profile in the coupling air is as a result of heat propagation through the aerosol into the air. In post processing mode the temperature change solution can be visualized in various plot type or animation (see Appendix C).

Optical Beam Deflection. The transfer of energy from the aerosol to the surrounding air produces a refractive index gradient in the air. For small thermal perturbation, the time dependent change in refractive index is given as

$$\delta n(x, y, z, t) = \left(\frac{dn}{dT} \right) \delta T(x, y, z, t) \quad (3-6)$$

where $\delta T(x, y, z, t)$ equals δT as obtained from Eq. 2. The photothermal beam deflection (mirage effect) is as a result of variation in the position of the probe beam along its path.

The time dependent deflection angle is given a

$$\theta(x, y, z, t) = \int_{path} \frac{\partial \delta n}{\partial S_{\perp}} \delta S \quad (3-7)$$

For probe beam propagating along the x direction above the aerosol, the probe beam deflection is in two directions: y and z . Quad-cell or bi-cell position-sensing detector (PSD) is often used to perform photothermal deflection experiment. For this model, photothermal deflection signal calculation assumed bi-cell lateral position-sensing detection method with transverse offset of zero. The photothermal signal is only due to beam deflection with respect to z -axis. Hence, the deflection angle, $\theta(z, t)$, is calculated as

$$\theta(z, t) = \frac{dn}{dT} \int_x \frac{\partial \delta T(x, y, z, t)}{\partial z} dx \quad (3-8)$$

Eq. 3-8 shows that the photothermal deflection is proportional to the spatial derivative of temperature change rather than the temperature profile. In the post-processing mode, the photothermal deflection signal is obtained by using the in-built integration coupling variable in the Comsol Multiphysics software to integrate the first derivative of the temperature change with respect to z along x -axis above the aerosol. For the signal calculation a line or a very thin cylinder is drawn along the x -axis to represent the probe beam. Integration part of Eq. 3-8 is then evaluated on the line or the cylinder. The value of dn/dT for air is $-0.88 \times 10^{-6} \text{ K}^{-1}$.

RESULTS AND DISCUSSION

Figure 3-3 shows the probed temperature change as a function of time at $z = 10 \mu\text{m}$ above $2 \mu\text{m}$ diameter ammonium nitrate aerosol on germanium plate.

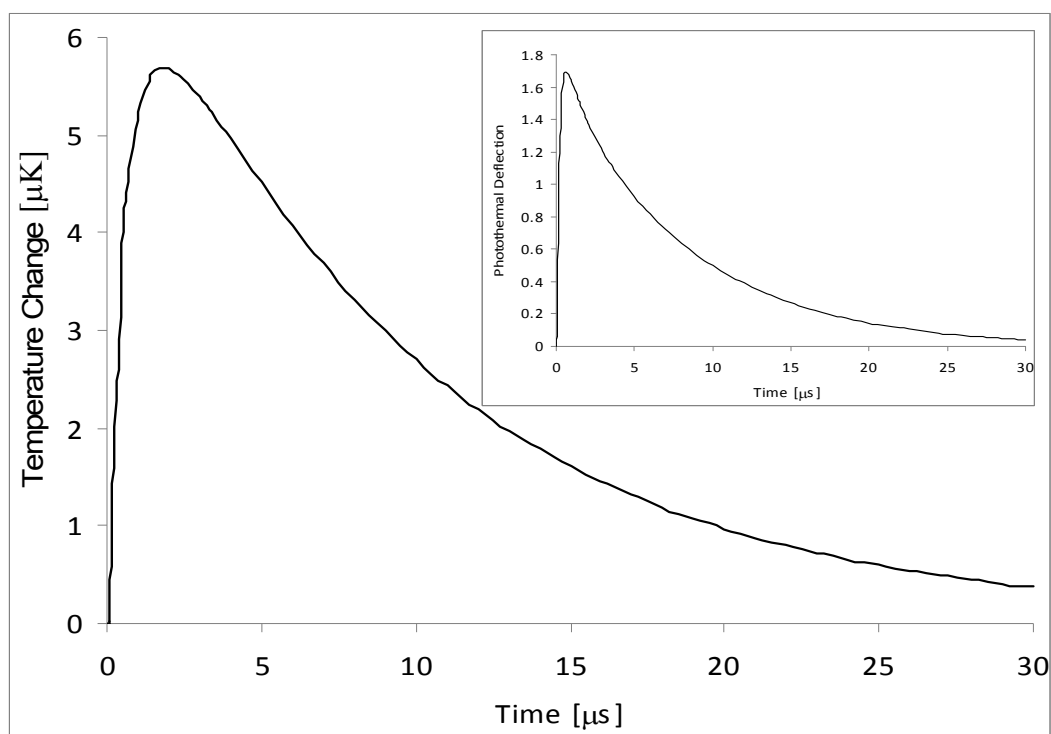


Figure 3-3. Plot of probed time dependent temperature change along x -axis for ammonium nitrate aerosols on germanium plate. The inset is the corresponding photothermal deflection signal (path integral of temperature change first derivative with respect to z)

The corresponding photothermal deflection signal (inset) is obtained by path integral of the first derivative of the temperature change with respect to z . At $t = 0$ a sudden rise in temperature is observed because pulsed heating is assumed to possess temporal pulse profile that is shorter than the characteristic thermal diffusion time of the sample. Figure 3-4 shows the temporal temperature change characterized by pulse

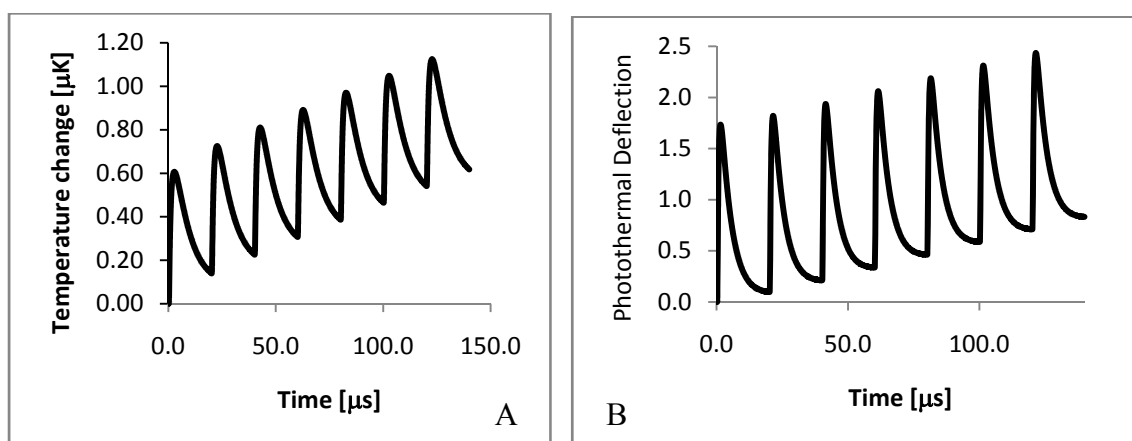


Figure 3-4. (A) Time-dependent temperature change and, (B) the resulting time-dependent photothermal deflection signal at 10 μm above aerosol following first seven excitation pulses with irradiance, $E = 3000 \text{ W m}^{-2}$ at 50 kHz repetition rate. The real signal magnitude is about six orders of magnitude larger than the temperature change magnitude.

repetition frequency of 50 kHz. It is observed that the maximum peak temperature increases with increasing the number of pulses.

Aerosols Optical Absorption. The theoretical photothermal signals (maximum time-dependent photothermal deflection magnitude) for 2 μm ammonium nitrate on germanium plate increase with optical absorption coefficient in a nonlinear fashion due to predominant surface absorption as particles become optically thick (Figure 3-5).

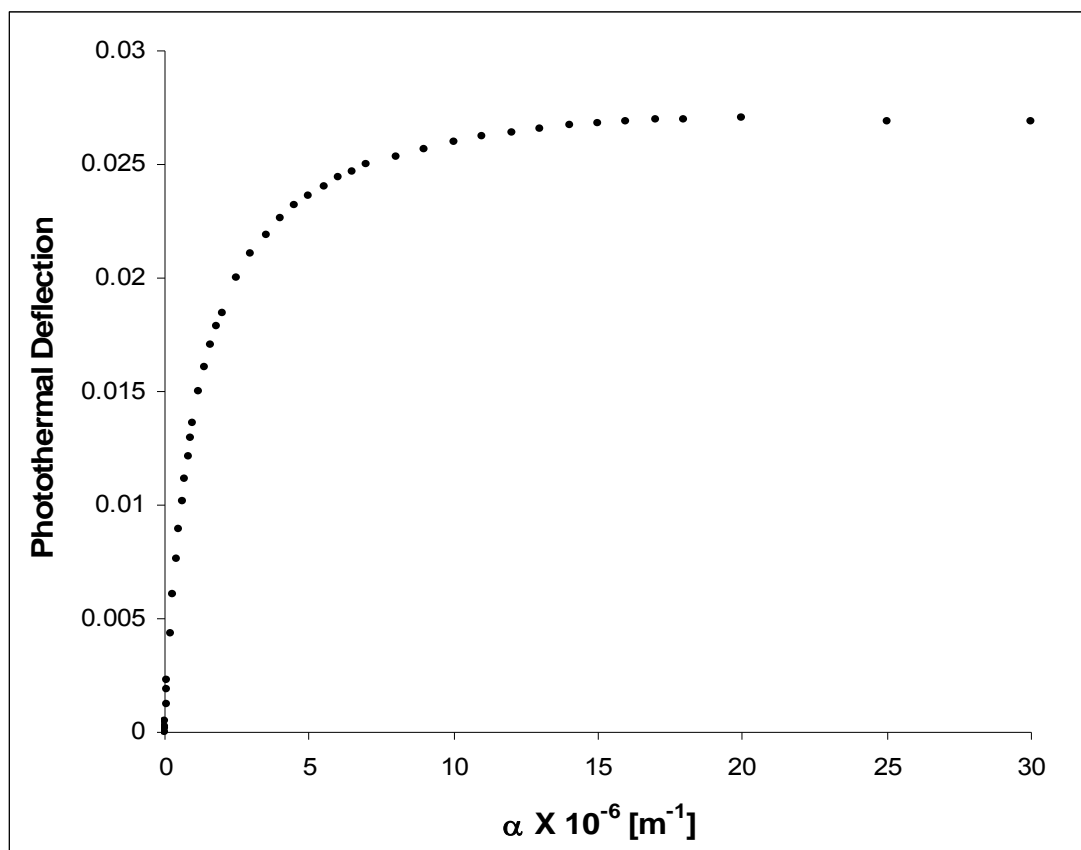


Figure 3-5. Plot of theoretical photothermal deflection signal (maximum time-dependent photothermal deflection magnitude) with aerosols optical absorption coefficient.

Thermal Diffusion. To examine the thermal propagation in the air-aerosol-substrate layer, transient analysis of temperature change is performed by modeling 2 μm diameter spherical ammonium nitrate aerosol on germanium substrate. The temperature change profile appears the same for both low absorbance ($\alpha = 2676 \text{ m}^{-1}$) and high absorbance ($\alpha = 2.676 \times 10^7 \text{ m}^{-1}$) aerosols without considering their magnitudes. Figure 3-6 shows the time-dependent temperature change at the entrance surface of the aerosol.

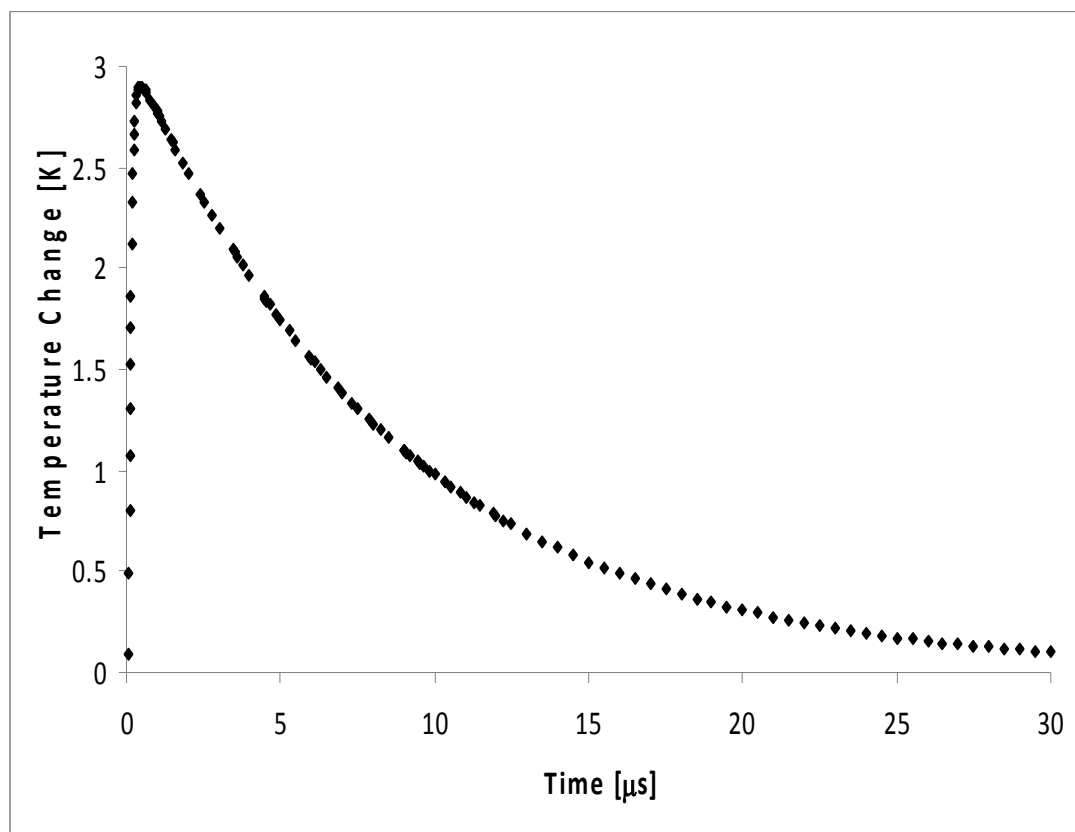


Figure 3-6. Time-dependent temperature change for ammonium nitrate aerosols on germanium substrate at the aerosol's entrance surface ($z = -1 \mu\text{m}$, $x = y = 0$).

Following the aerosol's heating by a pulse source, the aerosol's temperature instantaneously reaches maximum and rapidly cools to thermal equilibrium with the surrounding. Heat subsequently diffuses through the particle into the surrounding media, resulting in temperature gradient in the surrounding air. Figure 3-7 shows the transient temperature change inside the air at $10 \mu\text{m}$ above the aerosol and $10 \mu\text{m}$ into the substrate following heat transfer by the aerosol.

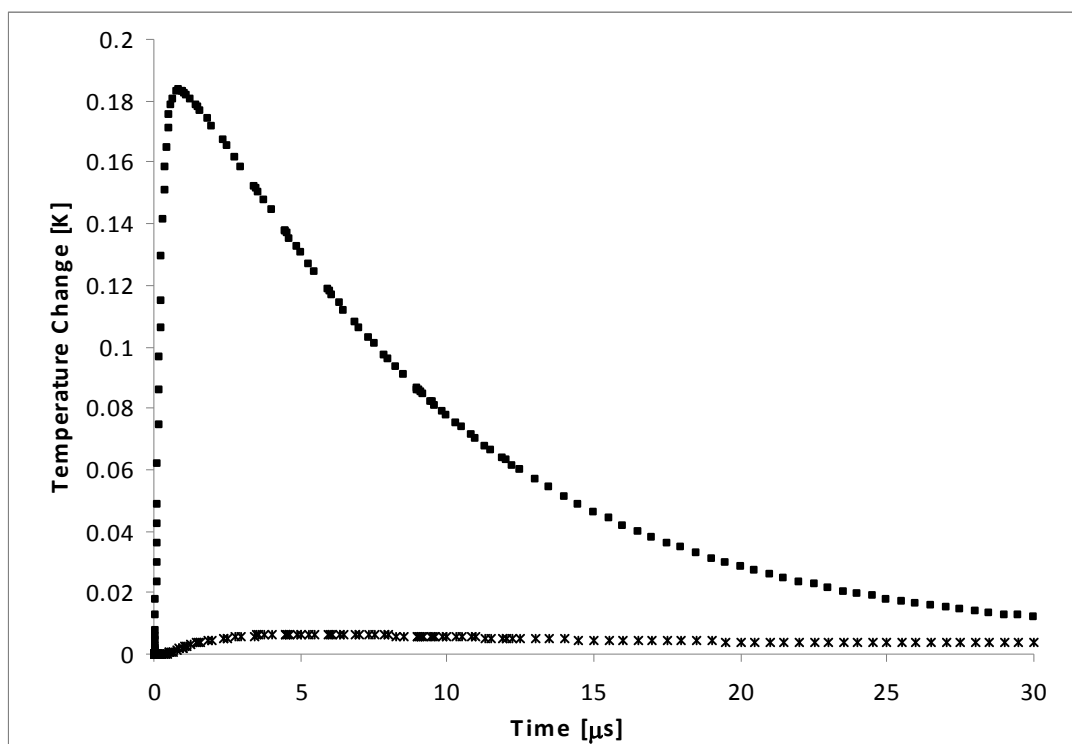


Figure 3-7. Time-dependent temperature change for ammonium nitrate aerosols on germanium substrate at distance $z = 10 \mu\text{m}$ above aerosol (top) and $z = 10 \mu\text{m}$ into substrate (bottom).

Solutions to both axial and transverse temperature change were obtained at time $t = 2 \mu\text{s}$ following the excitation. Figure 3-8 shows the temperature profile along z -axis (axial temperature change) from $6 \mu\text{m}$ above the aerosol, through the aerosol, to $6 \mu\text{m}$ into the substrate. The distance $z = -1 \mu\text{m}$ in Figure 3-8 is the entrance surface of the aerosol. The relative depth of the temperature change into substrate is dependent on factors like aerosol's absorption coefficient, aerosol-substrate contact area, and substrate's thermal properties.

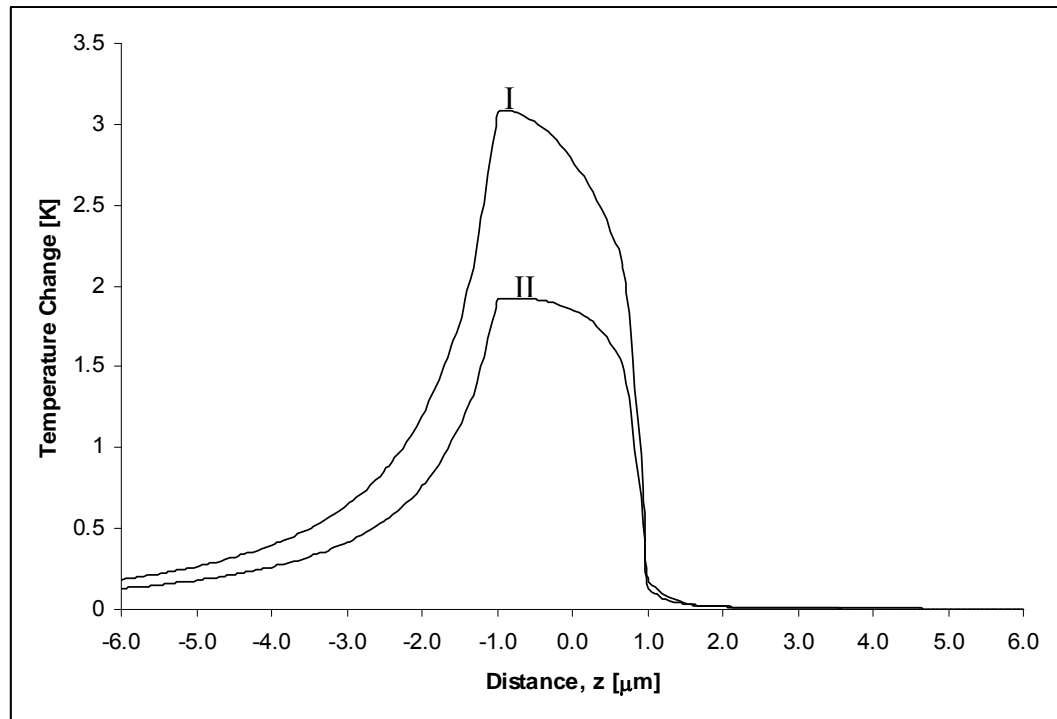


Figure 3-8. Adjusted temperature profile along z -axis at $t = 2 \mu\text{s}$ following pulse laser heating, distance $z = -1 \mu\text{m}$ is aerosol's top surface for: I. high absorbance aerosol, $\alpha = 2.676 \times 10^7 \text{ m}^{-1}$; II. low absorbance aerosol, $\alpha = 2676 \text{ m}^{-1}$. (particle diameter is $2 \mu\text{m}$, irradiance, $E = 3000 \text{ W m}^{-2}$)

The temperature change profile along x -axis (transverse temperature change) at $z = 6 \mu\text{m}$ above the aerosol is shown in Figure 3-9. The transverse temperature distribution appears to be gaussian in form.

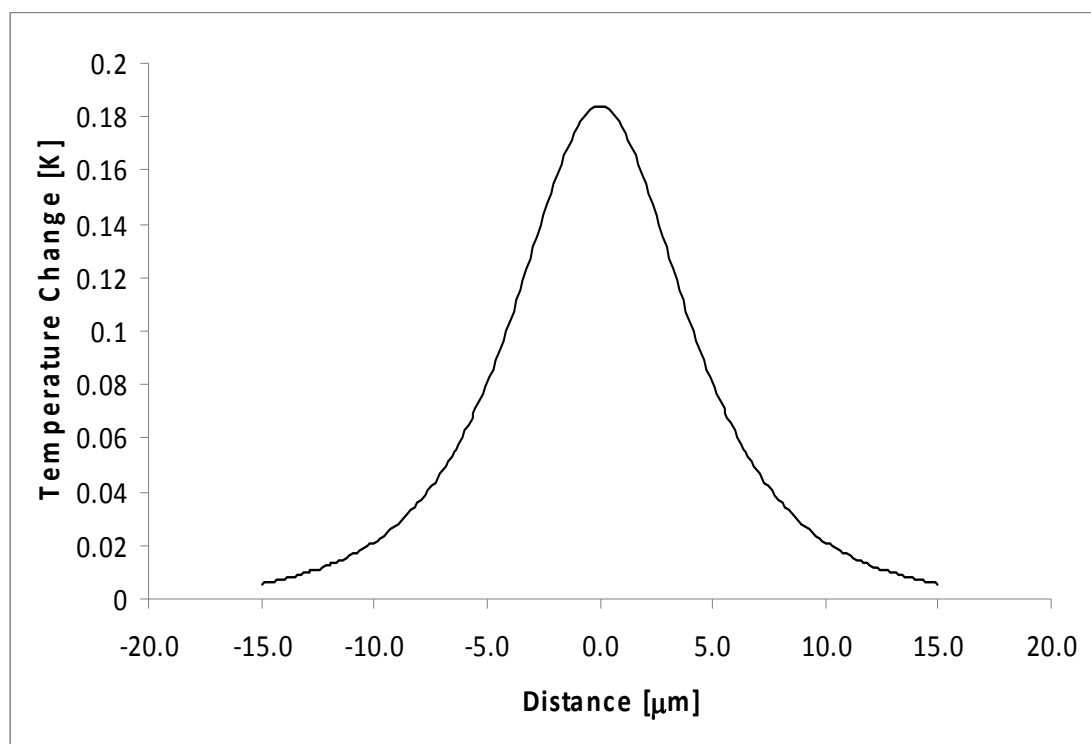


Figure 3-9. Transverse temperature change profile along x -axis at $z = 6 \mu\text{m}$ above aerosol for both high absorbance aerosol, $\alpha = 2.676 \times 10^7 \text{ m}^{-1}$; and low absorbance aerosol, $\alpha = 2676 \text{ m}^{-1}$. (particle diameter is $2 \mu\text{m}$, irradiance, $E = 3000 \text{ W m}^{-2}$)

Aerosols Size and Shape. Since atmospheric aerosols are generally non-uniform in size (polydisperse aerosols) and shape, it is important to know how the aerosol's size and shape affect the photothermal deflection signal. The effect of aerosol's size on the photothermal deflection signal is investigated by comparing the photothermal deflection signal from single spherical aerosol of various diameters. The model uses ammonium nitrate aerosol on germanium substrate. The estimated theoretical signal (maximum

magnitude of time-dependent photothermal signal) for different aerosol's size is then plotted against aerosol's diameter.

For low absorbance ($\alpha = 2676 \text{ m}^{-1}$) aerosols the theoretical signal increases with log of aerosol's diameter as shown in Figure 3-10, though the absorbed energy supposed to increase with increase in size since aerosol cross section area is proportional to size. The regression line is a log fit of signal with size. The variance in the plot is mainly due to calculation error.

Perhaps we can assume that Figure 3-10 possesses two linear trends; one for aerosols with less than $10 \mu\text{m}$ in diameter, and the other for aerosols greater than $10 \mu\text{m}$ diameter. However, aerosol's sizes of interest are those below $10 \mu\text{m}$ therefore the signal-size relationship can still be considered linear for this range. At this point, the only reason for the overall non-linear relationship may be attributed to increased aerosol-to-air-to-substrate thermal interaction as the aerosols grow in size. This effect is not due to increase in aerosol scattering with particles size because scattering does not create a temperature gradient; no index change in the surrounding air is created.

In contrast, a linear relationship is seen between the theoretical signal and aerosol's diameter for high absorbance ($\alpha = 2.676 \times 10^7 \text{ m}^{-1}$) aerosols (Figure 3-11). This is mainly because, as mentioned earlier, increase in aerosol's cross section will result in increased absorbed energy. Furthermore, the absorption in high absorbance aerosols is mainly at the surface which tends to reduce thermal interaction between the aerosol and the substrate.

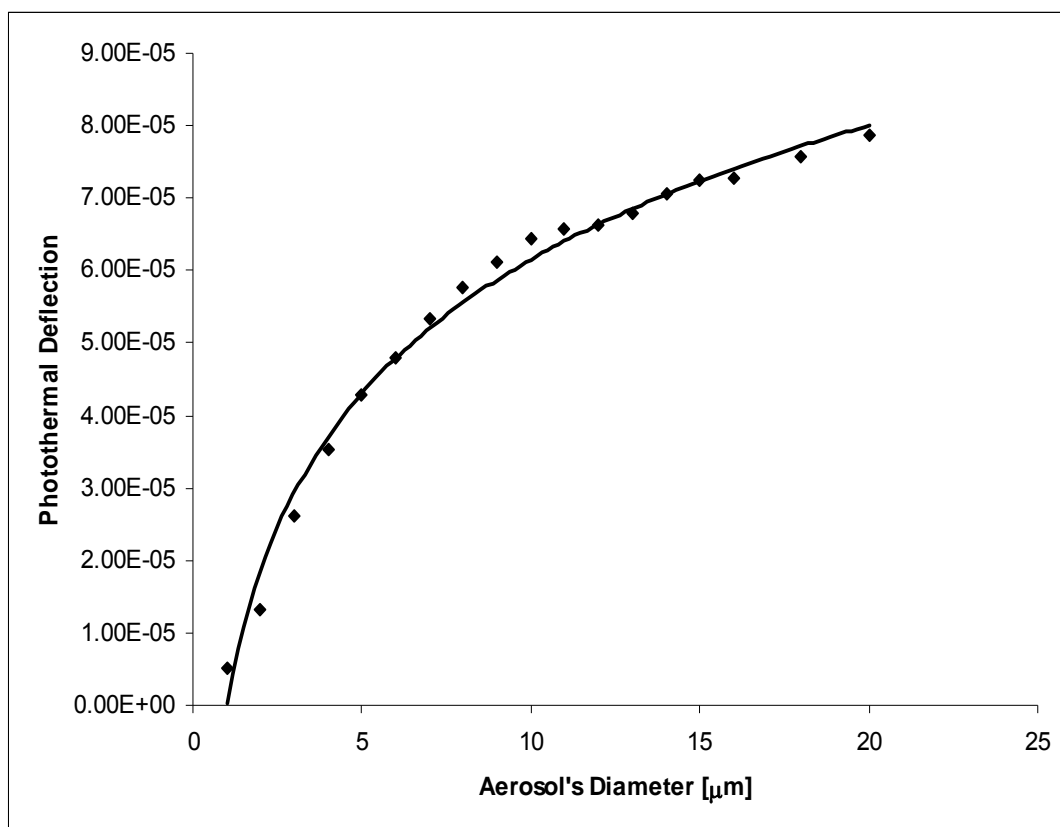


Figure 3-10. The plot of theoretical photothermal deflection signal (maximum time-dependent photothermal deflection magnitude) with aerosol's diameter for ammonium nitrate aerosols on germanium plate showing the effects of aerosol's size on photothermal signal for low absorbance, $\alpha = 2676 \text{ m}^{-1}$, aerosol. Irradiance, $E = 3000 \text{ W m}^{-2}$.

Aerosol's shape effect is examined by comparing model results for a prolate ($z = 1.5625 \mu\text{m}$, $a = b = 0.8 \mu\text{m}$ in Eq. 2), spherical ($z = a = b = 1 \mu\text{m}$ in Eq. 2), and oblate ($z = 0.4096 \mu\text{m}$, $a = b = 1.5625 \mu\text{m}$ in Eq. 2) aerosols of equal volume.

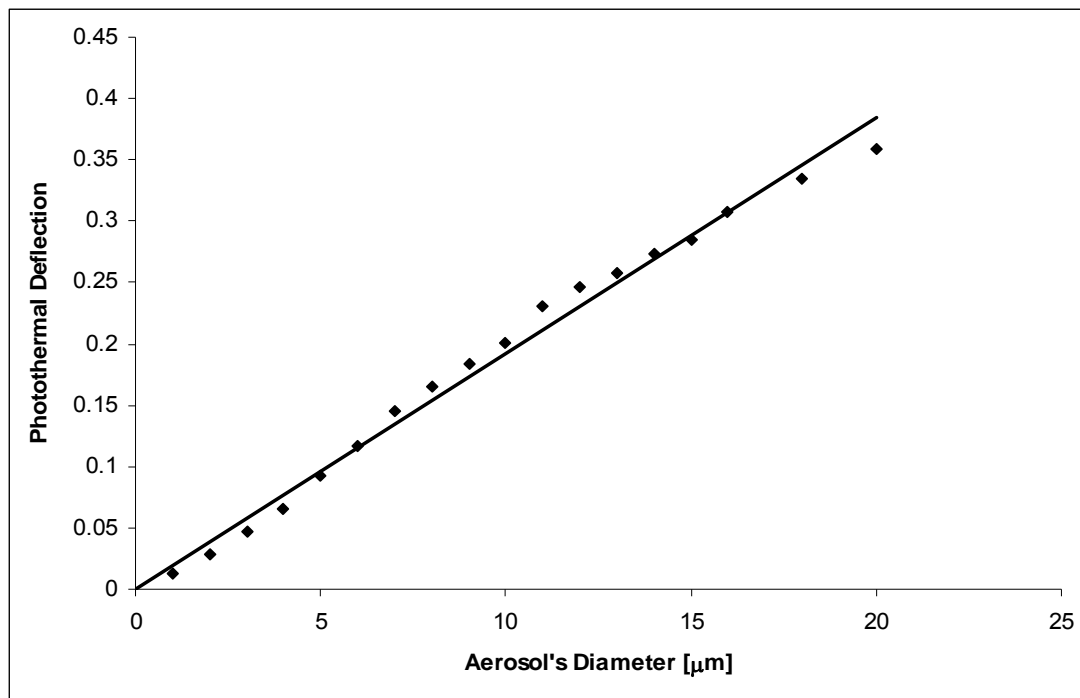


Figure 3-11. Plot of theoretical photothermal deflection signal (maximum time dependent photothermal deflection magnitude) with aerosol's diameter for ammonium nitrate aerosols on germanium plate showing the effects of aerosol's size on photothermal signal for high absorbance, $\alpha = 2.676 \times 10^7 \text{ m}^{-1}$, aerosol. Irradiance, $E = 3000 \text{ W m}^{-2}$).

Figure 3-12 shows that the results are about the same in magnitude and profile for spherical and prolate aerosols. Signal reduction is observed with oblate aerosol which may be due to increased contact heat conductance between the aerosol and the substrate. Increase in aerosol-substrate contact area will increase the contact heat conductance between the aerosol and the substrate, thus increasing the heat transfer rate from aerosol into the substrate. Prolate and spherical aerosols have less contact area with the substrate

(point source contact). Hence most of the heat is transferred into the air since the aerosol-air contact conductance area is much larger than the aerosol-substrate contact conductance area. These observations are similar to those reported by Kumar *et al.*²⁶ on thermal contact conductance for cylindrical and spherical contacts. The authors have shown in their report that the contact conductance for sphere-flat and cylinder-flat contacts is about an order of magnitude lower than for flat-flat contact.

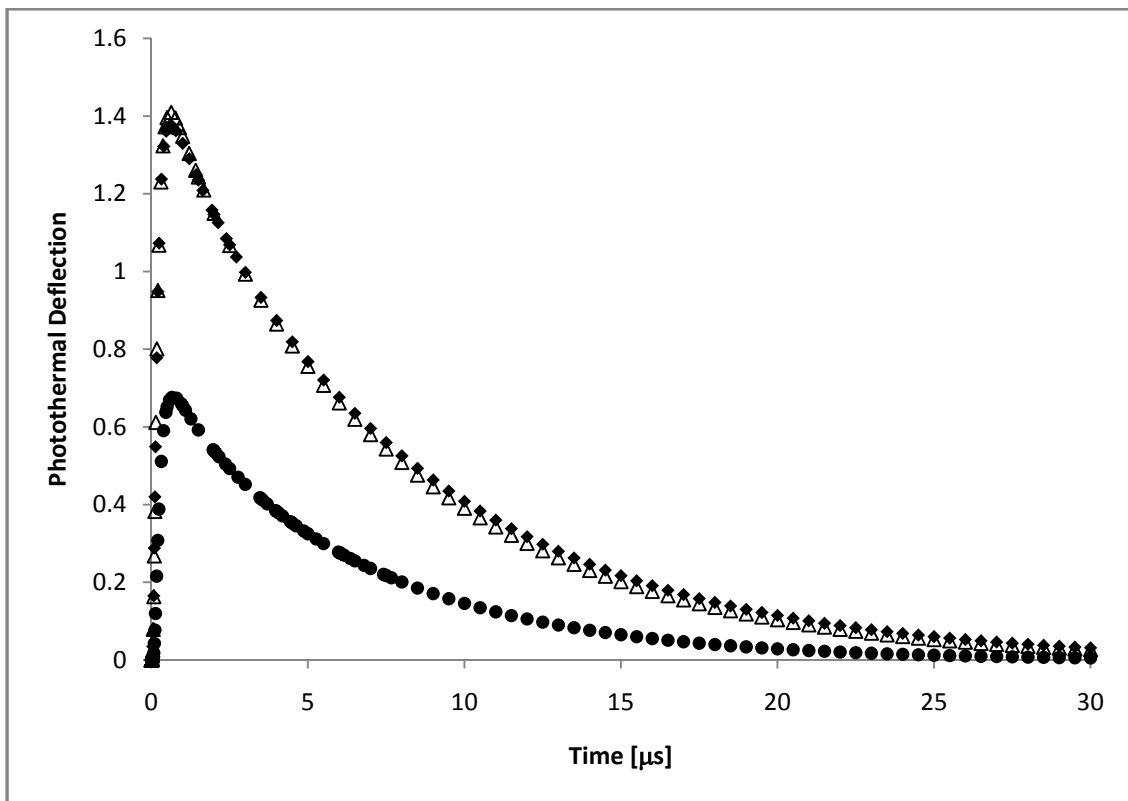


Figure 3-12. Time-dependent photothermal deflection signal for: ■ spherical aerosol, Δ prolate aerosol, ● oblate aerosol.

Aerosols Thermal Properties. The effect of aerosol's heat capacity and thermal conductivity on the photothermal deflection signal is investigated by changing the aerosol's properties relative to that of air. The aerosol's diameter is $2\ \mu\text{m}$ and the density is $1720\ \text{kg}\ \text{m}^{-3}$. The substrate's properties are those for germanium. Change in photothermal deflection signal with respect to change in one of the aerosol's properties is obtained by varying the property of interest while the other is held constant.

Low absorbance ($\alpha = 2676\ \text{m}^{-1}$) aerosols show no significant change in photothermal deflection magnitude with change in aerosol's heat capacity and thermal conductivity except when heat capacity changes by an order of magnitude less than that of the surrounding air (Figure 3-13 and Figure 3-14). However, the signal's decay time increases with increased aerosol's heat capacity and decreases with thermal conductivity. Increased signal decay time with heat capacity is due to reduced rate of cooling in the air. High aerosol's heat capacity means slow rate of heat transfer within the aerosol resulting in decreased signal decay time. When the aerosol's thermal conductivity increases, rate of temperature change in the air increases and the signal decay time becomes less.

For high absorbance ($\alpha = 2.676 \times 10^7\ \text{m}^{-1}$) aerosols, no significant change is observed in the photothermal signal decay time with change in aerosol's heat capacity and thermal conductivity due to relatively less aerosol-to-substrate heat transfer (Figure 3-15 and Figure 3-16). The photothermal deflection signal increases with aerosol's heat capacity because and decreases with aerosol's thermal conductivity. The thermal energy transfer from aerosol's surface into the bulk part of the aerosol decreases with its heat capacity.

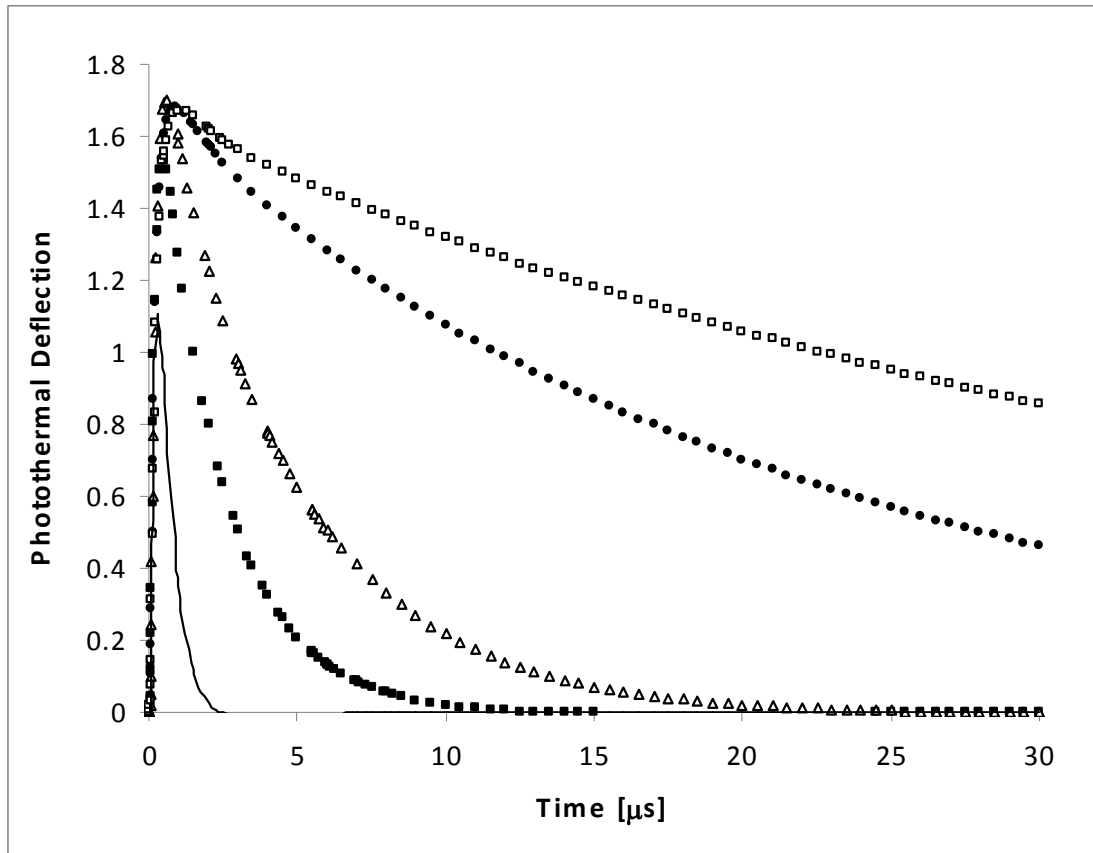


Figure 3-13. The plot of time-dependent photothermal deflection signal showing the effects of aerosol's heat capacity for different ratio of aerosol's heat capacity to heat capacity of air with low absorbance aerosols; \square 0.1, \blacksquare 0.5, \triangle 1, \bullet 5, \square 10 ($k_s = 59.8 \text{ W m}^{-1} \text{ K}^{-1}$, $C_{ps} = 320 \text{ J kg}^{-1} \text{ K}^{-1}$, $\rho_s = 5330 \text{ kg m}^{-3}$, $k_p = 1.8 \text{ W m}^{-1} \text{ K}^{-1}$, $\rho_p = 1720 \text{ kg m}^{-3}$, $k_a = 0.0261 \text{ W m}^{-1} \text{ K}^{-1}$, $C_{pa} = 1010 \text{ J kg}^{-1} \text{ K}^{-1}$, and C_{pp} is varied relative to C_a . where subscripts p , s , and a stand for particle, substrate, and air. Irradiance, $E = 3000 \text{ W m}^{-2}$)

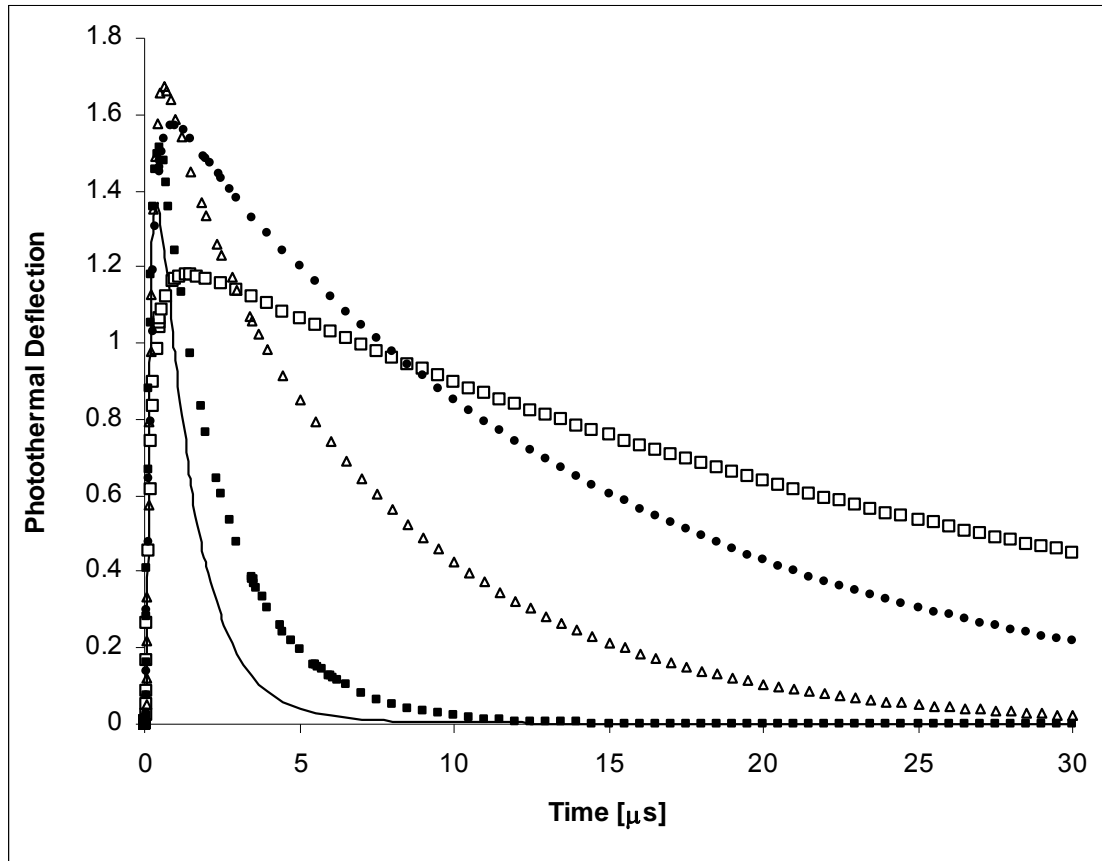


Figure 3-14. The plot of time-dependent photothermal deflection signal showing the effects of aerosol's thermal conductivity for different ratio of aerosol's thermal conductivity to thermal conductivity of air with low absorbance aerosols; \square 1, \bullet 10, Δ 100, \blacksquare 1000, $-$ 10000 ($k_s = 59.8 \text{ W m}^{-1}\text{K}^{-1}$, $C_{ps} = 320 \text{ J kg}^{-1} \text{ K}^{-1}$, $\rho_s = 5330 \text{ kg m}^{-3}$, $C_{pp} = 1740 \text{ J kg}^{-1} \text{ K}^{-1}$, $\rho_p = 1720 \text{ kg m}^{-3}$, $k_a = 0.0261 \text{ W m}^{-1} \text{ K}^{-1}$, $C_{pa} = 1010 \text{ J kg}^{-1} \text{ K}^{-1}$, and k_p is varied relative to k_a . where subscripts p , s , and a stand for particle, substrate, and air. Irradiance, $E = 3000 \text{ W m}^{-2}$).

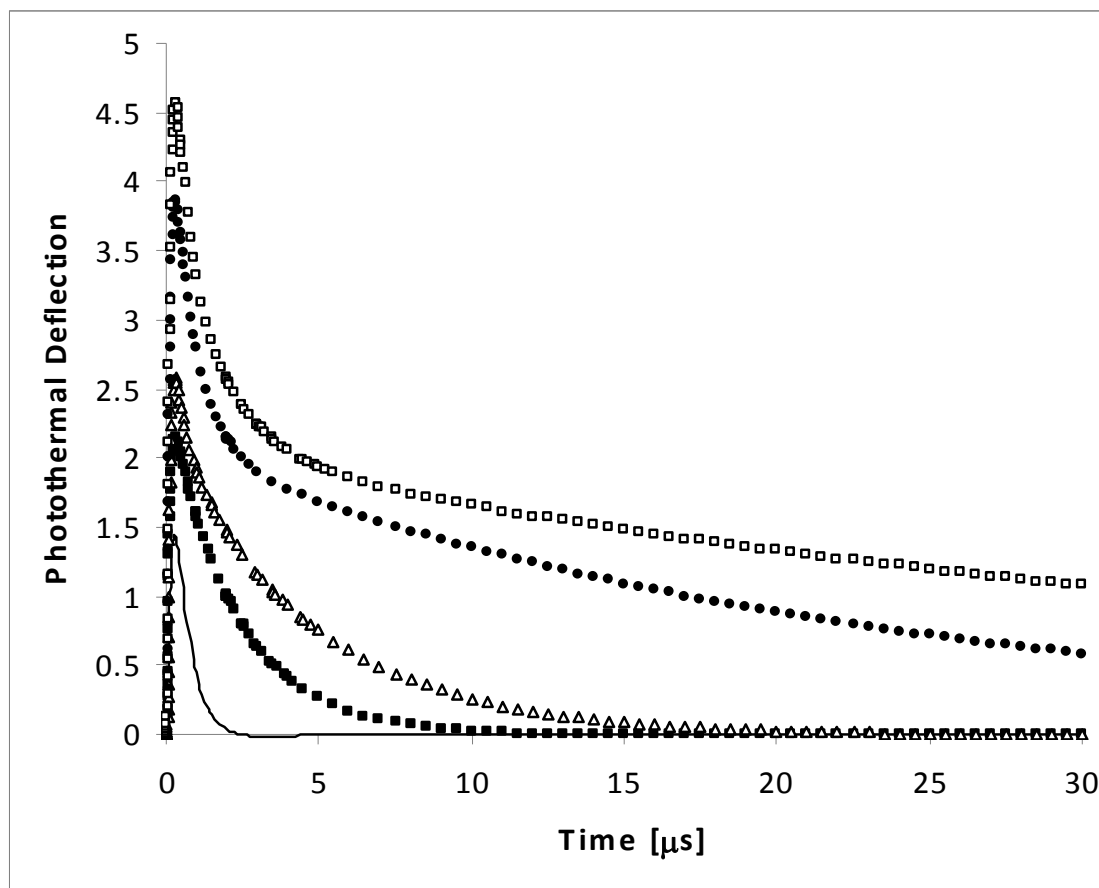


Figure 3-15. The plot of time-dependent photothermal deflection signal showing the effects of aerosol's heat capacity for different ratio of aerosol's heat capacity to heat capacity of air with high absorbance aerosols; --- 0.1, \blacksquare 0.5, \triangle 1, \bullet 5, \square 10 ($k_s = 59.8 \text{ W m}^{-1} \text{ K}^{-1}$, $C_{ps} = 320 \text{ J kg}^{-1} \text{ K}^{-1}$, $\rho_s = 5330 \text{ kg m}^{-3}$, $k_p = 1.8 \text{ W m}^{-1} \text{ K}^{-1}$, $\rho_p = 1720 \text{ kg m}^{-3}$, $k_a = 0.0261 \text{ W m}^{-1} \text{ K}^{-1}$, $C_{pa} = 1010 \text{ J kg}^{-1} \text{ K}^{-1}$, and C_{pp} is varied relative to C_a . where subscripts p , s , and a stand for particle, substrate, and air. Irradiance, $E = 3000 \text{ W m}^{-2}$)

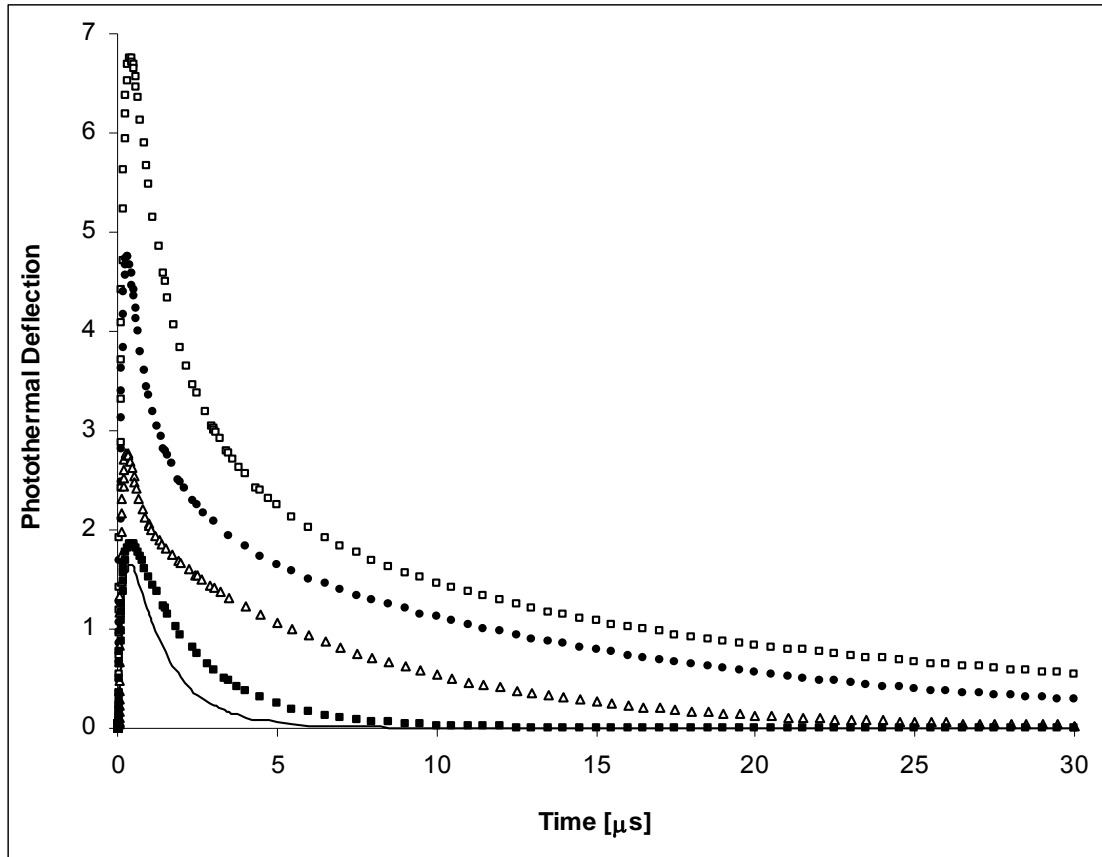


Figure 3-16. The plot of time-dependent photothermal deflection signal showing the effects of aerosol's thermal conductivity for different ratio of aerosol's thermal conductivity to thermal conductivity of air with high absorbance aerosols; \square 1, \bullet 10, Δ 100, \blacksquare 1000, $-$ 10000 ($k_s = 59.8 \text{ W m}^{-1}\text{K}^{-1}$, $C_{ps} = 320 \text{ J kg}^{-1} \text{ K}^{-1}$, $\rho_s = 5330 \text{ kg m}^{-3}$, $C_{pp} = 1740 \text{ J kg}^{-1} \text{ K}^{-1}$, $\rho_p = 1720 \text{ kg m}^{-3}$, $k_a = 0.0261 \text{ W m}^{-1} \text{ K}^{-1}$, $C_{pa} = 1010 \text{ J kg}^{-1} \text{ K}^{-1}$, and k_p is varied relative to k_a where subscripts p , s , and a stand for particle, substrate, and air. Irradiance, $E = 3000 \text{ W m}^{-2}$).

Substrate Thermal Properties. Following aerosol's excitation with pulsed laser, the generated thermal field propagates into both the substrate and the surrounding air. In order to examine how the characteristics (heat capacity and thermal conductivity) of the substrate influence the photothermal signal, models for 2 μm diameter particle with different substrate properties are performed. The properties of aerosol are those for ammonium nitrate. The influence of each of these properties on the photothermal signal is obtained by varying one of the properties while the other is fixed. Substrate's density used is 5330 kg m^{-3} .

No significant change is seen in photothermal deflection magnitude and signal time-constant for high absorbance ($\alpha = 2.676 \times 10^7 \text{ m}^{-1}$) aerosols when substrate's heat capacity is varied owing to less heat transfer from aerosol to substrate. However, slight changes occur in signal magnitude for low absorbance aerosols ($\alpha = 2676 \text{ m}^{-1}$) with change in substrate's heat capacity (Figure 3-17). Absorption occurs in the bulk part of low absorbance aerosol and the heat transfer from aerosol to substrate is relatively high. The temperature change depth into the substrate is therefore higher than that which occurs in high absorbance aerosols.

Substrate's thermal conductivity affects signal decay time for both low and high absorbance aerosols but has no effect on signal magnitude (Figure 3-18 and Figure 3-19). The results indicate that the signal decay time decreases with increased substrate's thermal conductivity. Decrease in substrate's thermal conductivity decreases the rate of heat transfer within the substrate resulting in less heat transfer from air into the substrate that decreases signal decay time. The complex change in decay time with high

absorbance aerosol, as in Figure 3-18, may be due to thermal coupling from the aerosol to substrate through the air.

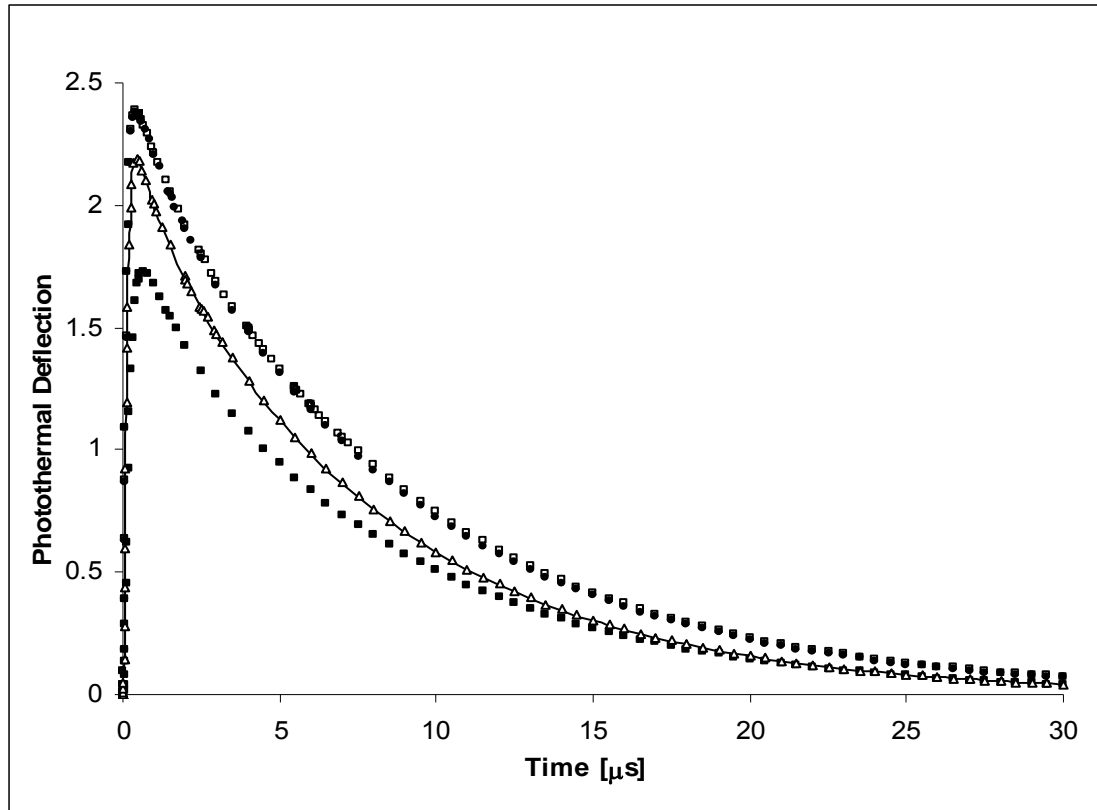


Figure 3-17. Plot of time-dependent photothermal deflection signal showing how substrate's thermal properties influence photothermal signal for different substrate's heat capacity relative to heat capacity of air with low absorbing aerosol; \square 0.1, \circ 0.5, \blacktriangle 1, $-$ 5, \blacksquare 10 ($k_p = 1.8 \text{ W m}^{-1} \text{ K}^{-1}$, $C_{pp} = 1740 \text{ J kg}^{-1} \text{ K}^{-1}$, $\rho_p = 1720 \text{ kg m}^{-3}$, $k_s = 59.8 \text{ W m}^{-1} \text{ K}^{-1}$, $\rho_s = 5330 \text{ kg m}^{-3}$, $k_a = 0.0261 \text{ W m}^{-1} \text{ K}^{-1}$, $C_{pa} = 1010 \text{ J kg}^{-1} \text{ K}^{-1}$, and C_{ps} is varied relative to C_{pa} . where subscripts p , s , and a stand for particle, substrate, and air. Irradiance, $E = 3000 \text{ W m}^{-2}$).

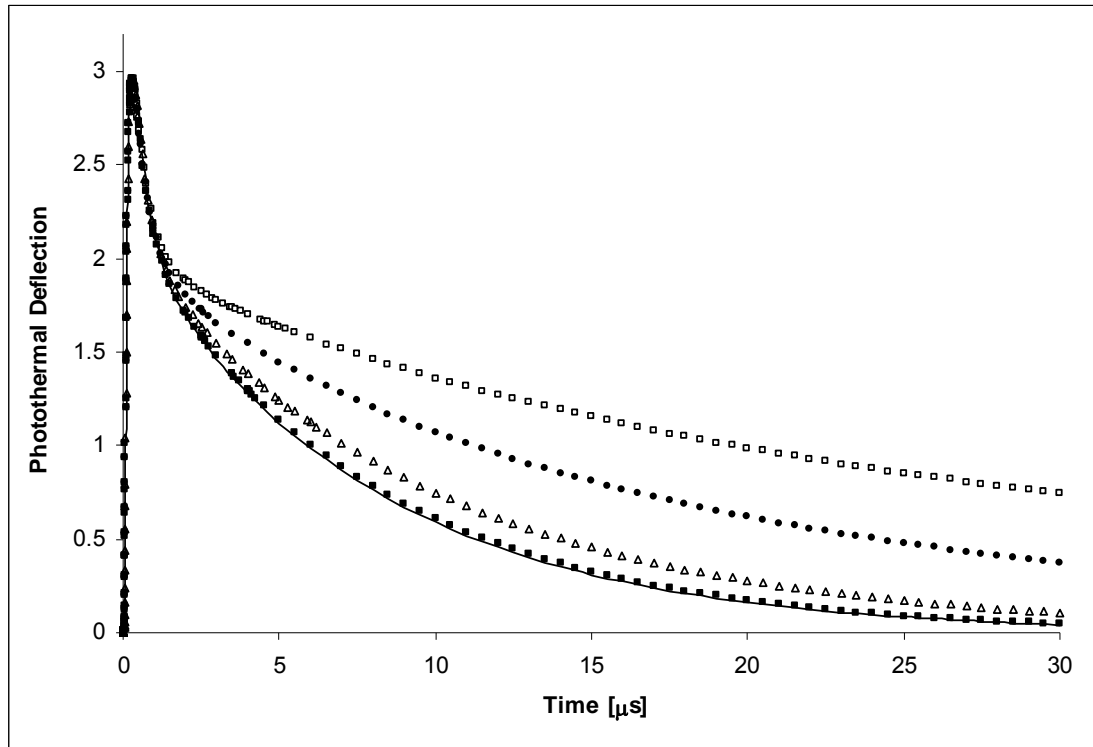


Figure 3-18. Plot of time-dependent photothermal deflection signal showing how substrate's thermal properties influence photothermal signal for different ratio of substrate's thermal conductivity to thermal conductivity of air with high absorbing aerosol; \square 1, \bullet 10, Δ 100, \blacksquare 1000, $-$ 10000 ($k_p = 1.8 \text{ W m}^{-1} \text{ K}^{-1}$, $C_{pp} = 1740 \text{ J kg}^{-1} \text{ K}^{-1}$, $\rho_p = 1720 \text{ kg m}^{-3}$, $C_{ps} = 320 \text{ J kg}^{-1} \text{ K}^{-1}$, and $C_{pa} = 1010 \text{ J kg}^{-1} \text{ K}^{-1}$, $k_a = 0.0261 \text{ W m}^{-1} \text{ K}^{-1}$, $\rho_s = 5330 \text{ kg m}^{-3}$, k_s is varied relative to k_a where subscripts p , s , and a stand for particle, substrate, and air. Irradiance, $E = 3000 \text{ W m}^{-2}$).

All else equal, it may be assumed that substrate's thermal properties have a role to play in the heat transfer dynamics in the air-aerosol-substrate layer. The results also

suggest that substrate heat capacity have less effect on the signal particularly for high absorbance aerosols.

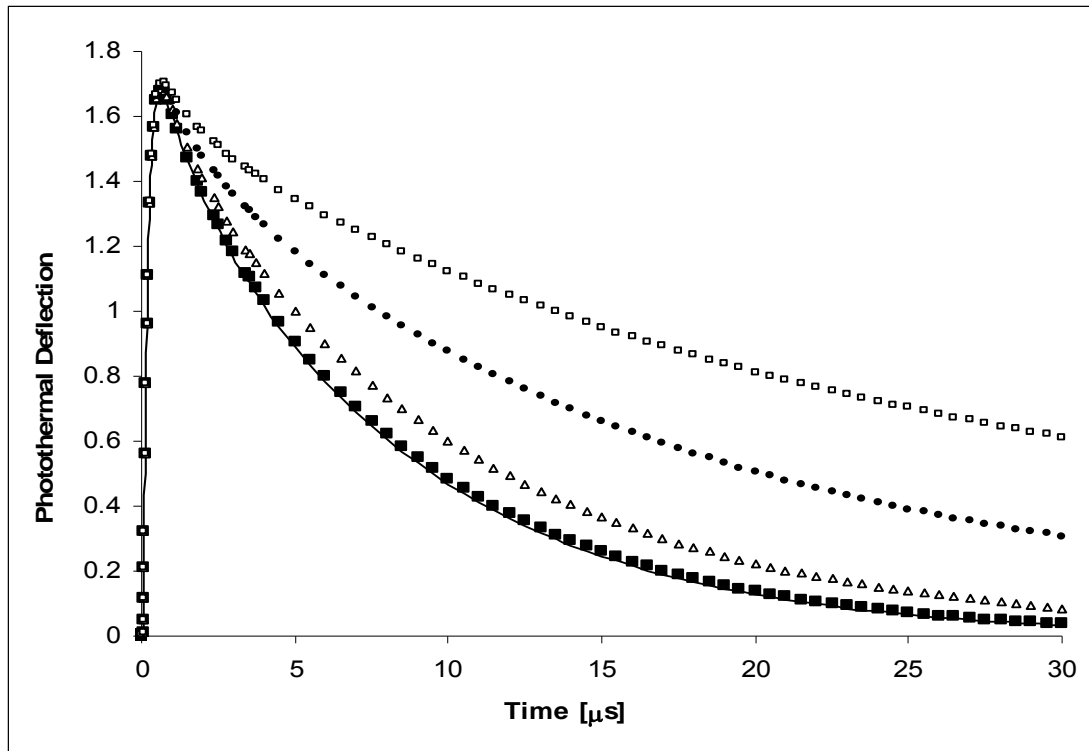


Figure 3-19. Plot of time-dependent photothermal deflection signal showing how substrate's thermal properties influence photothermal signal for different substrate's thermal conductivity relative to thermal conductivity of air with low absorbing aerosol; \square 1, \bullet 10, Δ 100, \blacksquare 1000, $-$ 10000 ($k_p = 1.8$ $\text{W m}^{-1} \text{K}^{-1}$, $C_{pp} = 1740 \text{ J kg}^{-1} \text{K}^{-1}$, $\rho_p = 1720 \text{ kg m}^{-3}$, $C_{ps} = 320 \text{ J kg}^{-1} \text{K}^{-1}$, and $C_{pa} = 1010 \text{ J kg}^{-1} \text{K}^{-1}$, $k_a = 0.0261 \text{ W m}^{-1} \text{K}^{-1}$, $\rho_s = 5330 \text{ kg m}^{-3}$, k_s is varied relative to k_a where subscripts p , s , and a stand for particle, substrate, and air. Irradiance, $E = 3000 \text{ W m}^{-2}$).

Multiple Particle Deposit. For experimental purpose, the sampling method in this type of aerosol analysis may produce aggregates of aerosols on the substrate. This may have considerable effect on the photothermal signal because of non-uniform morphology and surface texture. The question is 1.) How does the non-uniform surface texture from ensembles of aerosols influence the temperature change profile in the surrounding fluid? 2.) Does inter-particle heat transfer affect signal and how do we quantify aerosols? To address these questions the experiments are modeled as a function of particle's arrangement on a surface.

The effects of non-uniform morphology and surface texture on temperature change are examined by comparing model results from ensembles of spherical aerosols of equal size with results from ensembles of aerosols with different sizes and shapes (Figure 3-20).

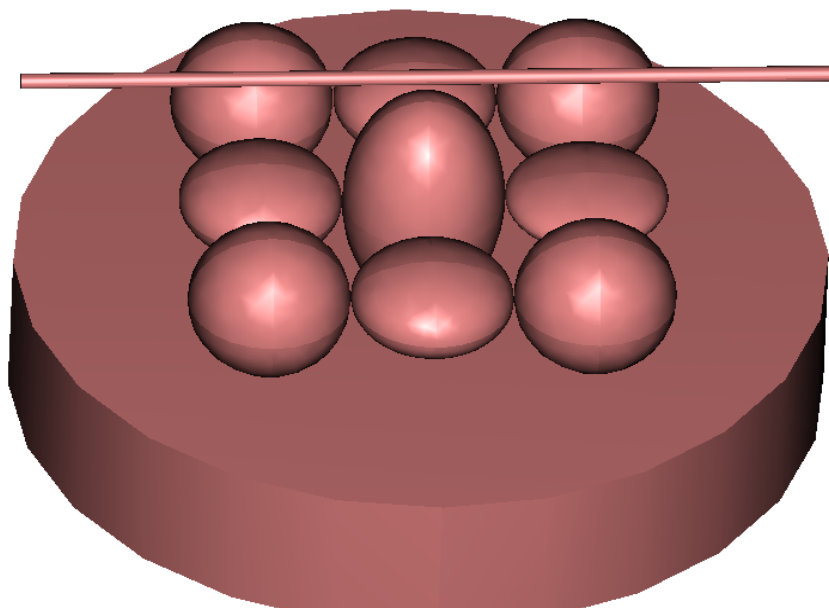


Figure 3-20. Three dimensional geometry of non-uniform aerosols deposited on flat substrate and the probe beam propagation.

Without considering the magnitude, the difference in the temperature profile is insignificant for both models as shown in Figure 3-21. Provided the particle-to-particle separation distance is less than the thermal diffusion length of each particle, the thermal wave overlap from each aerosol compensates the spatial temperature fluctuations that may arise from non-uniform morphology and surface texture.

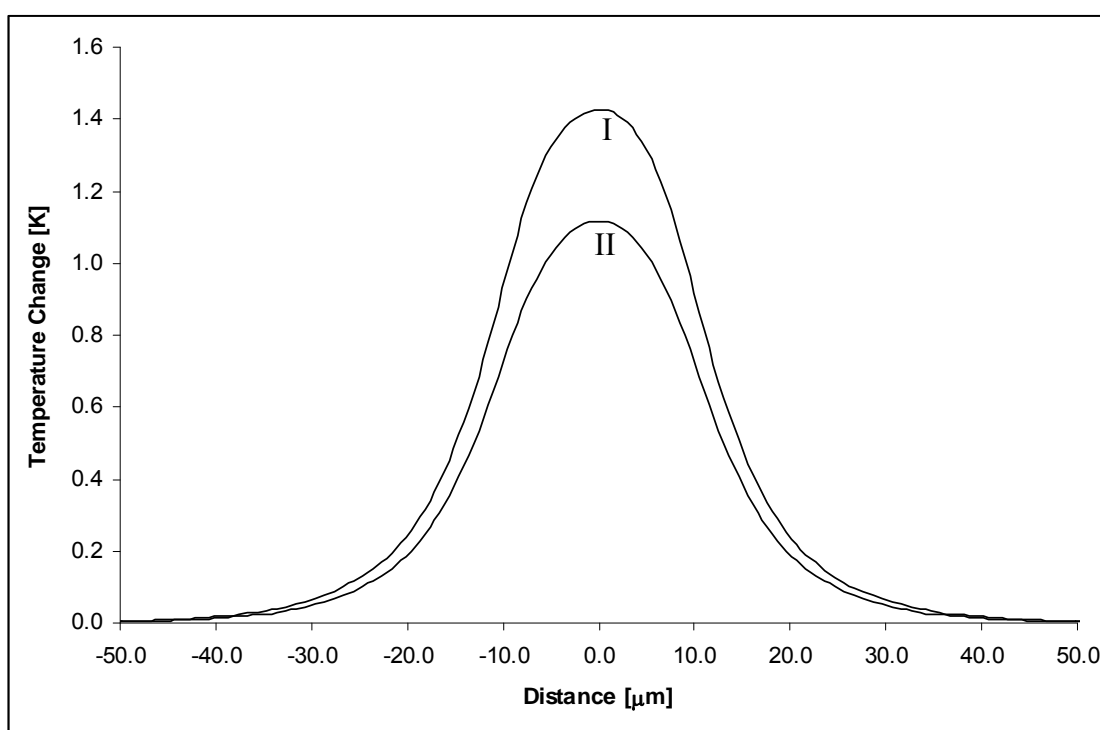


Figure 3-21. Spatial temperature change profile showing the effects of surface texture on temperature gradient above aerosol for: I. uniform aerosols (all aerosols equal in size and shape, II. non-uniform aerosols. *prolate* ($z = 1.5625 \mu\text{m}$, $a = b = 0.8 \mu\text{m}$ in Eq. 2), *spherical* ($z = a = b = 1 \mu\text{m}$ in Eq. 2), and *oblate* ($z = 0.4096 \mu\text{m}$, $a = b = 1.5625 \mu\text{m}$ in Eq. 2) with equal absorbance of 2676 m^{-1} .

The decrease in photothermal signal with non-uniform aerosols, as shown in Figure 3-22, is due to presence of oblate-like aerosols ($z = 0.4096 \mu\text{m}$, $a = b = 1.5625 \mu\text{m}$ in Eq. 2).

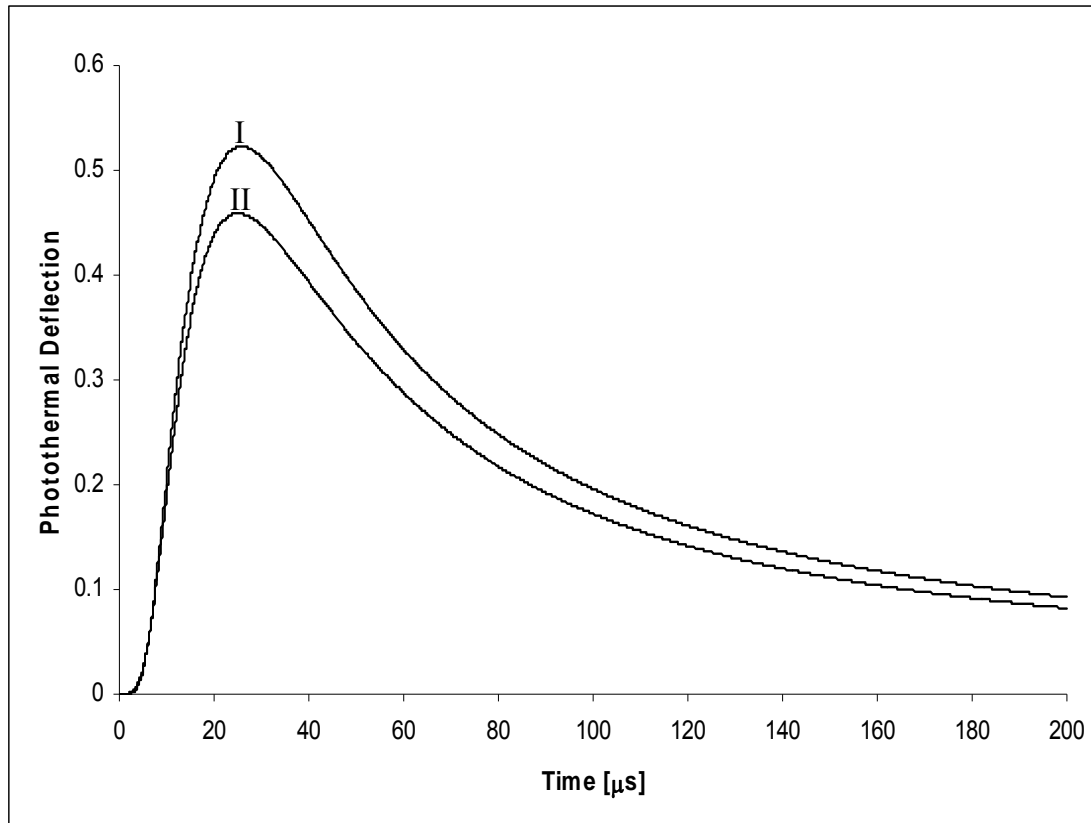


Figure 3-22. Time-dependent photothermal signal for: I. uniform aerosols (all aerosols equal in size and shape, II. for non-uniform aerosols . *prolate* ($z = 1.5625 \mu\text{m}$, $a = b = 0.8 \mu\text{m}$ in Eq. 2), *spherical* ($z = a = b = 1 \mu\text{m}$ in Eq. 2), and *oblate* ($z = 0.4096 \mu\text{m}$, $a = b = 1.5625 \mu\text{m}$ in Eq. 2) with equal absorbance of 2676 m^{-1} .

Model for ammonium nitrate aerosol on germanium substrate is used to examine how the inter-particle heat transfer influences photothermal deflection. The model uses three spherical aerosols arrayed along x -axis with varying aerosol-to-aerosol distance. This also simulates effects of surface particle density in monolayer aerosol deposit. The aerosols have equal diameter of $2\ \mu\text{m}$ and are simultaneously heated with constant irradiance source. Figure 3-23 shows that the theoretical photothermal deflection signal for both high absorbance and low absorbance aerosols approaches linear addition of signal from individual aerosol as the inter-particle distance tends to about $4\ \mu\text{m}$.

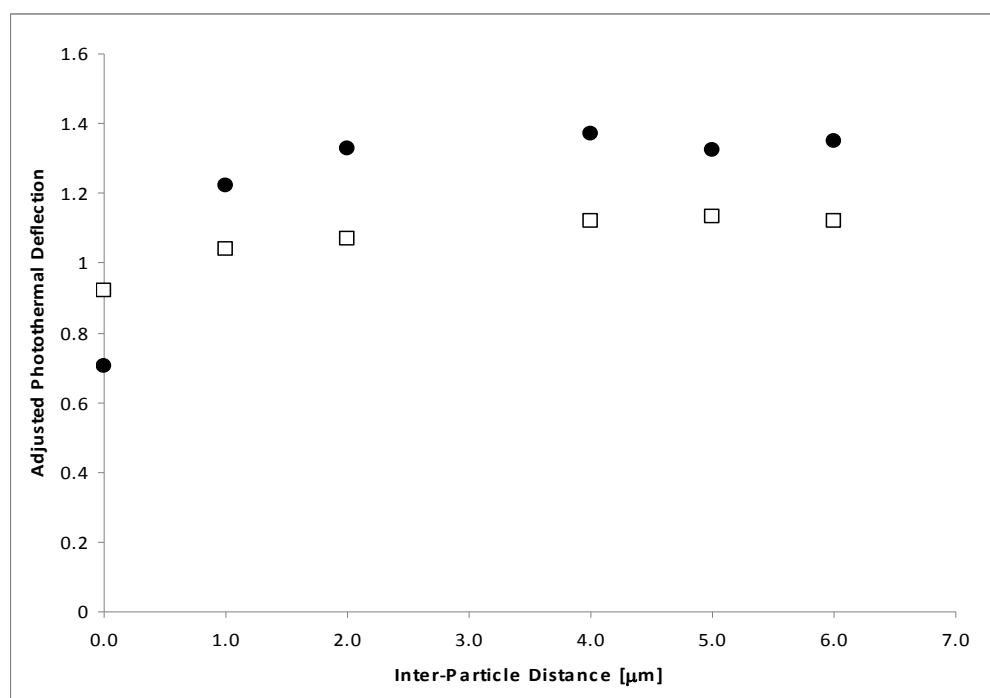


Figure 3-23. Time-dependent photothermal deflection signals showing the effects of inter-particle contact on signal, \square for low absorbance aerosol model, \bullet for high absorbance aerosol model.

The reduced signal magnitude in smaller spaced aerosols suggests that particle-to-particle thermal interactions affect signal. With this condition, quantitative aerosol analysis will require calibration using aerosol standards. For particles in contact with each other, despite the particle-to-particle heat transfer, Figure 3-24 shows that the resulting signal from constant irradiance model linearly increases with number of particles.

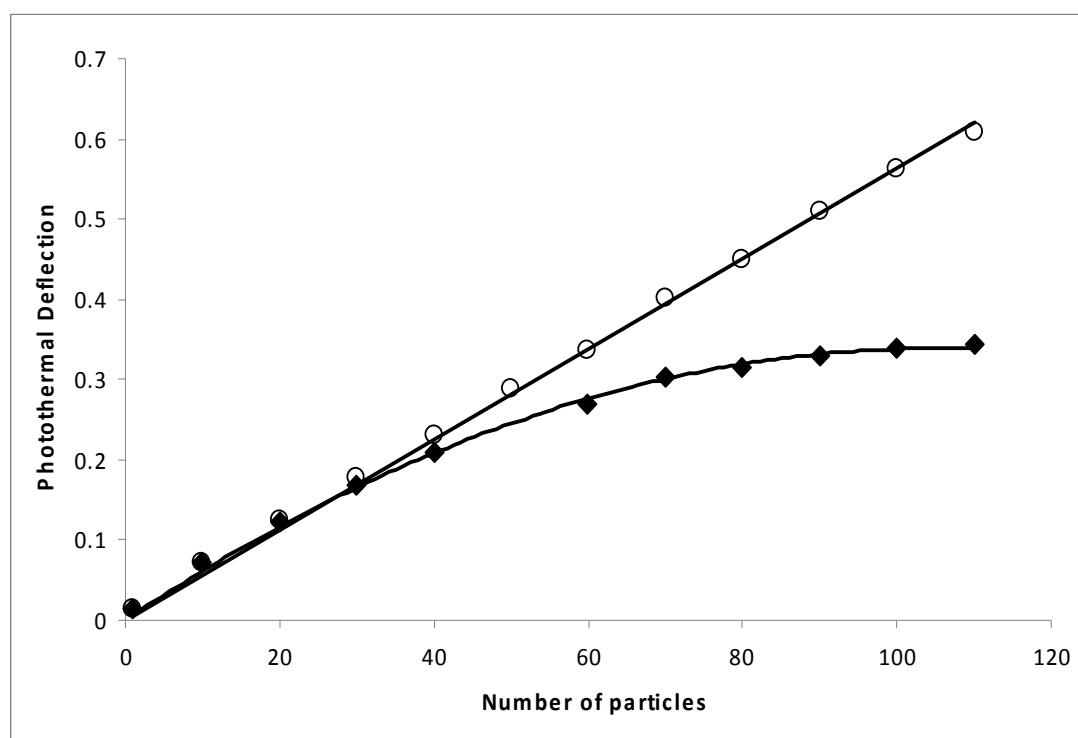


Figure 3-24. Plot of theoretical photothermal signal with number of aerosols with constant irradiance source and gaussian irradiance source (assuming gaussian laser beam radius of 100 μm) for ammonium nitrate aerosols on germanium substrate; \blacklozenge — gaussian irradiance, \circ — constant irradiance.

Assuming the aerosols are heated by a pulse laser with a TEM₀₀ irradiance profile and Eq. 3-2 is rewritten as

$$Q(r) = \alpha E e^{-2r^2/w^2} e^{(-\alpha l)} \cdot f(t) \quad (3-9)$$

where w (m) = 1.0×10^{-4} m is the excitation beam radius, $r^2 = x^2 + y^2$. Other variables have the same definition as in Eq. 3-2. As expected, the signal for gaussian irradiance increases nonlinearly with number of particles, indicating the signal dependence on excitation beam width. This dependence can be reduced by using irradiance source with excitation-beam projected area much larger than the sample's surface area.

With ensembles of particles, the probe laser direction may also affect the observed photothermal signal. Figure 3-25 shows the geometry for three 2 μ m aerosols model used to examine the effects of probe laser direction on the photothermal deflection magnitude.

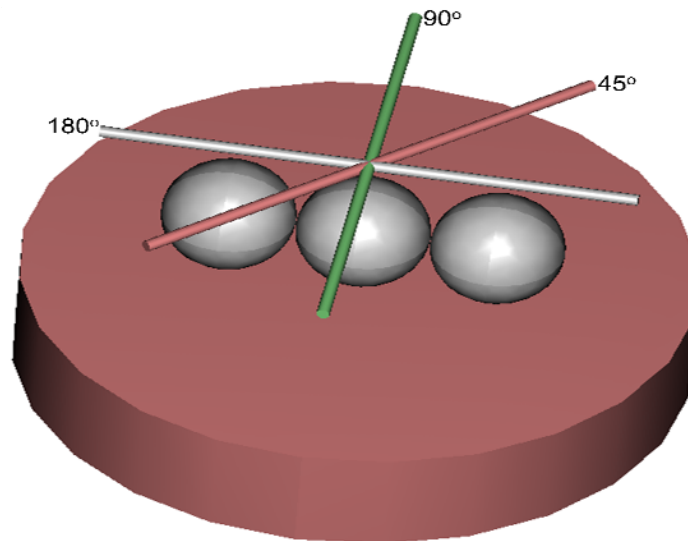


Figure 3-25. Three dimension geometry for three-2 μ m aerosol with different probe beam propagation direction.

The model is performed by probing the temperature gradient in various directions with respect to x -axis. The result (Figure 3-26) shows higher signal with probe laser direction parallel to the x -axis than any other direction. This suggests that the farther the particle from probe laser radial distance the less its effect on the probe beam deflection.

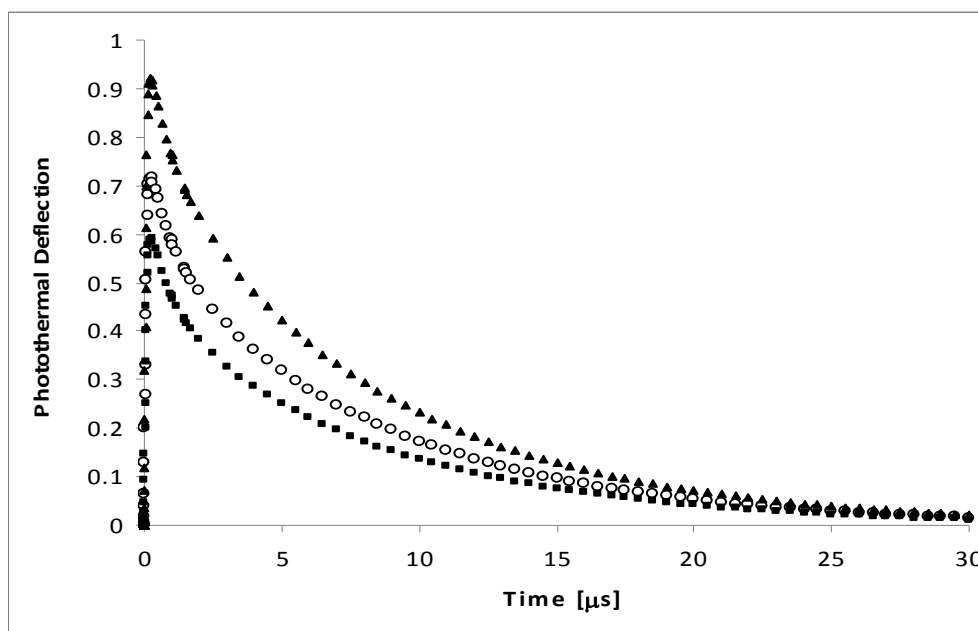


Figure 3-26. Effect of probe beam direction on photothermal signal for ammonium nitrate aerosols on germanium plate; ▲ 180° to x -axis, ○ 45° to x -axis, ◆ 90° to x -axis.

Chopped Continuous Wave Excitation. Contrary to pulse excitation, the aerosol is heated for a longer time scale in the case of continuous wave (CW) excitation. At initial stage, the absorbed energy heats up the aerosol rapidly; however, the air is not heated at a significant rate because of its low thermal conductivity. At later time, when

the aerosol has almost reached saturation temperature, most of the absorbed energy then goes to the air. The most interested aspect of CW excitation models is investigating how the signal changes with particle and substrate thermal properties. A single spherical aerosol with 2 μm diameter is used in all the CW models.

The results showed that the signal profiles for low and high absorbance have the same trend, indicating similar heat transport mechanism for both samples. Figure 3-27 show the time-dependent signal for different ratio of particles heat capacity to that of air and no significant difference is seen in signal magnitude for low and high absorbance particles. However, the signal time constant increases with aerosol's thermal conductivity. The signal however decreases in magnitude with aerosol's thermal conductivity with no change in signal time constant (Figure 3-28). Similar results are obtained for substrate's properties (Figure 3-29 and Figure 3-30). No significant change in signal magnitude and time constant with substrate's heat capacity. But the signal thus decreases with substrate's thermal conductivity.

In summary, signals are relatively stable with CW excitation because at later time of heating the particle becomes like a heat source in the media. This does not mean better results when compared with pulse excitation. Signal magnitude for pulse excitation is about five orders of magnitude larger than CW signals. In laboratory experiment, the signal-to-noise ratio in CW may be ruined by convectional flow as the heating time increases.

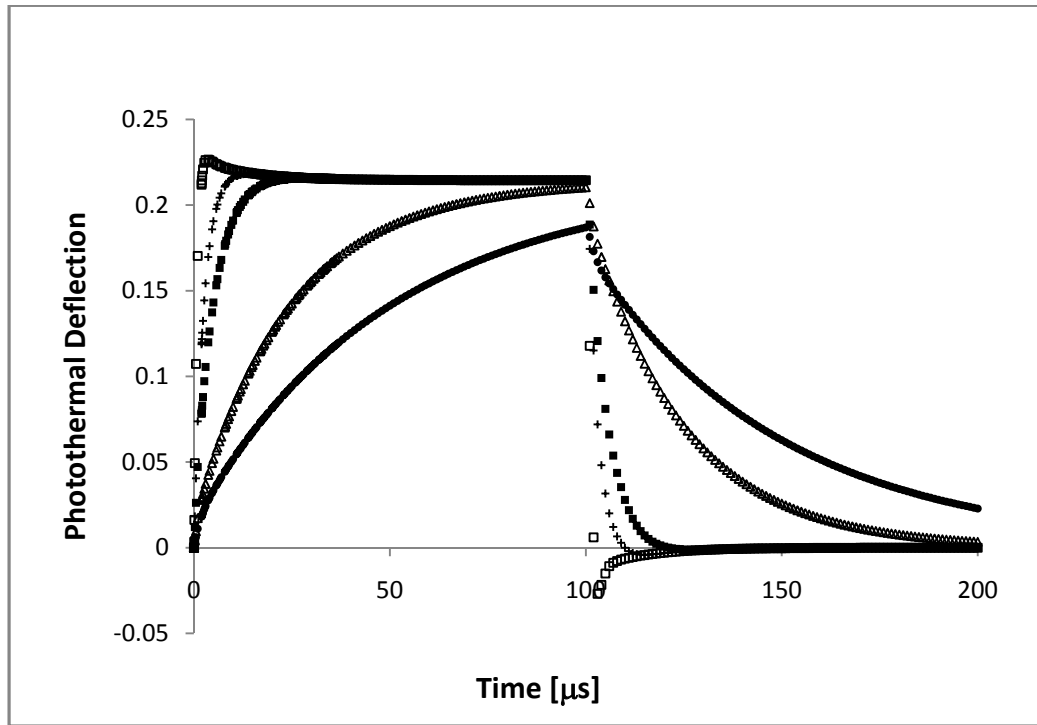


Figure 3-27. Time-dependent photothermal deflection signal with CW excitation showing the effects of aerosols heat capacity for different ratio of heat capacity to heat capacity of air. \square 0.1, $+$ 0.5, \blacksquare 1, \triangle 5, \bullet 10. No difference in the profile for low and high absorbance aerosols except for their magnitude ($k_s = 59.8 \text{ W m}^{-1}\text{K}^{-1}$, $C_{ps} = 320 \text{ J kg}^{-1} \text{ K}^{-1}$, $\rho_s = 5330 \text{ kg m}^{-3}$, $k_p = 1.8 \text{ W m}^{-1} \text{ K}^{-1}$, $\rho_p = 1720 \text{ kg m}^{-3}$, $k_a = 0.0261 \text{ W m}^{-1} \text{ K}^{-1}$, $C_{pa} = 1010 \text{ J kg}^{-1} \text{ K}^{-1}$, and C_{pp} is varied relative to C_a . where subscripts p , s , and a stand for particle, substrate, and air. Irradiance, $E = 3000 \text{ W m}^{-2}$).

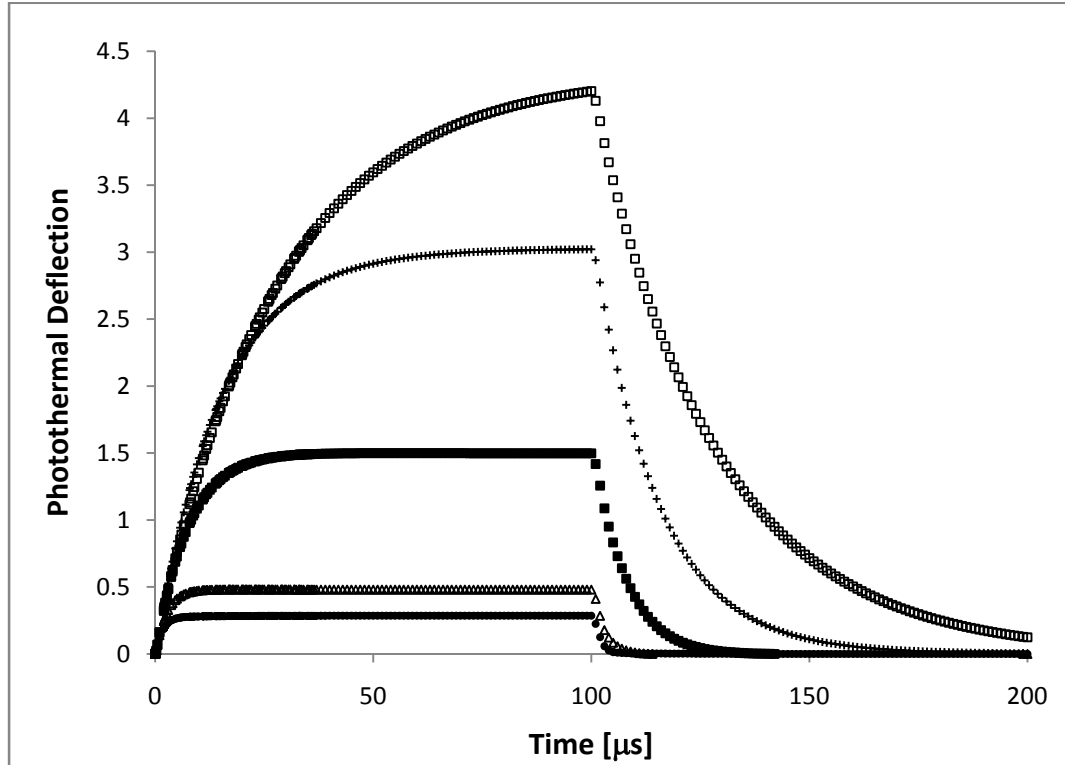


Figure 3-28. Time-dependent photothermal deflection signal with CW excitation showing the effects of aerosols thermal conductivity for different ratio of aerosol's thermal conductivity to thermal conductivity of air. \square 1, $+$ 10, \blacksquare 100, Δ 1000, \bullet 10000. No difference in the profile for low and high absorbance aerosols except for their magnitude. ($k_s = 59.8 \text{ W m}^{-1}\text{K}^{-1}$, $C_{ps} = 320 \text{ J kg}^{-1} \text{ K}^{-1}$, $\rho_s = 5330 \text{ kg m}^{-3}$, $C_{pp} = 1740 \text{ J kg}^{-1} \text{ K}^{-1}$, $\rho_p = 1720 \text{ kg m}^{-3}$, $k_a = 0.0261 \text{ W m}^{-1} \text{ K}^{-1}$, $C_{pa} = 1010 \text{ J kg}^{-1} \text{ K}^{-1}$, and k_p is varied relative to k_a . where subscripts p , s , and a stand for particle, substrate, and air. Irradiance, $E = 3000 \text{ W m}^{-2}$)

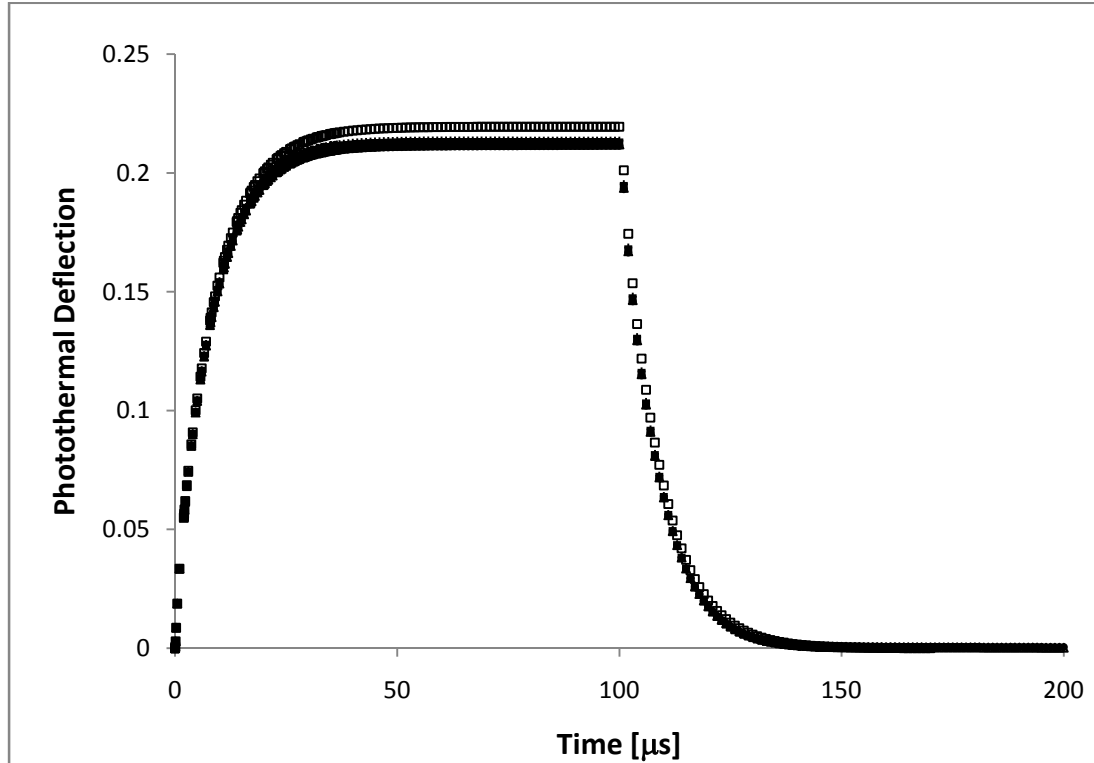


Figure 3-29. Time-dependent photothermal deflection signal with CW excitation showing the effects of substrate's heat capacity for different ratio of substrate's heat capacity to heat capacity of air. \square 0.1, $+$ 0.5, \blacksquare 1, Δ 5, \bullet 10. No difference in the profile for low and high absorbance aerosols except for their magnitude ($k_p = 1.8 \text{ W m}^{-1} \text{ K}^{-1}$, $C_{pp} = 1740 \text{ J kg}^{-1} \text{ K}^{-1}$, $\rho_p = 1720 \text{ kg m}^{-3}$, $k_s = 59.8 \text{ W m}^{-1} \text{ K}^{-1}$, $\rho_s = 5330 \text{ kg m}^{-3}$, $k_a = 0.0261 \text{ W m}^{-1} \text{ K}^{-1}$, $C_{pa} = 1010 \text{ J kg}^{-1} \text{ K}^{-1}$, and C_{ps} is varied relative to C_{pa} . where subscripts p , s , and a stand for particle, substrate, and air. Irradiance, $E = 3000 \text{ W m}^{-2}$).

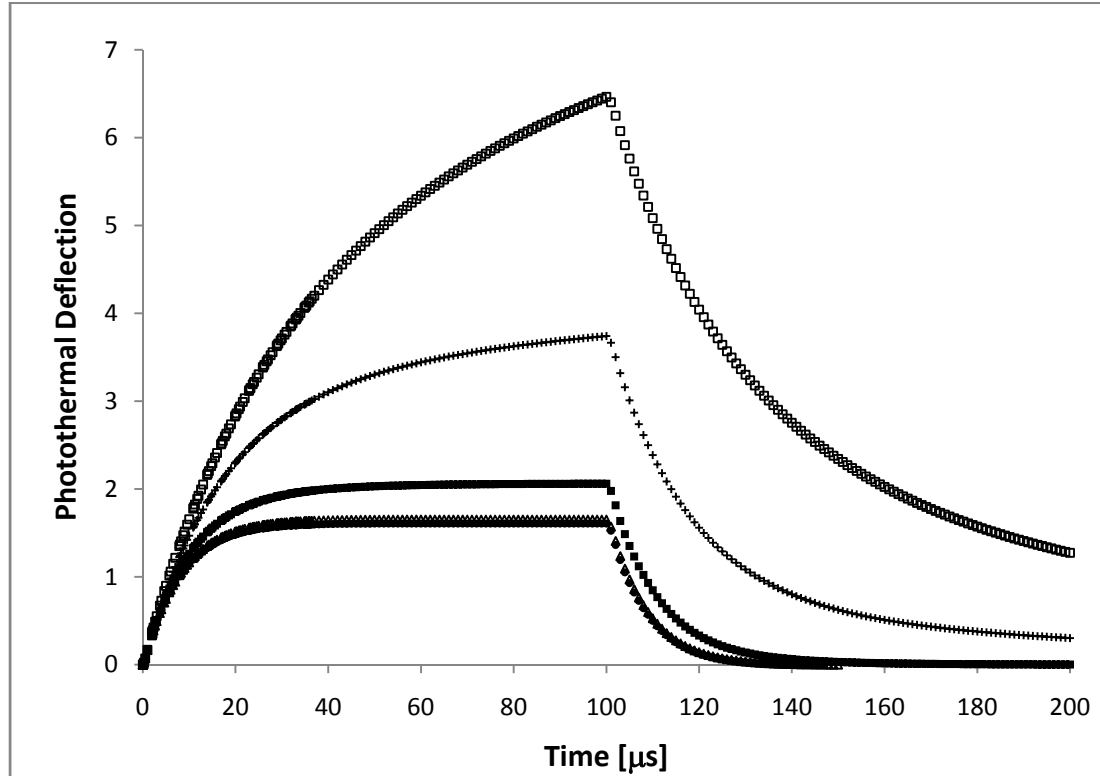


Figure 3-30. Time-dependent photothermal deflection signal with CW excitation showing the effects of substrate thermal conductivity for different ratio of thermal conductivity to thermal conductivity of air. \square 1, $+$ 10, \blacksquare 100, Δ 1000, \bullet 10000. No difference in the profile for low and high absorbance aerosols except for their magnitude ($k_p = 1.8 \text{ W m}^{-1} \text{ K}^{-1}$, $C_{pp} = 1740 \text{ J kg}^{-1} \text{ K}^{-1}$, $\rho_p = 1720 \text{ kg m}^{-3}$, $C_{ps} = 320 \text{ J kg}^{-1} \text{ K}^{-1}$, and $C_{pas} = 1010 \text{ J kg}^{-1} \text{ K}^{-1}$, $k_a = 0.0261 \text{ W m}^{-1} \text{ K}^{-1}$, $\rho_s = 5330 \text{ kg m}^{-3}$, k_s is varied relative to k_a where subscripts p , s , and a stand for particle, substrate, and air. Irradiance, $E = 3000 \text{ W m}^{-2}$).

CONCLUSION

The models presented in this chapter showed that large changes occur in photothermal signal with aerosol properties. The signals appear to be stable with substrate properties particularly with high absorbance aerosols. Changes in photothermal signal with interparticle distance suggest that interparticle heat transfer affect signal from aerosols, hence the need for calibration with aerosol standards for experimental measurement. There is need to know how large is this effect with high surface particle loading.

REFERENCES

- 1 S. E. Bialkowski, *Photothermal Spectroscopy Methods for Chemical Analysis*, John Wiley and Sons, New York, 1996.
- 2 P. H. McMurry, *Atmospheric Environment* **34**, 1959-1999 (2000).
- 3 C. A. Pope, M. J. Thun, M. M. Mamboodiri, D. W. Dockery, J. S. Evans, F. E. Speizer, and C. W. Heath Jr., *American Journal of Respiratory and Critical Care Medicine* **151**, 669-674 (1995).
- 4 L. C. Aamodt, and J. C. Murphy, *Journal of Applied. Physics* **52**, (8), 4903-4914 (1981).
- 5 L. C. Aamodt, and J. C. Murphy, *Journal of Applied Physics* **54**, (2), 581-591 (1983).
- 6 D. Fournier, and A. C. Boccara, *Photothermal Investigations in Solids and Fluids*. Academic Press, New York, 1989.

- 7 J. C. Murphy, and L. C. Aamodt, *Journal of Applied Physics* **51**, (9), 4580-4588 (1980).
- 8 M. A. Schweitzer, and J. F. Power, *Applied Spectroscopy* **48**, (9), 1054-1075 (1994).
- 9 M. A. Schweitzer, and J. F. Power, *Applied Spectroscopy* **48**, (9), 1076-1087 (1994).
- 10 M. A. Shannon, A. A. Rostami, and R. E. Russo, *Journal of Applied Physics* **71**, (1), 53-63 (1992).
- 11 H. S. Carslaw, and J. C. Jaeger, *Conduction of Heat in Solids, 2nd ed.* Oxford, Clarendon, 1986.
- 12 D. Bicanic, S. Kruger, P. Tores, B. Bein, and F. Harren, *Applied Spectroscopy* **43**, (1), 148-153 (1989).
- 13 E. L. Lasalle, F. Lepoutre, and J. P. Roger, *Journal of Applied Physics* **64**,1-5 (1988).
- 14 A. Mandelis, and R. F. Power, *Applied Optics* **27**, (16), 3397-3407 (1988).
- 15 J. F. Power, and A. Mandelis, *Applied Optics* **27**, (16), 3408-3417 (1988).
- 16 J. A. Sell, *Photothermal Investigation of Solids and Fluids*. Academic Press, New York, 1989.
- 17 M. J. Smith, and R. A. Palmer, *Applied Spectroscopy* **41**, (7), 1106-1113 (1987).
- 18 C. H. Chan, *Applied Physics Letters* **26**, (11), 628-630 (1975).
- 19 C. L. DeForest, J. Qian, and R. E. Miller, *Applied Optics* **41**, (27), 5804-5813 (2002).

- 20 H. S. Kwok, T. M. Rossi, W. S. Lau, and D. T. Shaw, *Optics Letters* **13**, (3), 192-194 (1988).
- 21 G. Sageev, and J. H. Seinfeld, *Applied Optics* **23**, (23), 4368-4374 (1984).
- 22 C. F. Bohren, and D. R. Huffman, *Absorption and Scattering of Light by Small Particles*. John Wiley and Sons, New York, 1983.
- 23 CRC Handbook of Chemistry and Physics, 87th ed., 2006-2007.
- 24 E. Jona, T. Sramko, and D. Nagy *J. Thermal Analysis* **27**, 37-42 (1983).
- 25 M. B. S. Osman, A. Z. Dakroury, M. T. Dessouky, M. A. Kenawy, and A. A. El-Sharkawy, *Journal of Thermal Analysis* **46**, 1697-1703 (1996).
- 26 S. S. Kumar, P. M. Abilash, and K. Ramamurthi, *Heat and Mass Transfer* **40**, 679-688 (2004).

CHAPTER 4

AEROSOL GENERATION AND SAMPLING

ABSTRACT

In this chapter, an aerosol generation and sampling apparatus is developed with the major purpose of producing standard aerosols. The apparatus includes 70 L cylindrical flow-tube that is used mainly for dilution and equilibration. The generated aerosols range in size from 0.05 μm to greater 1 μm . Characterization of the generated aerosols in terms of size and concentration is done with Micro-Orifice Uniform Deposit Impactor (MOUDI). The impactor is equipped with a rotator that allows rotating impaction plates. Two types of deposit pattern are generated by operating the impactor in rotating and non-rotating mode. Chemical composition of the particles is examined with Confocal Raman Microscopy.

INTRODUCTION

Calibration of aerosols instruments is essential for high-quality analysis. Up till now, aerosol-measuring instrument calibration has proven to be a difficult task for many reasons. The purpose of calibration is to establish the relationship between the instrument response and a specific aerosol property such as size, mass concentration, number concentration, and chemical composition. The criteria for reliable aerosol generation equipment include: 1) static air sampling; 2) stable aerosol concentration over long time period; and 3) reproducible size of generated aerosols.¹ The apparatus described in this chapter is meant to meet these requirements for the purpose of the intended

measurement. The ability to collect and separate aerosols with respect to their size is another very important aspect of air quality analysis. Cascade impactors, which are arrangement of impactors in series, have performed well in this respect since it was first reported by May, 1945.² The single impactors are called stages and are arranged in such way that the largest particles are separated first and the smallest last. With descending particle size the nozzle diameter and distance between nozzle and impaction plate becomes smaller, gradually decreasing the particle size collected.

Details about theories of cascade impactor has been previously reported in literature.³⁻⁵ Operation of cascade impactor is governed by the principles of inertial impaction. Inertial impaction is a special case of curvilinear motion and used for the collection of particles from air or other gases. The particles are measured by mass and not by volume or surface. Impaction provides besides the mass distribution of particles also the possibility to receive information about chemical composition of particles by subsequent chemical analysis. Figure 4-1 shows a single stage impactor describing the underlying principle governing particle collection by impaction. An aerosol is passed through a nozzle or jet and the output stream is directed against a flat plate, here impaction plate. This flat plate forces the air stream to have an abrupt 90° bend in the streamlines to form what is called curvilinear flow field. For the flow around the plate, small particles are able to follow the curvilinear stream lines almost perfectly due to their very small inertia, whereas large particle with high inertia are too slow to adjust quickly

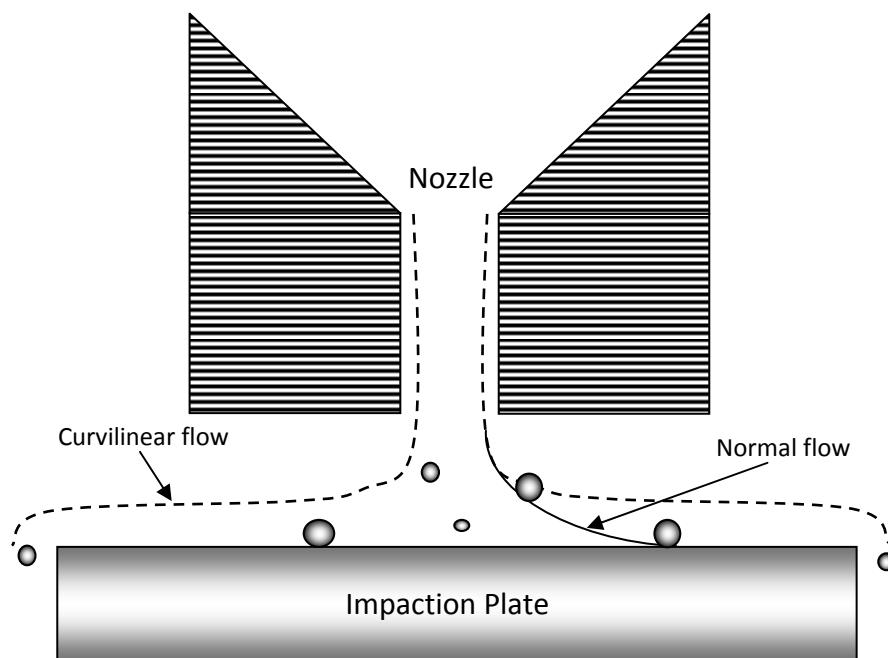


Figure 4-1. Schematic diagram of a single impactation stage.

enough to the new path and continue on their original ones and eventually deposited on the plate. Thus the aerosol is divided into two size categories: particles larger than a certain aerodynamic size are impacted and removed, particles smaller are passing through.

MATERIALS AND METHOD

Aerosol Generation Apparatus. Figure 4-2 shows the apparatus for the production of laboratory-generated aerosols (see Appendix D). The aerosol generation apparatus is setup in manner to Hogrefe *et al.*⁶ There are 4 major components: the nebulizer, the diffusion drier, filtering/thermal conditioning chamber, and impactor. First,

a commercial grade atomizer (BGI collision atomizer model MRE CN24/25) is used for aerosolizing an aqueous solution of ammonium nitrate. The ammonium nitrate solution had a nominal concentration of about 1.5 mg/ml. About 30 mL of ammonium nitrate solution is placed in the atomizer to produce polydisperse aerosols with narrow size distribution.

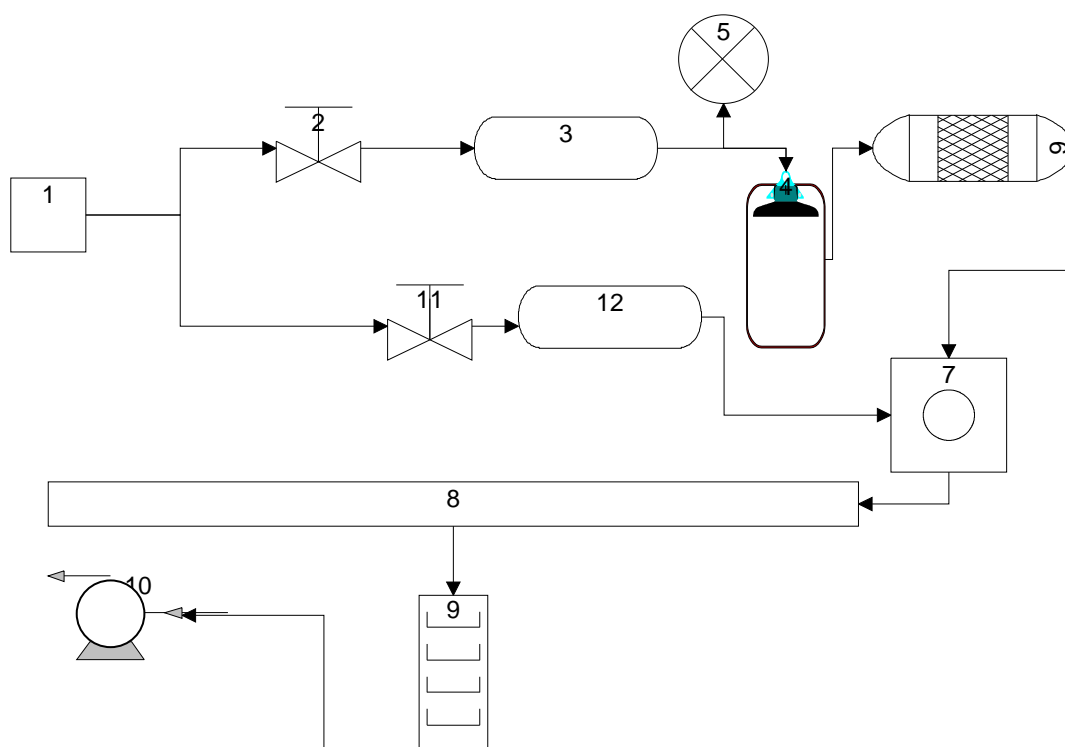


Figure 4-2. Aerosol sampling apparatus: 1. Air source, 2. Valve, 3. Air filter, 4. BGI Collision Atomizer, 5. Pressure Gauge, 6. Drier, 7. 5L-volume mixing chamber, 8. 4 m X 0.15 m Cylindrical slow-Flow tube, 9. 10 stage MOUDI Impactor, 10. Vacuum Pump, 11. Valve, 12. Air filter.

The nebulizing pressure and the output flow rate are constantly monitored throughout the experiment. The nebulizing pressure and output flow rate are 13 psi and 6 L/min, respectively. Fresh portion of the ammonium nitrate stock solution was used for every sampling period in order to minimize evaporation that normally leads to increase in concentration with time, such that the concentration could be held constant within 5% of variation.

Following atomization, the particles are diffusion dried with a homemade diffusion drier filled with desiccated silica gel, bead size 2-4 mm with indicator. The dried aerosols are further diluted by flowing into 60 L/min stream of dry air. The combined streams then flow through a slow-flow chamber (a 4 m long horizontal aluminum tube, 15 cm inner diameter, with an approximate volume of 70 L). The pressure in the chamber is equilibrated with atmospheric pressure by flowing to an open end. Aerosols were sampled through a 2 cm inner diameter sampling port at the mid-length of the slow-flow chamber with an impactor.

Impactor Sampling in Photothermal Spectroscopy. Impactors are used to classify aerosols according to aerodynamic diameter.⁷⁻¹⁰ The aerodynamic diameter as a special case of the equivalent diameter is defined as the diameter of a sphere with unit density (1 g cm^{-3}) and the same settling velocity as the observed particle. A MSP Corporation Model 100 Micro-Orifice Uniform Deposit Impactor is used to collect size resolved aerosols from the slow-flow chamber. This instrument consists of 10 impaction stages, each with a successively smaller cut-off size, which classified aerosols according

to aerodynamic diameter. Nominal cut-off size and number of nozzles of the MOUDI stages are as shown in Table 4-1.

Table 4-1. Nominal cut-off size and number of nozzles of MOUDI stages.

Stage	Cut-off Size (μm)	Number of nozzles
Inlet	15	1
1	10	3
2	5.6	10
3	3.2	10
4	1.8	20
5	1.0	40
6	0.56	80
7	0.32	900
8	0.18	900
9	0.10	2000
10	0.05	2000

Figure 4-3 (B) shows the image of the MOUDI consisting of two basic assemblies. One is the cascade impactor and the other is the rotator. The primary purpose of the rotator is to provide a rotating drive shaft which, in turns, rotates alternate stages of the MOUDI. The rotator also houses a control valve for controlling the flow through the MOUDI and two pressure gages. The upper pressure gage monitors the pressure drop across the upper stages to provide an indication of the flow rate through the impactor. The lower pressure gage monitors the pressure drop across the final stage. The rotating version of MOUDI is meant to produce near uniform particle deposit. However, the deposit pattern is non-homogeneous and makes quantitative analysis of aerosols more complex. The particle deposit for each of the impaction stages consists of non-homogeneous multiple ring patterns.

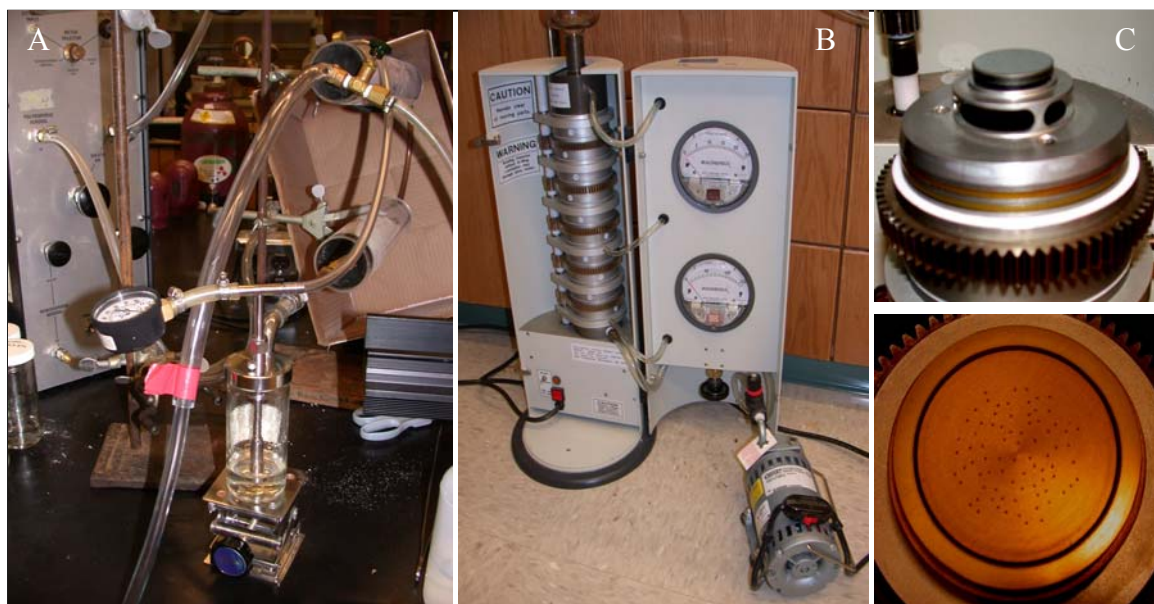


Figure 4-3. Laboratory setup of equipment for generation and collection of ammonium nitrate aerosols. A. Collison atomizer and drier, B. Micro-Orifice Uniform Deposit Impactor (MOUDI), C. MOUDI single stage and impaction plate.

The impactor is first calibrated with polymer microsphere of standard sizes from Duke Scientific Corporation. Two sampling methods are performed by operating MOUDI with rotating and non-rotating impaction plates. The impactor flow rate is 30 L/min at the inlet for both operational modes. A non-coated flat-surface germanium disc, 25.4 mm diameter, is used to collect aerosols of known size at different MOUDI stages for different times. The collected aerosols are transferred in desiccators to the photothermal apparatus in order to prevent aerosols from absorbing air-moisture during transit. Aerosols mass loading is measured with CAHN Model 10931-01F C-31

microbalance. Composition of the collected aerosols is examined with Raman Microscopy.

RESULTS AND DISCUSSION

Rotating and Non-Rotating Impaction. Figure 4-4 and Figure 4-5 show the deposit pattern for non-rotating and rotating impaction plate, respectively. Using rotating impaction plates gives non-homogeneous “multi-ring” deposit pattern that complicates aerosol quantitation with photothermal spectroscopy. Non-rotating impaction method produces individual spots with ensembles of particles, each spot from each nozzle on the impaction stage. A Nikon microscope fitted with Sony Model XC-77RR CCD video camera is used to examine the profile of each spot. The image taken is analyzed with NIH Image J software, and the pixel intensity profile for each spots is obtained as shown in Figure 4-4 (emphasized). The profile for all spots appeared to be similar.

Rotating and non-rotating sampling methods are compared for stage 6 of MOUDI. Using weight by difference, total mass loading for 30 minutes from each collection method is measured with a microbalance. This is performed by using micro glasses as the impaction plate with the assumption that the difference in collection efficiency of micro glasses and germanium is negligible. For 30 L/min MOUDI flow rate, total mass loading of 55 μg and 52 μg are obtained for rotating and non-rotating impaction respectively, resulting in average mass concentration of approximately 50 $\mu\text{g m}^{-3}$.

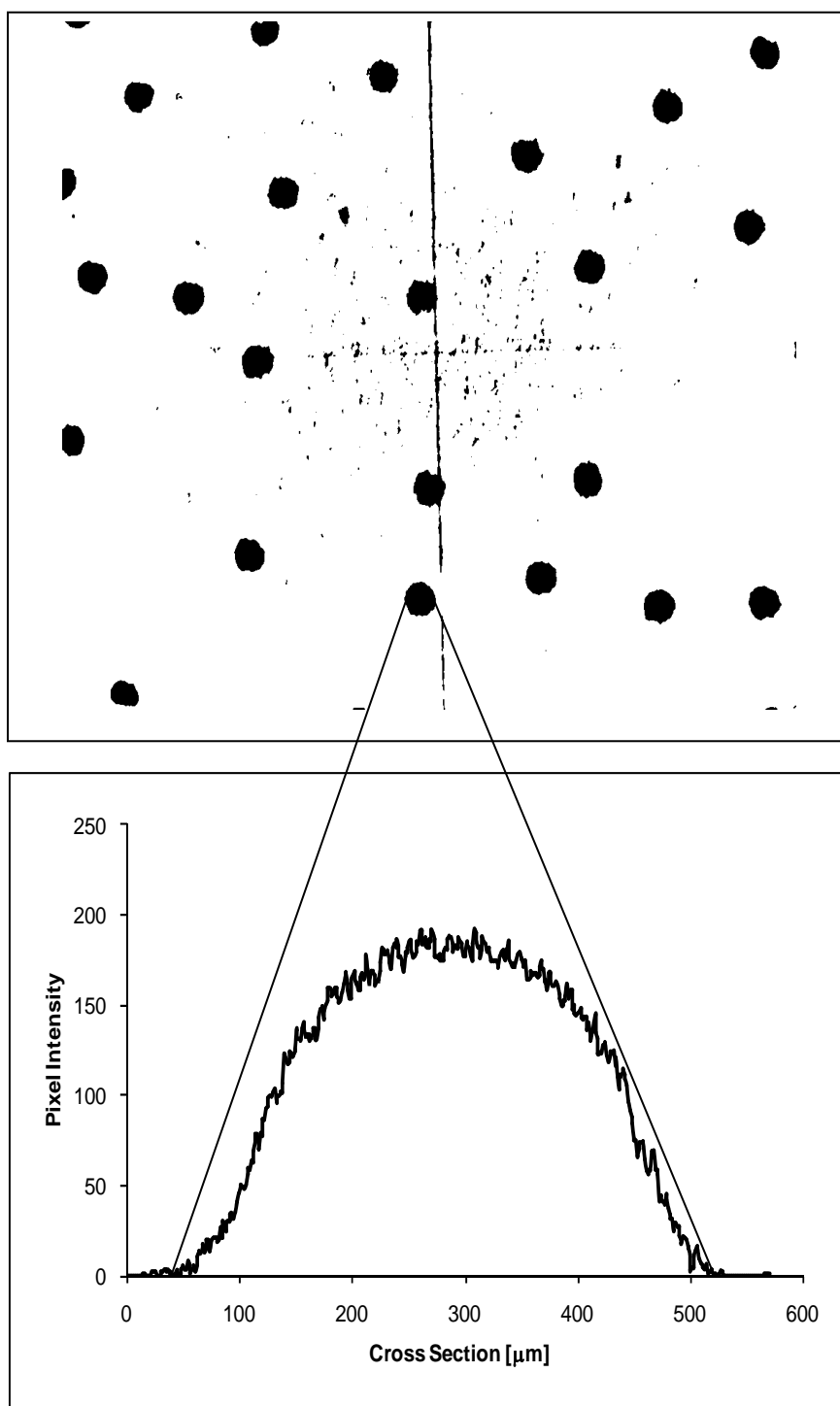


Figure 4-4. Non-rotating impaction deposit collected on stage 6 of MOUDI, and pixel intensity profile of individual spot (emphasized).

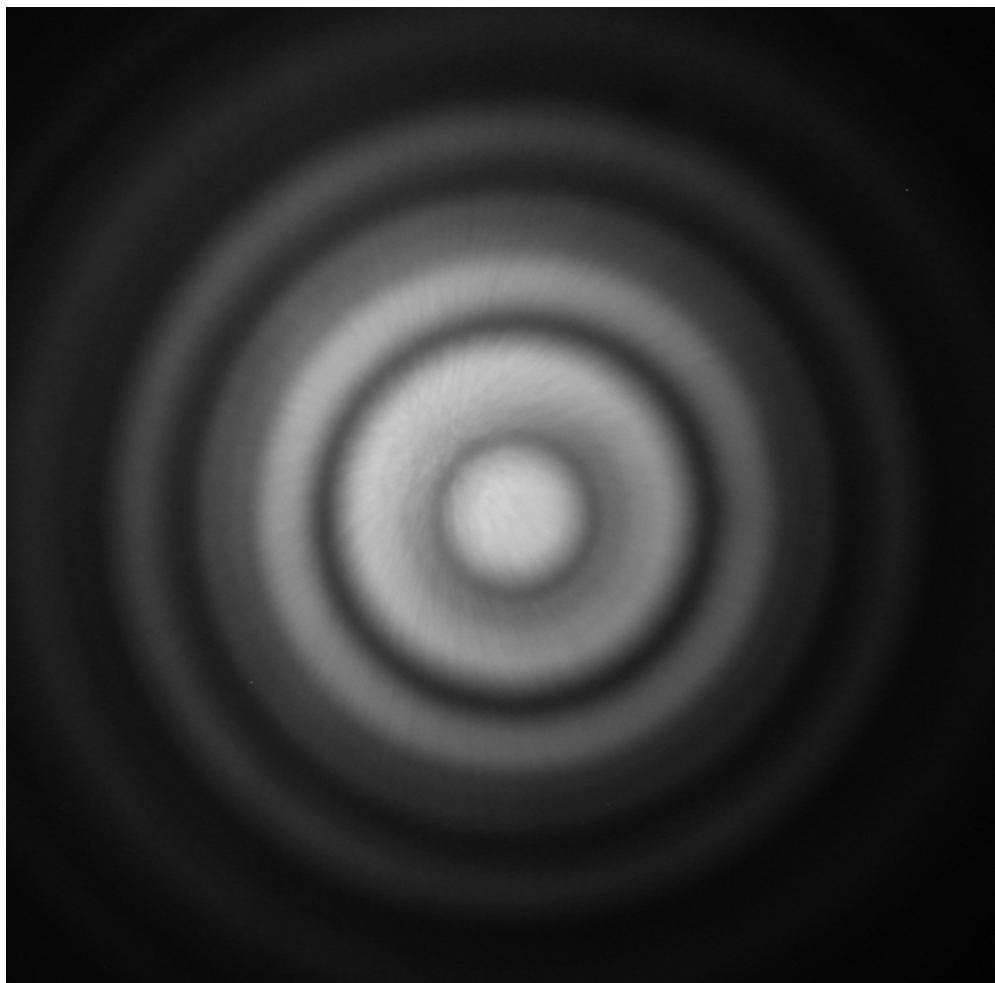


Figure 4-5. Image of rotating impactation deposit collected on stage 6 of MOUDI.

Average mass of individual spot in non-rotating impactation is calculated by dividing the total mass loading by number of spots. On stage 6 (0.56 μm cut-off size) of MOUDI, there are 80 nozzles, hence 80 individual aerosol spot with spot diameter of about 0.55 mm. The spatial distance between two spots is at least 3 mm. The average mass of individual spot is estimated at 0.66 μg . Although, the calculated mass concentration is higher than the current US Ambient Air Quality Standard for $\text{PM}_{2.5}$, the

range is still within the expected linear range for the detection method reported in this dissertation. The difference in total deposit mass for each collection method may be due to adsorption isotherm.

Common practice with impactor sampling is to use substrates made with, aluminum foil, glass microfibres or Teflon as impaction surface.⁷ Chemical analysis and concentration determination of the collected aerosols can then be performed with other analytical techniques. Collection efficiencies for these substrates are well known to be greater than 98%. In spectroscopic method such as photothermal spectroscopy, the choice of collection substrate is important. The substrate must be optically transparent in the wavelength region of the excitation source. Commercial grade germanium window is used as the impaction plate for excitation at 9.56 μm wavelength since it is transparent to the infrared range between 1.8 -17 μm . Particle bouncing is an inherent problem with impactor sampling method, especially with non-coated substrates. This effect reduces the substrate's collection efficiency and increases the measurement uncertainty. Collection efficiency for germanium plate is verified by comparing the mass of collected aerosols with that of aerosols collected with aluminum foil. The estimated efficiency is within 1% variation of the aluminum foil.

Chemical Identification of Aerosols with Confocal Raman Microscopy. The chemical composition of generated aerosols are examined with Raman microscopy. Although it is not possible to produce synthetic aerosols that accurately reflect the qualities of atmospheric aerosols, ambiguity arises when aerosols contain huge moisture content and many chemical components. This part of the measurements was conducted at

the University of Utah in Dr J. M. Harris laboratory. We are able to identify the components of the produced aerosols by using confocal microscopy. Confocal Raman microscopy is a powerful method to provide spatially resolved information about chemical composition of materials in many fields, including study of composites, pigments, semiconductors, and biological structures. It is also a very useful technique for the analysis of small particles attached to the surface of a slide or cover-slip.

Principles of Confocal Raman spectroscopy has been reported elsewhere.¹¹⁻¹³ In a confocal microscope, the light of a laser is focused to a tiny - in the ideal case diffraction limited - spot on the sample with an objective lens. The reflected or backscattered light is collected and re-collimated by the same objective and then separated from the incoming light path by a beam splitter. The aim of this section of our measurement is to chemically identify the generated aerosols that are been analyzed with photothermal spectroscopy.

Confocal Raman Microscope. Figure 4-6 shows the microscope setup image as used for the measurement. A detailed description and block diagram of the microscope optics has been reported.¹¹ Briefly, sample excitation is provided by a Kr⁺ laser (Innova 90, Coherent, Inc.) operating at 647.1 nm with an output power of 30 mW. The laser beam was directed optically through a 4X beam expander (model 50-25-4X-647, Special Optics, Inc.) mounted on a Nikon TE 300 inverted fluorescence microscope. The expanded beam passed through the rear of the microscope into a cube that held a band-pass filter (D647/10, Chroma Tech, Inc.), a dichroic beam splitter (655DCLP, Chroma Tech, Inc.) and a high-pass filter (E660LP, Chroma Tech, Inc.). The beam is reflected by the dichroic beam upward into a 100X, 1.4 NA oil immersion microscope objective (CFL

PLAN APO, Nikon, Inc.) and was focused through a #1-thickness microcover glass (VWR glass), which is the substrate on which the aerosol is sitting on. Raman scattering from the sample was collected by the same objective and passed through the dichroic and high-pass filter into the microscope frame, where it could then be directed to a 10X eyepiece for visual observations, a monochromator (250IS, Chromex, Inc.) and CCD (DV420, Andor, Inc., cooled to $-60\text{ }^{\circ}\text{C}$) for spectral analyses, or a digital camera (CoolPix 950, Nikon, Inc.) for imaging. Whitelight, bright-field illumination of the sample was provided by an overhead 30-W tungsten illuminator.

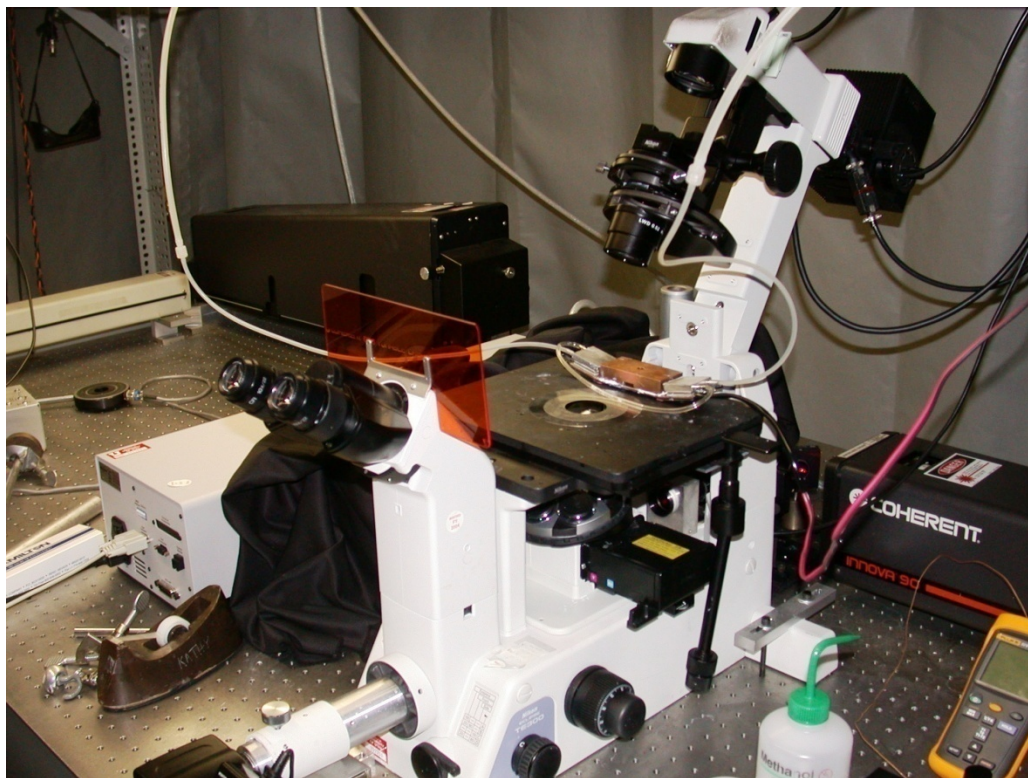


Figure 4-6. Experimental setup for Confocal Raman Microscopy measurement.

The confocal aperture was established in a manner similar to Williams *et al.*¹⁴ by focusing the sample image onto the entrance slit of the monochromator to define a horizontal position and binning three rows of pixels of the CCD image to define a vertical position. The monochromator slit was set at 50 μm to define a 500 nm region in the horizontal plane within the sample (100X magnification) while three rows of the CCD (equivalent to 66 μm) were sampled and binned to define a 660 nm vertical region in the sample.

Results from Raman Measurement. Spatially diffused ammonium nitrate aerosols are generated as described earlier in this chapter. The aerosols are collected on a #1 thickness microcover glass (VWR Scientific glasses) as shown in Figure 4-7.

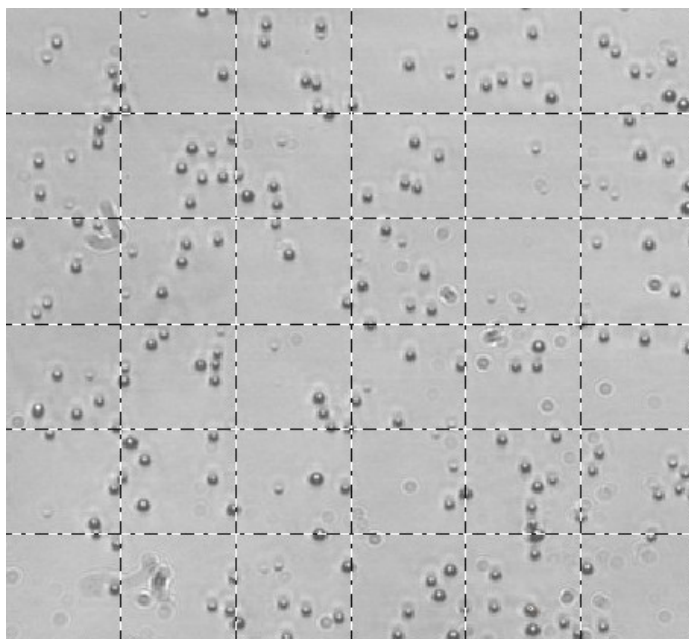


Figure 4-7. Image of spatially diffused ammonium nitrate aerosols collected on #1 thickness microcover glass for Confocal Raman microscopy. Each particle diameter is about 1 μm .

Figure 4-8 shows the Raman Spectrum of a single ammonium nitrate aerosol of about 1 μm aerodynamic diameter collected on micro-slide #1. Ammonium nitrate has three major shifts at 733 cm^{-1} , 1050 cm^{-1} , and 1440 cm^{-1} as shown in the spectrum. The result shows that the generated aerosols are of high purity with less moisture content. This also indicates that this method can be a useful tool for qualitative analysis of ambient aerosols. Simultaneous detection of photothermal signal and Raman shift would be a novel method for aerosols analysis.

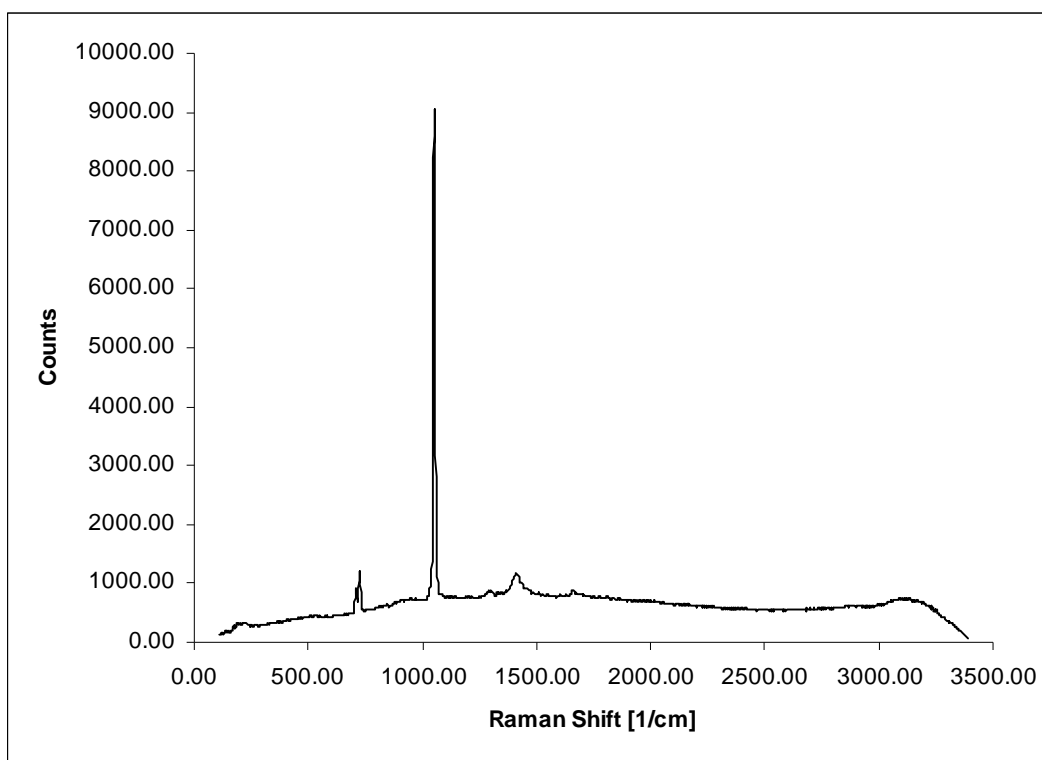


Figure 4-8. Measured Raman shift of single ammonium nitrate aerosol (1 μm aerodynamic diameter) using Convocal Raman Microscopy. Ammonium nitrate particle has major shifts at 726 cm^{-1} , 1050 cm^{-1} , and 1440 cm^{-1} .

CONCLUSION

A method of aerosol generation for spectroscopic analysis based on impactor sampling method is developed. The sampling technique can be used to produce standard aerosols of known chemical composition and size. Aerosols produced have low moisture content with no impurity. Raman Microscopy is used as a qualitative detection method to examine the composition of collected aerosols. This method may be used in future to provide the amount of various components of atmospheric aerosols.

REFERENCES

- 1 Y.-S. Cheng, and B. T. Chen, Aerosol Sampler Operation. In Air Sampling Instruments. ACGIH Worldwide, Cincinnati, OH, 2001; p 177-199.
- 2 K. R. May, *Journal of Scientific Instruments* **22**, 187-195 (1945).
- 3 V. A. Marple, and K. L. Rubow, Theory and design guidelines. In Cascade Impactor Sampling and Data Analysis. American Industrial Hygiene Association: Akron, OH, 1986; p 79-101.
- 4 V. A. Marple, K. L. Rubow, and S. M. Behm, *Aerosol Science and Technology* **14**, 434-446 (1991).
- 5 V. A. Marple, K. L. Rubow, and B. A. Olson, Inertia, Gravitational, Centrifugal, and Thermal Collection Techniques. In *Aerosol Measurement: Principles, Techniques and Applications*. Van Nostrand Reinhold: New York, 1993; p 206-232.

- 6 O. Hogrefe, F. Drewnick, G. G. Lala, J. J. Schwab, *Aerosol Science and Technology* **38**, 196-214 (2004).
- 7 P. H. McMurry, *Atmospheric Environment* **34**, 1959-1999 (2000).
- 8 D. Michaud, P. Picard, and M. Baril, *Aerosol Science and Technology* **31**, 323-337 (1999).
- 9 D. Michaud, P. Picard, and M. Baril, *Aerosol Science and Technology* **31**, 338-349 (1999).
- 10 P. Picard, D. Michaud, and M. Baril, *Aerosol Science and Technology* **31**, 350-357 (1999).
- 11 T. E. Bridges, M. P. Houlne, and J. M. Harris, *Analytical Chemistry* **76**, 576-584 (2004).
- 12 L. Kador, T. Schittkowski, M. Bauer, and Y. Fan, *Applied Optics* **40**, 4965-4970 (2001).
- 13 M. Larsson, J. Lindgren, A. Ljunglöf, and K. Knuutila, *Journal of Chromatography A* **954**, 151-158 (2002).
- 14 K. P. J. Williams, G. D. Pitt, D. N. Batchelder, and B. J. Kip, *Applied Spectroscopy* **48**, (4), 232-235 (1994).

CHAPTER 5

DEVELOPMENT OF INFRARED PHOTOTHERMAL DEFLECTION
SPECTROSCOPY (MIRAGE EFFECT) FOR ANALYSIS OF CONDENSED-PHASE
AEROSOLS COLLECTED IN A MICRO-ORIFICE UNIFORM DEPOSIT IMPACTOR

ABSTRACT

This chapter is focused on potential of mid-infrared photothermal spectroscopy for aerosol analysis. Ammonium nitrate aerosols are deposited on flat substrate by using Micro-Orifice Uniform Deposits Impactor (MOUDI). Photothermal spectroscopy with optical beam deflection (mirage effect) is used to detect deposited aerosols. Photothermal deflection from aerosols is measured with pulsed infrared laser light to heat up aerosols collected on the substrate. The deflection signal is obtained by measuring the position of a spot from a beam of light as it passes near the heated surface. The results showed that non-rotating impaction method is better for MOUDI operation because it produces samples with simple analysis and higher signal compared with rotating impaction method. Energy dependent photothermal measurement shows linear relationship between signal and laser intensity, and no loss of signal with time is observed. Detection limit from signal-mass curve is 7.31 ng. For 30 minutes collection time and 30 L/min. impactor's flow rate, the limit of detection in terms of aerosol mass concentration is $0.65 \mu\text{g m}^{-3}$. The detection limit from signal-number curve is 18 particles for average particle diameter of $3.0 \mu\text{m}$. Aerosol mass concentration calculation from number concentration measurement demonstrates a detection limit of $0.1 \mu\text{g m}^{-3}$ for 30 L/min. flow rate over a collection time of 30 minutes.

INTRODUCTION

Several health problems have been associated with aerosols less than 2.5 μm in diameter.¹ The recently revised National Ambient Air-Quality Standards reduced the 24-hr fine particles standard from 65 $\mu\text{g m}^{-3}$ to 35 $\mu\text{g m}^{-3}$.^{2,3} This standard requires sensitive ambient air monitoring methods with low detection limit in reference to the new standard. Photoacoustic spectroscopy is one of the viable spectroscopic techniques for analyzing atmospheric aerosols.⁴⁻⁸ In photoacoustic, light energy absorbed by the particles heats the surrounding gas. The temperature change in the surrounding gas causes the gas to expand and contract according to the modulation frequency of the light and the associated pressure variation intensity can be measured with a microphone.

Unlike photoacoustic, photothermal spectrometry is a novel optical technique that is used to measure low absorbance by probing the refractive index change created in the sample when absorption of electromagnetic radiation and subsequent thermal relaxation occur. However, photothermal technique tends to be more sensitive than photoacoustic. Photothermal optical beam deflection (mirage effect) probes the heat diffusion within a sample in an indirect way.

Photothermal deflection (mirage effect) is a valuable spectroscopic method for surface and interface analysis with both UV-VIS and NIR-Mid IR wavelength. Like other photothermal techniques, it can be applied to various samples including opaque and non-reflecting materials, which are difficult by using other conventional photothermal methods such as thermal lensing. Furthermore, photothermal deflection detection is

similarly characterized, as is the case with other photothermal methods, by critical dependence of the signal on the thermo-optical properties of the surrounding fluid. Previous reports on photothermal spectroscopy of aerosols have focused on the impact of associated heat and mass transfer processes on the atmosphere.⁹⁻¹² Photothermal deflection has been used to study the thermo-optical properties for various samples,¹³⁻¹⁶ however none has reported its application to aerosol analysis.

This chapter is focused on the development of photothermal deflection apparatus for chemical analysis of aerosols. Instrumentation for aerosols analysis tends to be complex and difficult especially when versatile sampling technique is not at hand. Sampling by impaction is a popular method in the measurement of aerosols.^{8, 17-22} In this chapter photothermal deflection spectrometry of aerosols with impaction sampling method is presented. Aerosol samples collected on germanium plate in MOUDI are analyzed with photothermal deflection apparatus. Photothermal measurements are performed in terms of mass concentration and number concentration. Aerosol mass concentrations are determined by using microbalance mass calibration to scale photothermal signals to mass loading. For number concentration, collected particles are first inspected and counted with optical microscope and the particle counts are used to standardize the photothermal measurement.

Chapter 3 of this dissertation details the report on numerical modeling of photothermal deflection from condensed-phase aerosols collected on plane surface substrate. The results showed that the temperature distribution above aerosol is dependent on shape, size and number of particles. The results also indicate that signal magnitude is

relatively stable with substrate's heat capacity and thermal conductivity especially with high absorbance particles.

THEORY

The theoretical principle of photothermal deflection has been previously reported,^{13-15, 23-33} and details about temperature profile in three-layer samples can be found in literature.^{13-15, 23, 25, 26, 28, 30, 31}

Considering air, aerosol, and substrate layers geometry as shown in Figure 3-1 of Chapter 3, the varying temperature above the surface of aerosol produces a refractive index gradient in the coupling fluid (air).

For small thermal perturbation, the photothermal deflection signal (beam deflection angle) due to the temperature gradient in the air that changes the position of the probe beam along its path, l , is given as

$$\bar{\theta} = \frac{1}{n} \frac{dn}{dT} \int_x^l \nabla_{\perp} \delta T \cdot \hat{c} s \quad (5-1)$$

If the probe beam propagation axis is along the x direction above the aerosol, the probe beam deflection is in two directions, x and z . If the deflection in the z direction is due to the heat diffusion processes perpendicular to the surface and the deflection in the y direction is due to the heat diffusion processes parallel to the surface, the normal deflection angles, θ_n , and the transverse deflection angle, θ_r , are given as

$$\theta_n = \frac{1}{n} \frac{dn}{dT} \int_{-\infty}^{+\infty} \frac{\partial \delta T}{\partial z} dx \quad (5-2)$$

$$\theta_r = \frac{1}{n} \frac{dn}{dT} \int_{-\infty}^{+\infty} \frac{\partial \delta T}{\partial y} dx \quad (5-3)$$

In this measurement it is also assumed that convective and radiative heat transfer are negligible, the sample is thermally and elastically isotropic and in good thermal contact with the fluid and the substrate, the coupling fluid and the backing substrate are optically transparent to the irradiation source, and the contribution from the acoustic wave to the thermal field is negligible.

EXPERIMENTAL

As illustrated in Figure 5-1, the apparatus consists of three major components: the pump laser and associated optics, the probe laser optics and detectors, signal collection and processing electronics. The pump laser is a Tachisto, pulsed, line-tunable CO₂ laser (9-11 μm wavelength range). The output of this laser is a TEM₀₀ mode pulse of 120 ns duration. Using low N₂ partial pressures in the CO₂ laser gas mixture minimized the relative energy in the “tail” portion of the pulse. The pulse laser energy was attenuated by placing a “Venetian blind” style infrared attenuator in the beam path prior to the focusing optics. CO₂ laser wavelengths are determined with an Optical Engineering CO₂ spectrum analyzer, Model 16-A. The R25 line of the 9.56 μm transition was used for all measurements. The pump beam is focused with a 100 mm focal length

off-axis parabolic focusing mirror before the sample. In this case, aberration value often associated with refractive focusing optics is minimized.

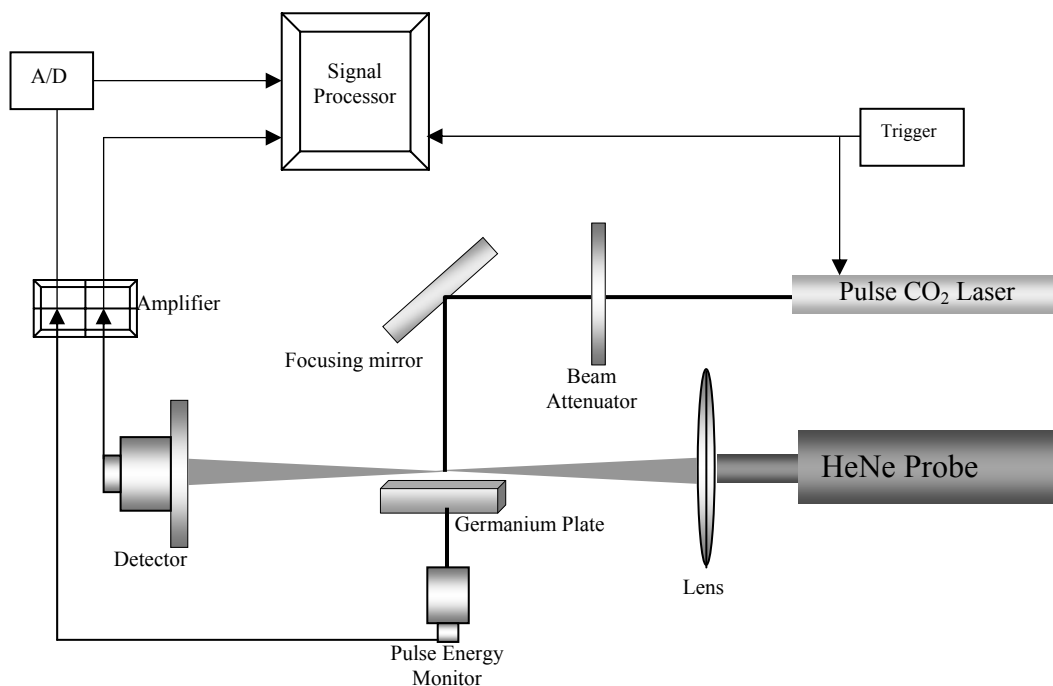


Figure 5-1. Photothermal mirage apparatus: The excitation beam is focused by a 100 mm focal length reflective off axis parabolic mirror. The probe laser, propagating just above the sample's surface in a horizontal axis perpendicular to the pump beam axis, was focused by a 100 mm fused silica lens. The deflection signal is detected by a bi-cell position sensing detector. Excitation pulse energy is simultaneously measured with the deflection signal using RjP-735 pyroelectric energy monitor.

This apparatus adopts small configuration described in Chapter 2 with foot print of about 0.09 m^2 without the CO_2 laser, probe laser, and electronic devices. The beam waist of the CO_2 laser at sample surface position is measured with a razor blade edge on a micrometer driven translation stage. The electric field beam radius at the sample surface calculated from the razor blade excursion resulting in 10% to 90% of the maximum pulse energy is 0.75 mm for mass concentration measurements and $70 \text{ }\mu\text{m}$ for number concentration measurements.

The probe laser, propagating just above the aerosol surface along horizontal axis perpendicular to the pump beam axis, was a polarized 4-mW continuous-wave He-Ne laser (632.8 nm wavelength) Uniphase Model 1205-1. The probe beam was focused by a 100 mm fused silica lens. The probe beam spot size measured with razor blade technique is about $38 \text{ }\mu\text{m}$ with a normal offset, z_0 of about $170 \text{ }\mu\text{m}$ (the distance from sample surface to the center of the probe beam). The probe beam normal offset is kept constant from one sample to another by a simple technique. First, the zero offset position ($z_0 = 0$) is determined by monitoring the sum of the photocurrent as detected by bi-cell position sensing detector with an oscilloscope. The maximum output from the detector indicates that the beam spot at the detector is symmetrical. The sample is moved close enough to the probe beam until a slight shift in the detector output is observed, indicating a contact between the sample surface and the probe beam. The sample is then moved back with a micrometer translator by a distance of $150 \text{ }\mu\text{m}$. This ensures that the probe beam offset is invariant from one sample to another. However, this method requires that the sample surface plane is properly aligned at 180° with the probe beam propagation axis. The

pump and the probe beam intercept each other at probe beam spot position. Photothermal deflection was monitored by using a United Detector Technology Model 301-DIV single axis position-sensing detector. Probe laser beam deflection occurs as a consequence of sample heating by pump laser excitation.

Signals from the detector were amplified and electronically filtered with a Tektronix model AM-502 differential amplifier. The integrated pulsed laser energies were measured with a Laser Precision Model RjP-735 pyroelectric energy monitor and digitized with a 12-bit analog to digital converter (A/D). The integrated pulse energy is directly proportional to the intensity since the laser pulse duration does not change from pulse-to-pulse, and the focus spot size of the pump beam does not change. Data collection and processing were performed on a PC with matched filter smoothing software that was developed in this laboratory.³⁴

Aerosol samples collected on uncoated flat-surface germanium disc were analyzed in the photothermal apparatus. The sample was placed at approximately 15 mm after the CO₂ laser beam spot. The plate was vertically positioned on a three dimensional micrometer driven translation stage with the sample plane perpendicular to the pump beam propagation axis. Horizontal translation perpendicular to the pump beam axis was controlled by using Oriel Corporation Model 18002 motor mike actuator 25 mm range.

RESULTS AND DISCUSSION

Aerosol Mass Concentration Measurements. Measurements of particulate mass concentrations are important for regulatory and scientific reasons. The current US

National Ambient Air Quality Standard for particulate matter applies to mass concentrations smaller than 10 μm aerodynamic diameter, and a new standard for mass concentrations of particles smaller than 2.5 μm aerodynamic diameter has been promulgated.² While research studies tend to focus on speciation and size, it is essential to be able to reconcile measured mass concentrations with the sum of measured species. Therefore, mass concentrations are also routinely measured in aerosol research studies. In this section, the measurement of aerosols mass concentration is considered using a new method based on photothermal deflection spectroscopy.

Rotating and Non-rotating Sampling. The impactor was operated in rotating and non-rotating mode, resulting in two types of aerosol deposit profile. Photothermal deflection signals from aerosols collected with rotating and non-rotating impaction were compared. The aerosols were heated with pulses of the pump beam at 3.75 Hz repetition rate and thermal propagation through the particles into the surrounding air, following relaxation of the absorbed optical energy, causes a change in the refractive index of the air. This then alters the propagation of the probe beam that passes through the air above the sample surface. The signal from blank germanium plate is negligible.

For the rotating impaction deposit, the signal was obtained by scanning the sample in the horizontal direction moving from the center towards the edge of the plate in order to obtain integrated signal over the scanned area. The horizontal scanning distance is relative to the pump-probe beam intercept. The signal for non-rotating impaction deposit was obtained by heating each aerosols spot individually. Chances of probing two

spots at a time are very low since the pump beam size is about six times less than the inter-spots distance.

Figures 5-2 and Figure 5-3 show the signal intensity profile for both sampling modes with about 0.8 mJ (3 mW pulse power at 3.75 Hz repetition rate) average pulse energy. A laser pulse gives rise to a data point and the signals were taken for 1000 pulses. The results show that the signal magnitude for non-rotating impaction is about three times more than the signal for rotating impaction.

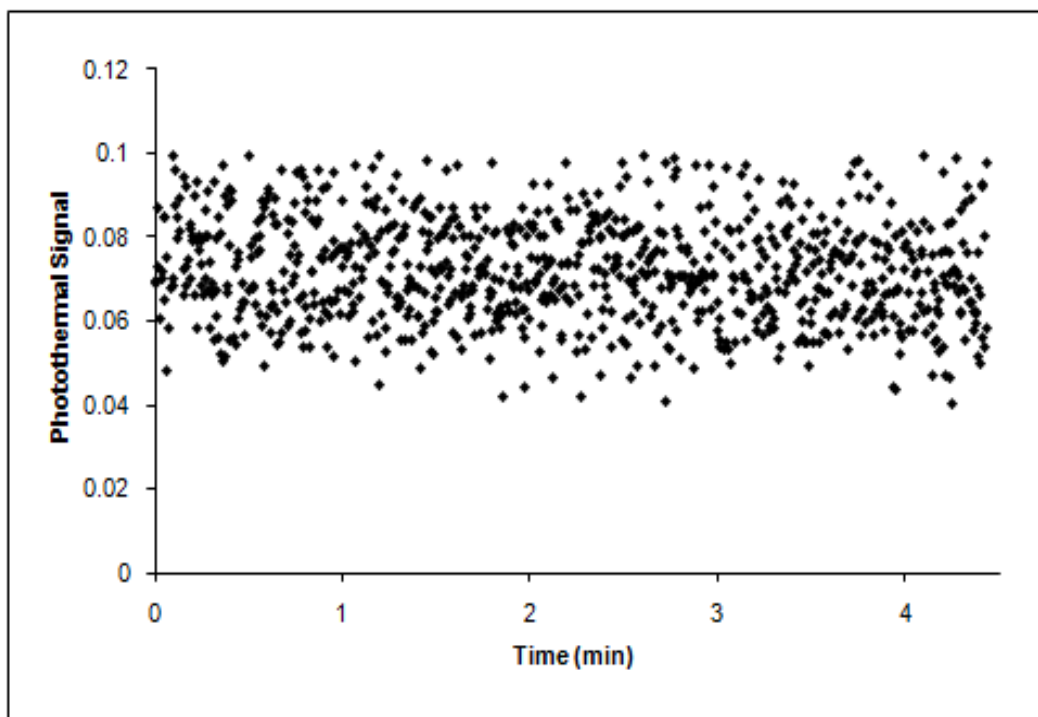


Figure 5-2. Pulse-to-pulse photothermal mirage signals from collected aerosols for individual spot from non-rotating impaction deposit

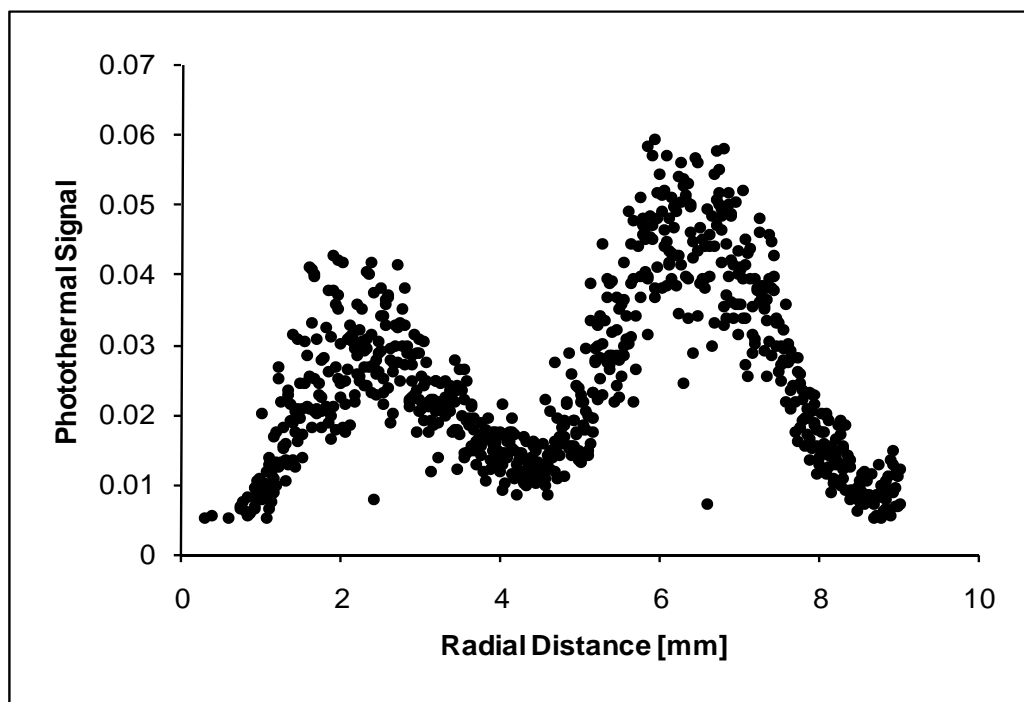


Figure 5-3. Pulse-to-pulse photothermal deflection signals from collected aerosols for radial scanning from rotating impaction deposit.

With low absorbance particles, absorbed energy is more likely to increase with deposit layers but particulate mass will not follow Beer's law if they are optically thick. Molar absorption coefficient for ammonium nitrate at 9.56 μm wavelength is about 2676 m^{-1} , therefore, higher signal in non-rotating impaction may be due to increase in deposit layers. Furthermore, the inherent complexity in analyzing rotating impaction deposit profile imperatively promotes the use of non rotating sampling method.

Time-dependent photothermal deflection measurement is also obtained for rotating impaction and non-rotating impaction mode. The signal profile reveals sample

depth dependent temporal thermal gradient in the surrounding air (Figure 5-4). The time-dependent signal profile for non-rotating impaction deposit is characterized with higher signal rise time indicating a time delay in heating the surrounding air, which increases with particle's size and number of layers.⁹

One of the advantages that are presented in the theories that describe photothermal spectroscopy is that the observed signal is directly proportional to the energy of the excitation laser pulse, implying that high-energy excitation pulses should

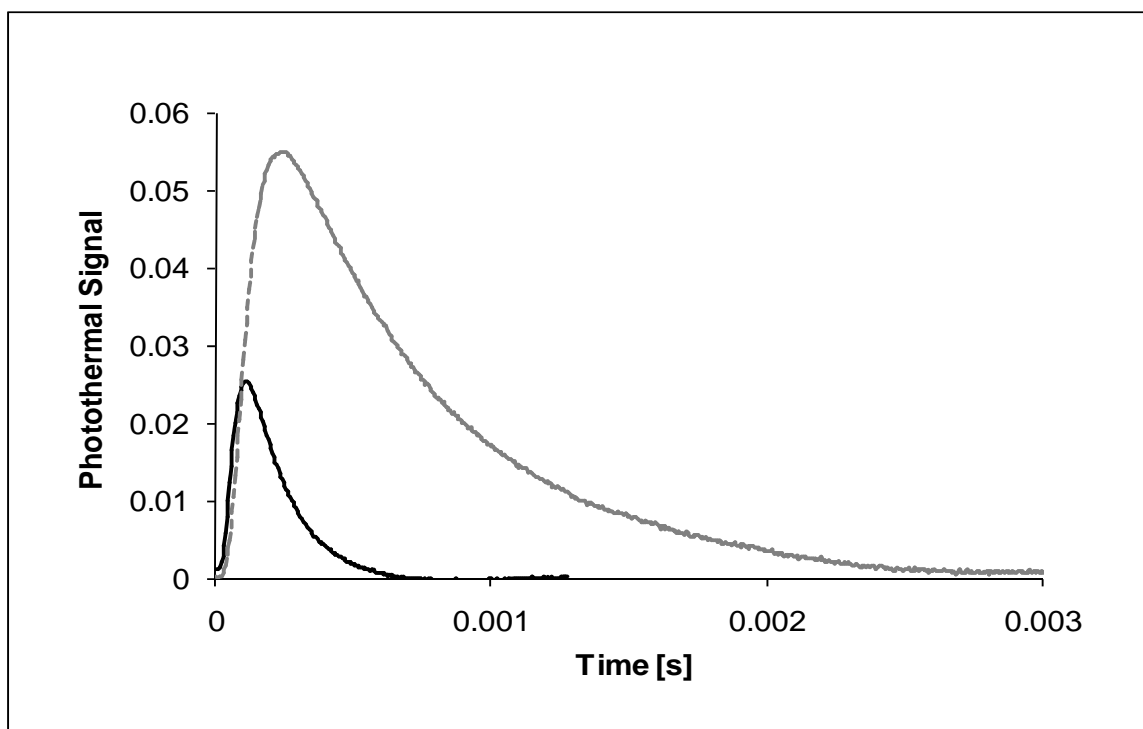


Figure 5-4. Time dependent photothermal mirage signal from collected aerosols for — rotating impaction deposit measured at a space region with high aerosol's deposit, — individual spot from non-rotating impaction deposit

provide optimal analytical sensitivity. Upon each pulse of the pump laser, photothermal deflection signal was estimated by using adaptive matched filter signal analysis. The CO₂ laser energy was monitored with A/D converter. Two separate data files were recorded for energy dependent signal measurement; one being the pump laser energy and the other the signal estimate per pulse.

Since the aerosols were collected on a non-coated surface, adhesion of particles is mainly due to particle-particle interaction and particle-surface interaction. One will expect loss of signal due to particle damage or desorption at relatively high pump beam fluence. In contrast, the energy dependent signal plot in Figure 5-5 is linear up to about

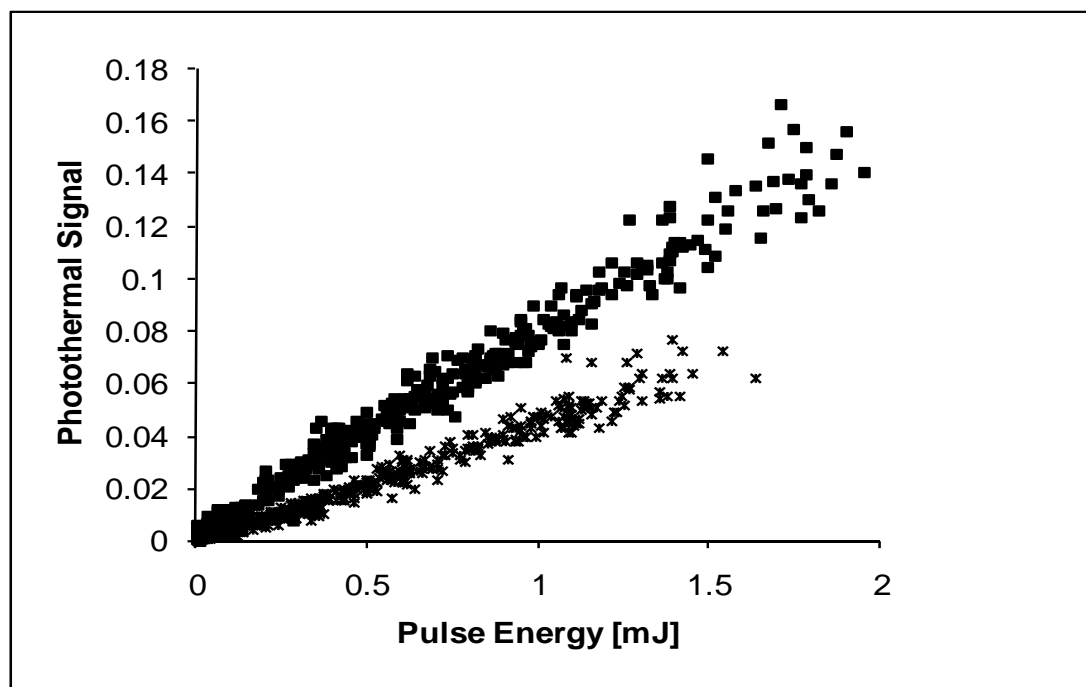


Figure 5-5. Energy dependent photothermal mirage signal from collected aerosols for:

- ◆ individual spot in non-rotating impaction, and *
- * rotating impaction deposit.

2 mJ pulse energy, indicating no detected damage of samples or loss of particles within the pulse energy range. Sensitivity for this method can further be improved by increasing the pump beam intensity.

Aerosols Mass Calibration. Numerical modeling results reported in Chapter 3 have shown that quantitative aerosol analysis will require calibration with standard aerosols since total signal from ensembles of particles does not equal linear addition of signals from individual particles. Aerosol standards are obtained by first calibrating the MOUDI with a microbalance. Aerosols are then simultaneously collected on stage 6, 7, and 8, and aerosol mass is obtained for different loading time. The impactor calibration curve is obtained by plotting the total mass against time. Figure 5-6 is the mass-time curve for stage 6, 7, and 8 of the MOUDI with rotating impaction plate. Operating the impactor with non-rotating plates produces individual spots with aggregates of aerosols: one spot for each nozzle of the impaction stage. Stage 5 and 6 of the impactor are used for the non-rotating impaction. On stage 5 and 6 of the impactor, there are 40 and 80 nozzles, respectively. Meaning there will be 40 individual spots for stage 5 and 80 individual spots for stage 6. Each of the aerosol spots generated from stage 5 is about 1 mm in diameter while aerosol spots generated from stage 6 is about 0.55 mm in diameter. The spatial distance between two spots is at least 3 mm.

In Figure 5-7, unlike rotating impaction method, the mass-loading time curve for non-rotating impaction method is linear up to about 30 minutes, indicating a low linear range compared to rotating impaction plate. This is because non-rotating impaction produces increased deposit layer and the total mass decreases with time due to adsorption

isotherm. This is not to say there is no isotherm associated with rotating impaction method, only that it will take a longer time before showing up. Although rotating impaction method produces higher mass-time linear range, the deposit patterns pose a difficult analysis for the photothermal measurement.

Since photothermal signals from rotating and non-rotating impaction suggest non-rotating impaction as a better sampling method, standard aerosols for calibration were collected on MOUDI stage 6 (0.56 μm particle diameter cut-off) with non-rotating impaction method for different times. Half of the germanium plate surface is covered with a #1 micro cover glass so that some aerosol spots are deposited on the glass surface.

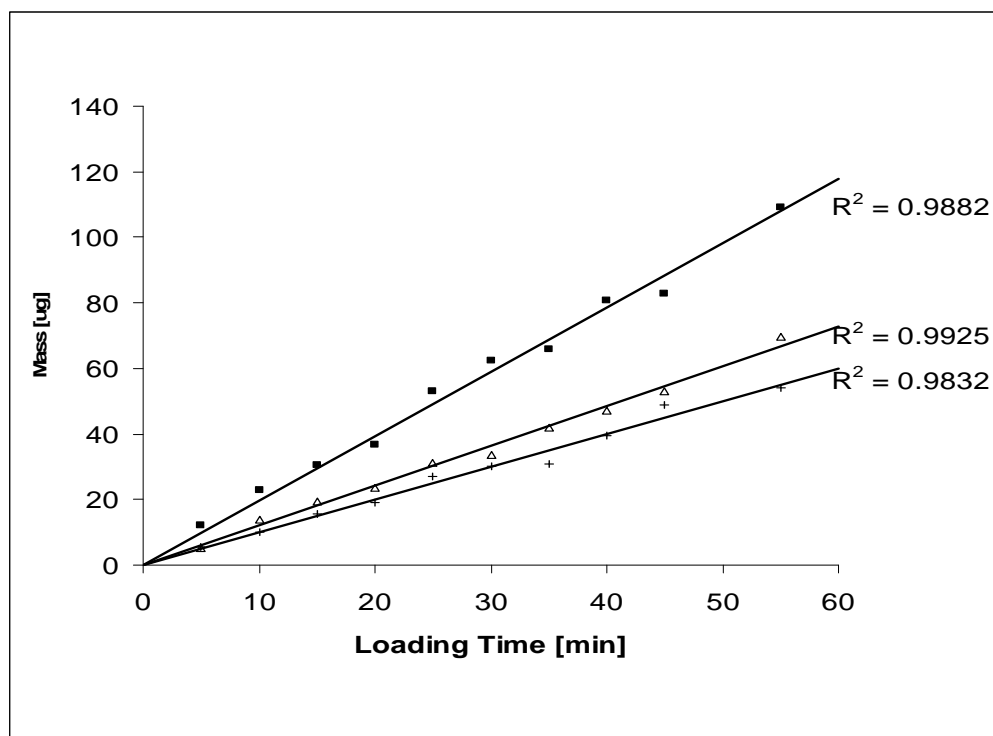


Figure 5-6. MOUDI mass calibration curve with rotating impaction plate. ♦ Stage 7,

△ Stage 8, + Stage 6.

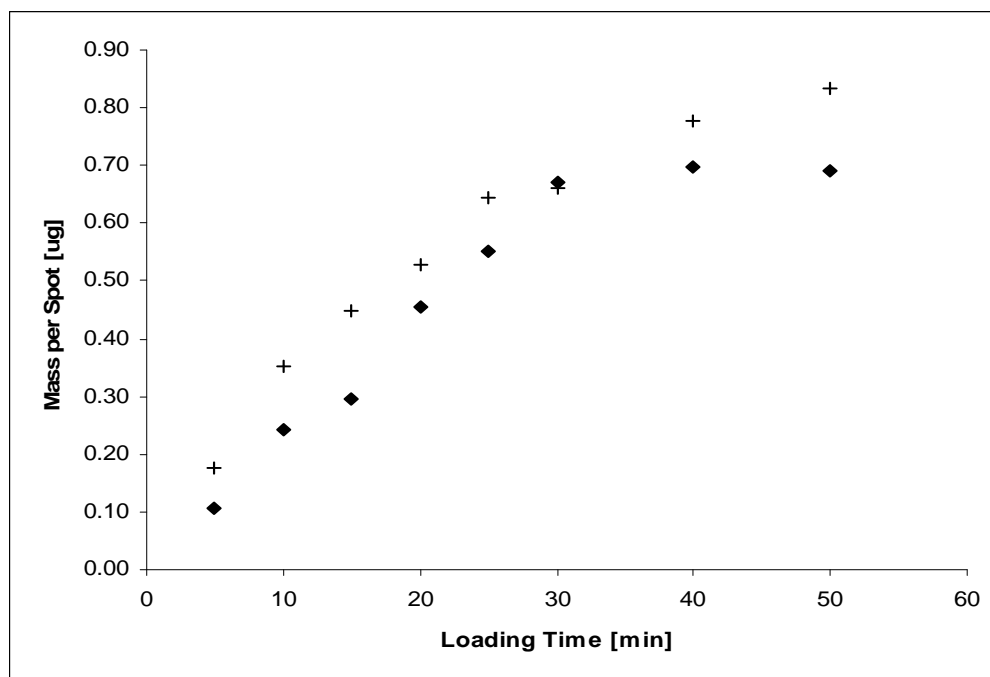


Figure 5-7. Mass - Collection time plot for non-rotating impaction deposits on: ♦ Stage 6, + Stage 5 of MOUDI.

Differential plate mass of aerosols deposited on glass are measure with a microbalance. Replicate measurements are obtained for each loading time and the average mass values are plotted against time. The mass-time plots (Figure 5-8) for MOUDI stage 6 showed linear relationship from 0 to 30 minutes loading time. Above 30 minutes, a nonlinear effect is observed which is mainly due to adsorption isotherm that is not accounted for in this report owing to the complexity of the adsorption mechanism.

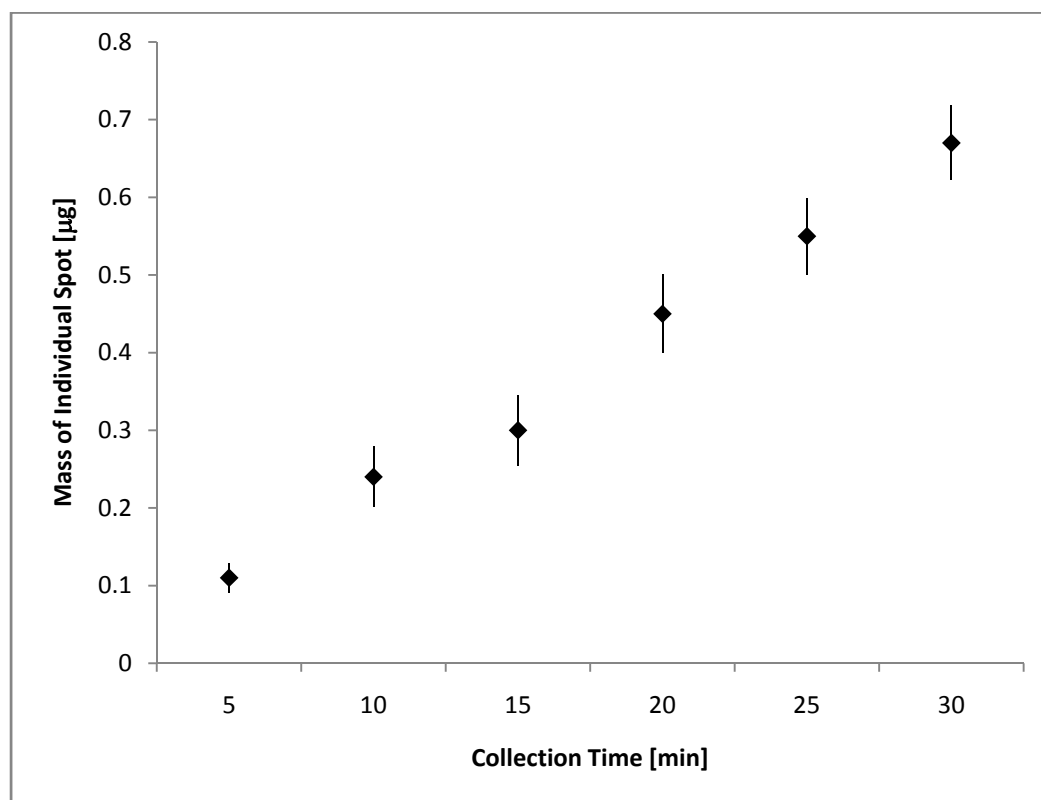


Figure 5-8. Standard curve for average mass loading of individual spot from stage 6 of MOUDI at different time.

Aerosols deposited on germanium plate are analyzed with photothermal deflection apparatus. Photothermal deflection signals from aerosols deposited on germanium plate are obtained by taking average of 200 data points. Predicted mass from MOUDI calibration was then used to scale photothermal signals to mass loading (Figure 5-9 and Figure 5-10).

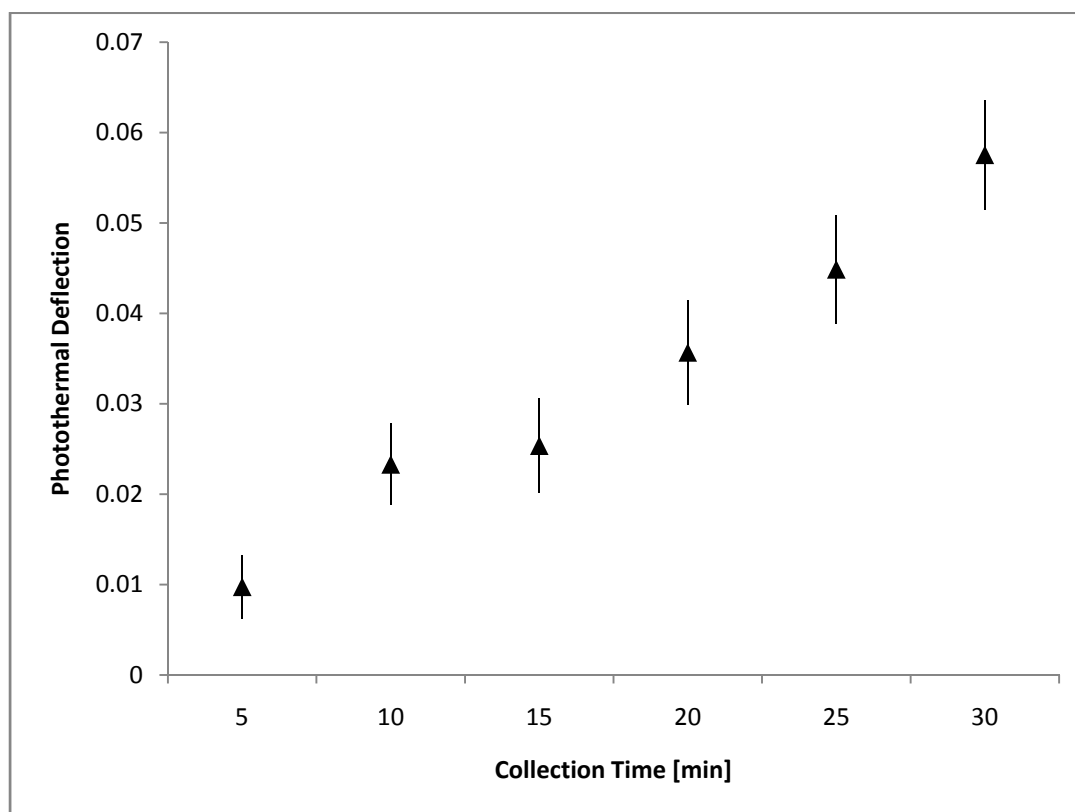


Figure 5-9. Signal-Collection time plot for photothermal deflection of aerosols collected on stage 6 of MOUDI with non-rotating impaction plate.

The detection limit ($3 \times$ blank standard deviation) from signal-mass curve is 7.31 ng. Aerosol mass concentration is calculated from MOUDI flow rate and collection time. A detection limit of $0.65 \mu\text{g m}^{-3}$ for 30 L/min flow rate and 30 min loading time is obtained, which is better than current analysis methods that uses filter sampling.

Uncertainty in measurements of aerosols with photothermal deflection is not that of sensitivity but that of intrinsic variability in sampling method. For 30 minutes collection time, relative error in mass calibration is less than 2%, which falls within an acceptable range.

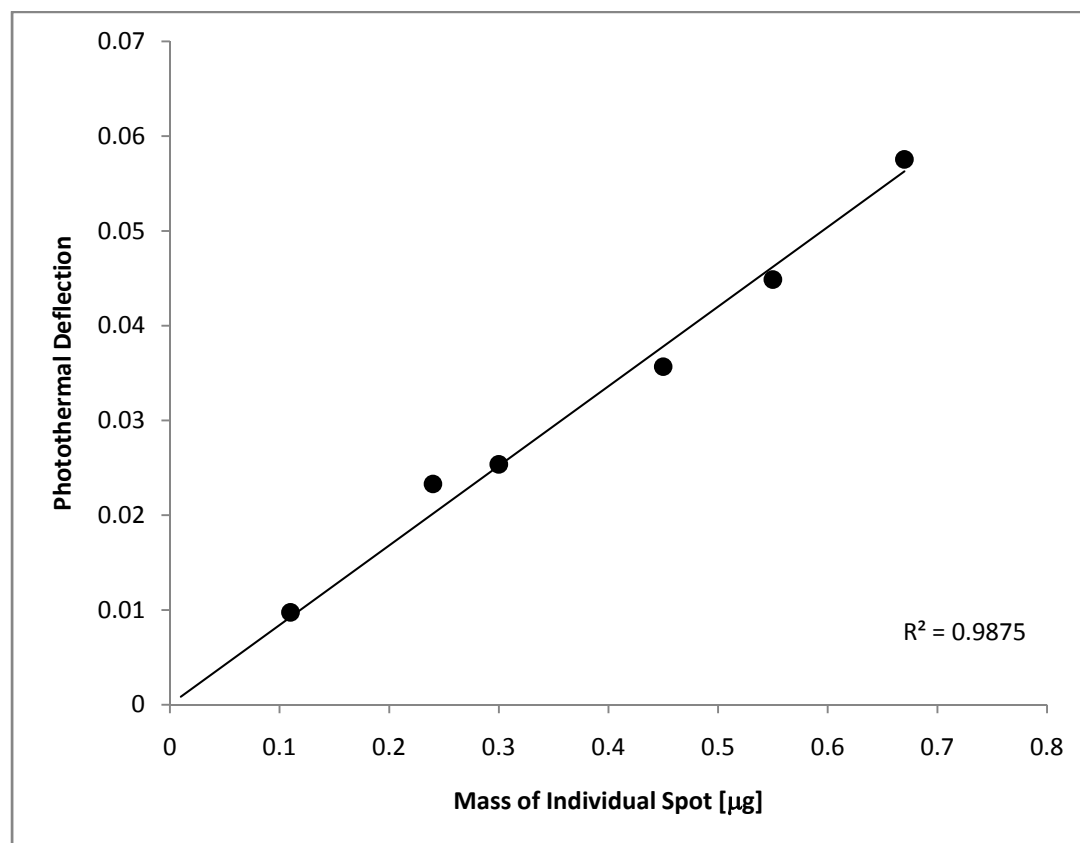


Figure 5-10. Standard plot of photothermal deflection signal with predicted mass loading for individual aerosol spot.

Uncertainty associated with sampling may further be reduced by using low pressure cascade impactor and substrates coated with optically transparent sticky material. Major sources of error associated with photothermal deflection measurements are either instrumental noise or source noise. These error sources and reduction method have been reported in literature.³⁵ Using appropriate optical setup and well-behaved laser light

source, such as quantum cascade laser, will generally improve sensitivity and accuracy of the photothermal apparatus.

Aerosol Number Concentration Measurements. Number concentration is another method of quantifying ambient aerosols. Condensation Nuclei Counter (CNC) and Cloud Condensation Nuclei Counter (CCNC) are commonly used to measure total aerosols number concentration larger than some minimum detectable sizes. In this section, determination of aerosol number concentration with photothermal deflection is demonstrated.

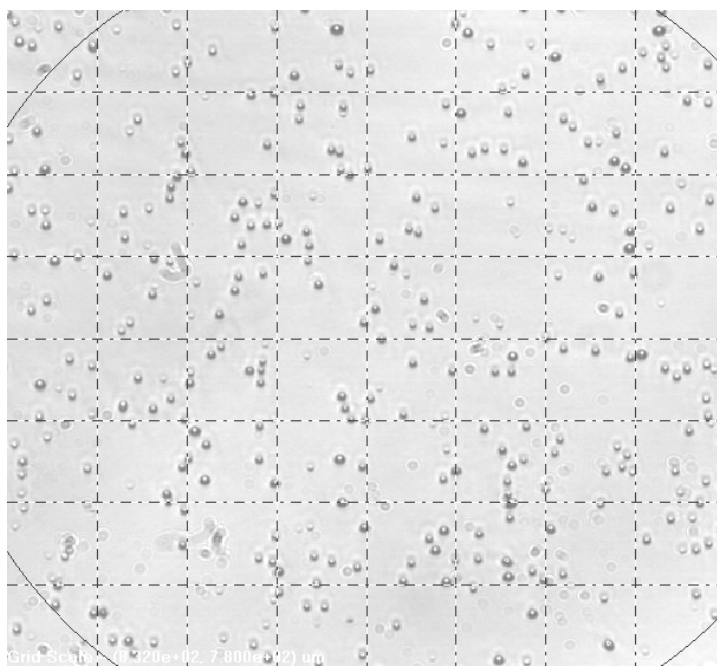
For photothermal deflection experiment, the aerosols deposited on a flat surface are first counted before probing with the photothermal deflection apparatus. For an accurate counting procedure, sample must be a monolayer particle deposit. In order to achieve this, the sampling method is modified by reducing the nebulizing pressure, loading time, the concentration of ammonium nitrate solution, and MOUDI flow rate. The aerosols are collected with non-rotating impaction plate on stage 5 in MOUDI at flow rate of 6 L/min. Half of the germanium plate is covered with a #1 microcover glass so that some aerosols fall on the glass. The particles distribution at a single spot is assumed to be uniform. The spots on the germanium plate are analyzed with photothermal deflection while those on glass are counted with an optical microscope.

MOUDI is designed to operate at 30 L/min in order to achieve the calibrated cut off sizes for different stages. There is need for particle size calibration since impactor flow rate is reduced to 6 L/min. Size calibration is performed with Melles Griot 10

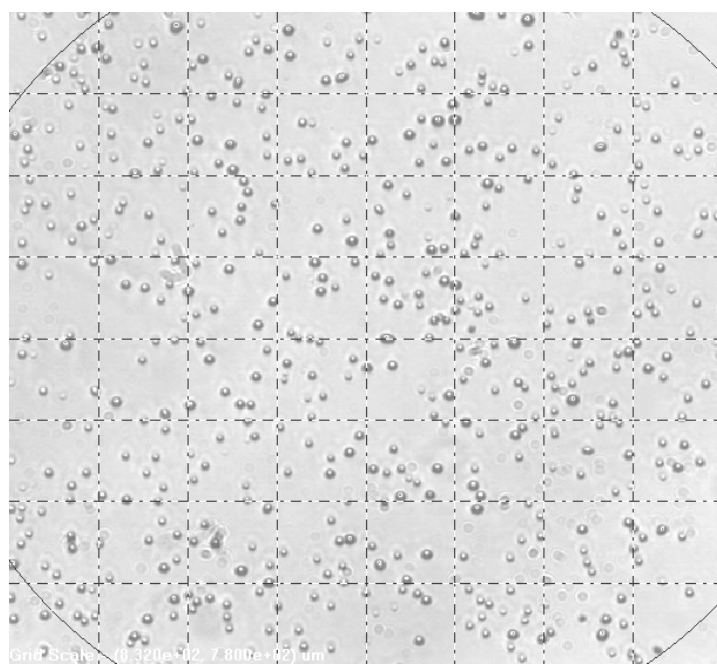
μm /unit standard ruling slide. The estimated average real size is about $3.0 \mu\text{m}$ with equivalent aerodynamic diameter of $4.1 \mu\text{m}$.

In order to obtain signal-number relationship from the photothermal measurement, a manual counting is employed using a Nikon microscope fitted with a Zeiss 46-20-46 (40 X) objective. The microscope is connected to a Sony Model XC-77RR CCD viewing camera for visualization and imaging. The camera is controlled by Spiricon LBA-PC software which is originally designed for laser beam profiling but was found to be a good tool in acquiring images from the CCD. Microscopic images of 5 randomly selected spots are saved with the LBA-PC software. Examples of the deposit images are shown in Figure 5-11 and Figure 5-12.

The software, configured with internal grid, divides the total surface area of the acquired image to 64 equal square units. The area of a unit square is calibrated with the Melles Griot standard ruling slide and was found to be $1600 \mu\text{m}^2$. Total number of particles sampled is obtained by summing counts from all the squares. Surface particle density (number of particles per unit area) is obtained by dividing total counts by sampled area. The counting process is repeated for five randomly chosen spots from every sample replicate. One-way ANOVA method is used to discriminate among spots and between plates.

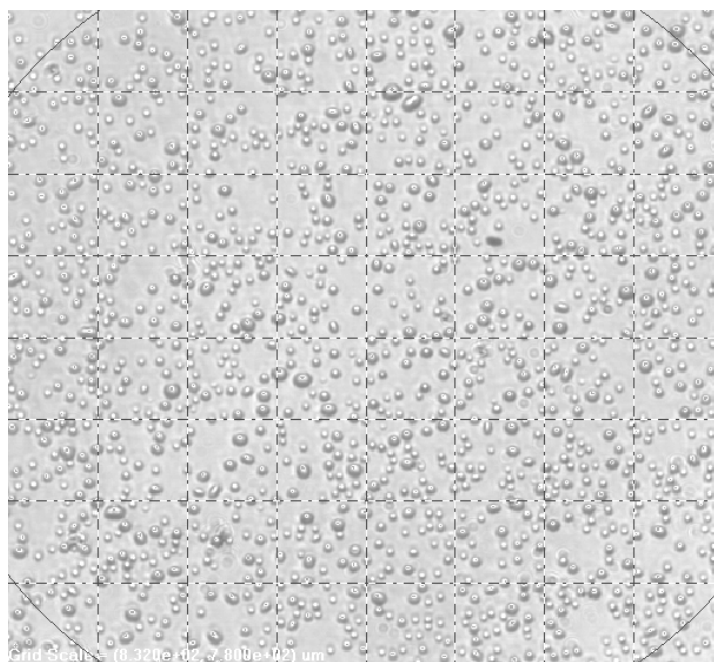


10 seconds

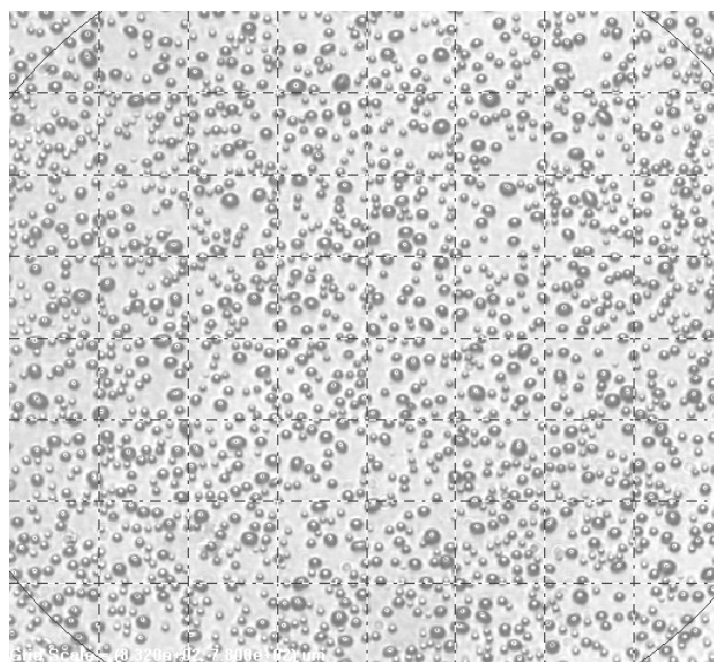


20 seconds

Figure 5-11. Images of aerosols on #1 micro plate collected for 10 seconds and 20 seconds.



60 seconds



120 seconds

Figure 5-12. Images of aerosols on #1 micro plate collected for 10 seconds and 20 seconds.

Aerosol “Pile-up” correction. Adsorption of hard spheres on solid surface with surface exclusion effect has been previously studied.³⁶⁻³⁹ The models proposed were based on empirical generalized Langmuir equation that does not take into account the force-convective flow mostly encountered in impaction sampling. The generalized equation for change in density with time has been given as

$$\frac{d\theta}{dt} = k_a C_0 \Phi(\theta) - k_d \theta \quad (5-4)$$

where k_a, k_d, C_0 retain their original definition in Langmuir equation.

Since there is no intention to develop new spherical particle adsorption kinetics, the common model of random sequential adsorption (RSA) configuration is assumed in estimation of monolayer surface area coverage (θ). RSA model assumes that particles are not allowed to diffuse on the surface and cannot desorb from it ($k_d = 0$). When N spheres of diameter d are adsorbed on a surface, the coverage is calculated by dividing the total projected area of the adsorbed spheres by the sampled surface area. Hence, for aerosol particle of diameter d , the time evolution monolayer unit surface coverage is given as

$$\theta(t) = \frac{n(t)\pi d^2}{4} \quad (5-5)$$

$n(t)$ is the time evolution surface particle density.

The surface extinction function $\Phi_{RSA}(\theta(t))$ defines the available fraction of the sampled areas and the probability that the new particle will adsorb on the surface in the presence of previously adsorbed particles. For entirely particle-free sampled area, the adsorbing probability of a particle arriving anywhere on the surface is unity. As the surface density of adsorbed particle increases the probability that the exclusion area (the area that cannot be occupied by the center of the projected area of new sphere) of two particles overlap is significant. Hence, the surface exclusion function as reported by Shaaf *et al.*³⁸ is given as

$$\Phi_{RSA}(\theta(t)) = 1 - 4\theta(t) + \frac{6\sqrt{3}}{\pi}\theta(t)^2 + 1.4069\theta(t)^3 + O\theta(t)^4 \quad (5-6)$$

Since Eq. 5-6 is only a function of coverage areas. At this point, a correction model based on the probability of pulse pile-up in photon counting statistics can be used to correct the aerosol pile-up effect on the particle counting. The time evolution aerosol deposition on the substrate with surface area A assumes a Poisson distribution with probability density function

$$P(n, \lambda AT) = \frac{(\lambda AT)^n e^{-\lambda AT}}{n!} \quad (5-7)$$

where T is time, λ is time evolution deposition rate, n is number of aerosols. The probability that aerosols pile-up occurs during the loading time is given as

$P_o = 1 - e^{-\lambda a}$. Where $\gamma = \Phi_{RSA}$. The probability that there is no pile-up, $e^{-\lambda a}$, is the required correction factor to adjust the measured count, and the actual count (adjusted counts), N_o ,

can be calculated from $N = N_0 e^{-\lambda a}$; where N is the measured count. The adjusted count-time curve shows that the “pile-up” effect is high at loading times above 90s as shown in Figure 5-13.

Aerosols Number Calibration. Aerosols number calibration is performed by collecting aerosols for different loading times. Three replicates for each loading time are obtained for the counting and photothermal measurement. The standard curve is obtained by plotting the mean count against loading time (Figure 5-13). The intercept on the vertical axis is due to false positive counts. The calibration curve shows some nonlinear effect above 90s which is probably due to the “pile-up” effects.

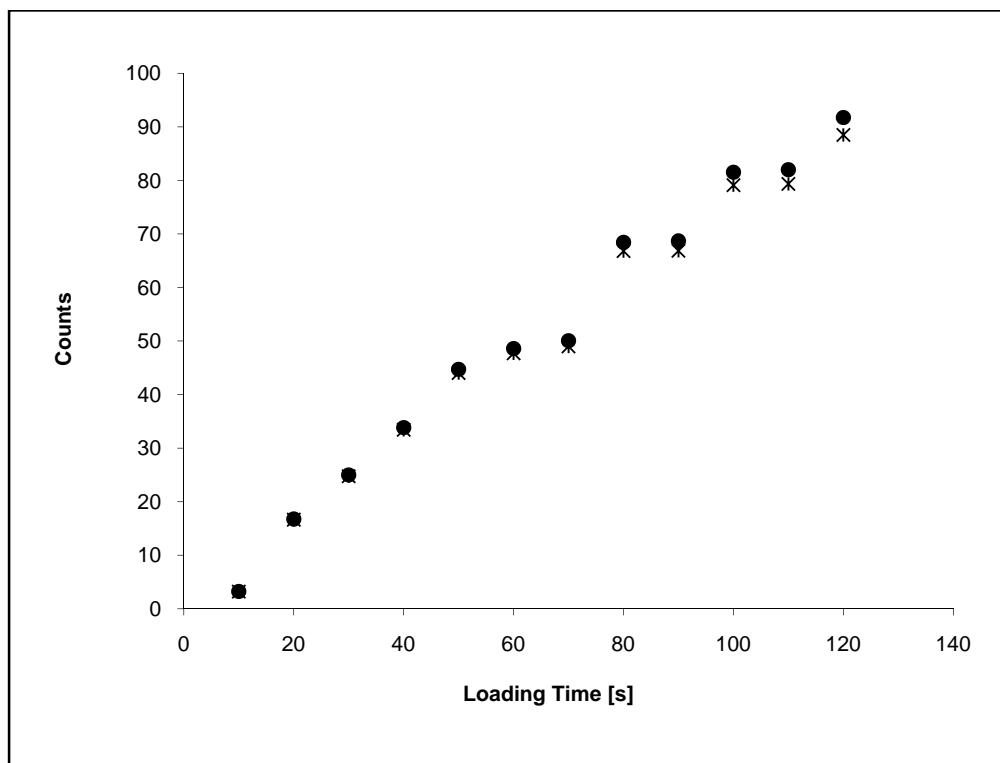


Figure 5-13. Counts-Loading time curve for impactor calibration. ●Adjusted count,
*measured count.

The associated error in the counting method is proportional to $1/\sqrt{n}$ where n is the mean number of particles. The error propagation curve (Figure 5-14) shows that counting error can be reduced to about 1% by increasing the loading time. Aerosols collected on germanium substrate were measured with the photothermal deflection apparatus. The apparatus is the same as described earlier except for the excitation beam radius. Excitation beam radius at the sample's surface is about 70 μm .

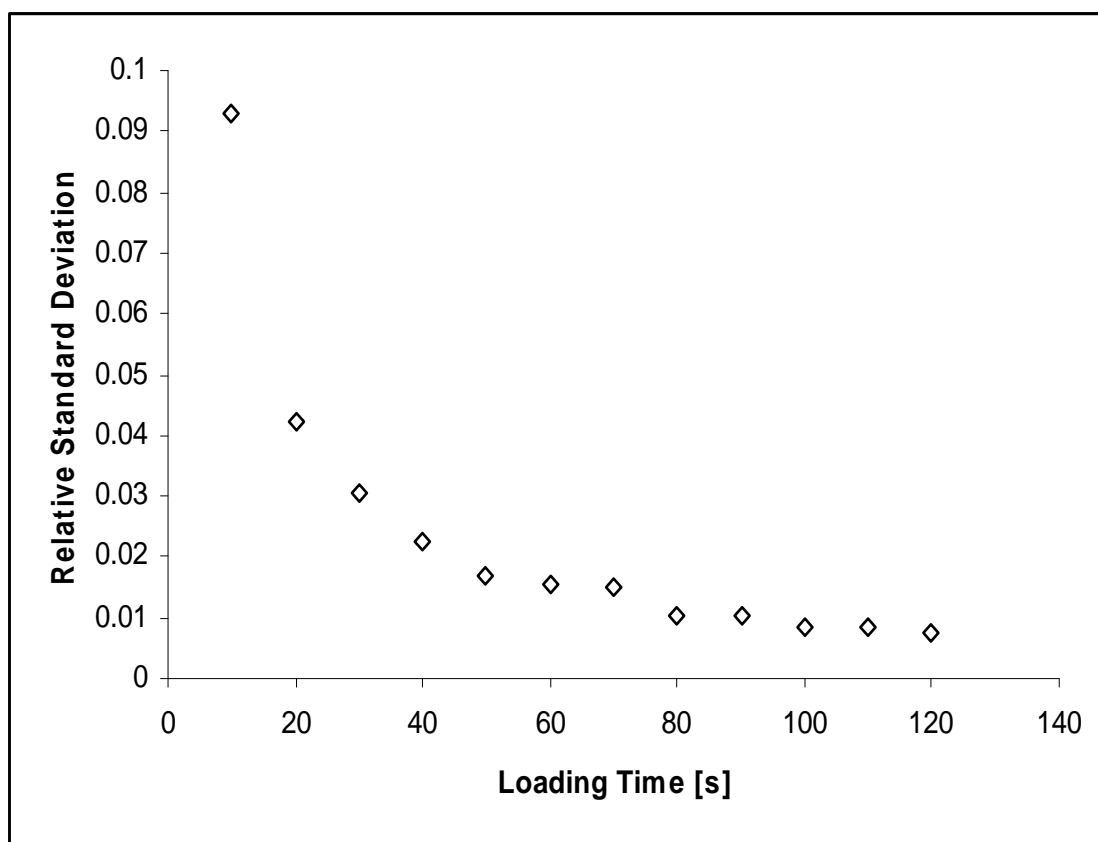


Figure 5-14. Relative standard deviation for count – loading time relationship.

For each of the sample replicates, five spots are randomly analyzed for the photothermal measurement. The mean photothermal signal is obtained by integrating 200 pulse-signals. The excitation beam projected area at the sample surface is $6362 \mu\text{m}^2$ which is much less than the area covered by individual aerosol spot. If we assume that particles that fall outside the probe area do not absorb the excitation laser energy then, the number of particles that produce the photothermal signals can be calculated as the product of the surface particle density and the excitation probe area. The mean value of photothermal deflection signal is plotted against the predicted counts from number-time curve. As shown in Figure 5-15, a linear relationship is observed for up to 120 s. The detection limit of 18 particles is obtained for average particle size of $3 \mu\text{m}$, which is equivalent to mass concentration of $0.1 \mu\text{g m}^{-3}$ for 30 L/min flow rate over 30 minutes collection time.

CONCLUSION

A photothermal method of detecting aerosols has been demonstrated. The technique promised to be sensitive for in situ analysis of atmospheric aerosols. Though the detection limits obtained are somehow higher than expected, the sensitivity is better than current analysis methods that are based on filter sampling and weighing. Potential source of variability appears to be irreproducibility of the collection method or the intrinsic variance due to aerosols probability distribution.

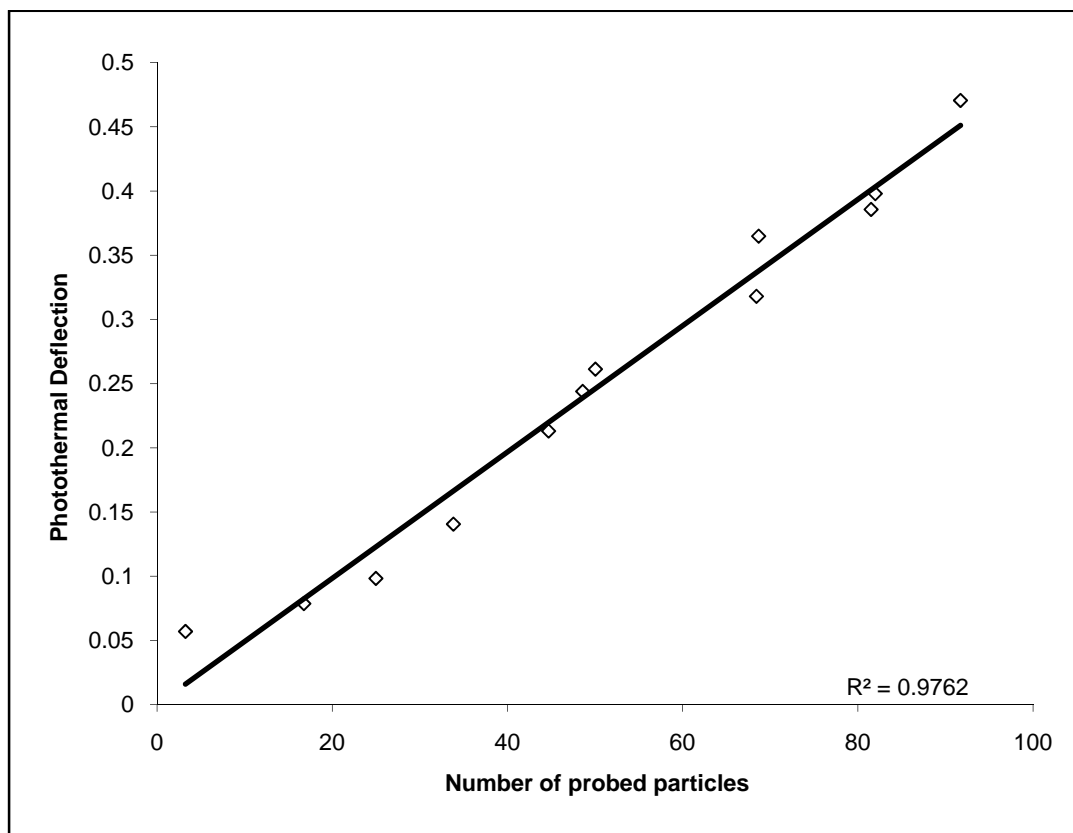


Figure 5-15. Photothermal deflection with number concentration standard curve.

REFERENCES

- 1 C. A. Pope, M. J. Thun, M. M. Mamboodiri, D. W. Dockery, J. S. Evans, F. E. Speizer, and C. W. Heath Jr., *American Journal of Respiratory and Critical Care Medicine* **151**, 669-674 (1995).
- 2 U.S.EPA, *National Ambient Air Quality Standards for Particulate Matter: Final Rule, Part II*. 2006; Vol. 71.
- 3 U.S.EPA, *Revision to Ambient Air Monitoring Regulations: Final Rule, Part III*. 2006; Vol. 71.

- 4 K. M. Adams, *Applied Optics* **27**, (19), 4052-4056 (1988).
- 5 K. M. Adams, L. I. J. Davis, S. M. Japar, and W. R. Pierson *Atmospheric Environment* **23**, (3), 693-700 (1989).
- 6 W. P. Arnott, H. Moosmuller, R. E. Abbott, M. D. Osssofsky, *Review of Scientific Instruments* **66**, (10), 4827-4833 (1995).
- 7 W. P. Arnott, H. Moosmuller, and C. F. Rogers, *Atmospheric Environment* **33**, (2845- 2852), (1999).
- 8 P. H. McMurry, *Atmospheric Environment* **34**, 1959-1999 (2000).
- 9 C. H. Chan, *Applied Physics Letters* **26**, (11), 628-630 (1975).
- 10 C. L. DeForest, J. Qian, and R. E. Miller, *Applied Optics* **41**, (27), 5804-5813 (2002).
- 11 H. S. Kwok, T. M. Rossi, W. S. Lau, and D. T. Shaw, *Optics Letters* **13**, (3), 192-194 (1988).
- 12 G. Sageev, and J. H. Seinfeld, *Applied Optics* **23**, (23), 4368-4374 (1984).
- 13 M. A. Schweitzer, and J. F. Power, *Applied Spectroscopy* **48**, (9), 1054-1075 (1994).
- 14 M. A. Schweitzer, and J. F. Power, *Applied Spectroscopy* **48**, (9), 1076-1087 (1994).
- 15 J. A. Sell, *Photothermal Investigation of Solids and Fluids*. Academic Press, New York, 1989.
- 16 M. A. Shannon, A. A. Rostami, and R. E. Russo, *Journal of Applied Physics* **71**, (1), 53-63 (1992).

- 17 L. A. Garnes, and D. T. Allen, *Aerosol Science and Technology* **36**, 983-992 (2002).
- 18 O. Hogrefe, F. Drewnick, G. G. Lala, J. J. Schwab, *Aerosol Science and Technology* **38**, 196-214 (2004).
- 19 D. Michaud, P. Picard, and M. Baril, *Aerosol Science and Technology* **31**, 323-337 (1999).
- 20 D. Michaud, P. Picard, and M. Baril, *Aerosol Science and Technology* **31**, 338-349 (1999).
- 21 P. Picard, D. Michaud, and M. Baril, *Aerosol Science and Technology* **31**, 350-357 (1999).
- 22 R. Rohl, J. W. Childers, and R. A. Palmer, *Applied Spectroscopy* **39**, 668-672 (1985).
- 23 L. C. Aamodt, and J. C. Murphy, *Journal of Applied Physics* **52**, (8), 4903-4914 (1981).
- 24 D. Bicanic, S. Kruger, P. Tores, B. Bein, and F. Harren, *Applied Spectroscopy* **43**, (1), 148-153 (1989).
- 25 L. C. Aamodt, and J. C. Murphy, *Journal of Applied Physics* **54**, (2), 581-591 (1983).
- 26 S. E. Bialkowski, *Photothermal Spectroscopy Methods for Chemical Analysis*. John Wiley and Sons, New York, 1996.
- 27 O. O. Dada, and S. E. Bialkowski, *Applied Spectroscopy* to be published, (2007).

- 28 D. Fournier, and A. C. Boccara, *Photothermal Investigations in Solids and Fluids*. Academic Press, New York, 1989.
- 29 E. L. Lasalle, F. Lepoutre, and J. P. Roger, *Journal of Applied Physics* **64**, (1), 1-5 (1988).
- 30 A. Mandelis, and R. F. Power, *Applied Optics* **27**, (16), 3397-3407 (1988).
- 31 J. C. Murphy, and L. C. Aamodt, *Journal of Applied Physics* **51**, (9), 4580-4588 (1980).
- 32 J. F. Power, and A. Mandelis, *Applied Optics* **27**, (16), 3408-3417 (1988).
- 33 M. J. Smith, and R. A. Palmer, *Applied Spectroscopy* **41**, (7), 1106-1113 (1987).
- 34 S. E. Bialkowski, *Review of Scientific Instruments* **58**, (4), 687-695 (1987).
- 35 G. R. Long, and S. E. Bialkowski, *Analytical Chemistry* **58**, 80-86 (1986).
- 36 I. Langmuir, *Journal of American Chemical Society* **38**, 2221-2295 (1916).
- 37 J. K. Mackenzie, *Journal of Chemical Physics* **37**, (4), 723-728 (1962).
- 38 P. Schaaf, and J. Talbot, *Journal of Chemical Physics* **91**, (7), 4401-4409 (1989).
- 39 R. A. Swendsen, *Physical Review A* **24**, (1), 504-508 (1981).

CHAPTER 6

CONTINUOUS LASER-EXCITED PHOTOTHERMAL SPECTROMETRY OF
CdS_xSe_{1-x} DOPED GLASSESⁱ

ABSTRACT

Photothermal lens measurements and finite element modeling are used to examine the physical changes taking place in optical filter glasses. Colored-glass and neutral density filters are found to have a strong positive temperature-dependent refractive index change. The overall positive refractive index change is thought to be a consequence of complex counteracting factors: stress-induced birefringence, polarizability, structural network and temperature-dependent carrier density changes in the CdS_xSe_{1-x} microcrystals that produce optical properties of these glasses. Finite element analysis (FEA) modeling is used to examine the temperature profiles and the goodness of the semi-infinite thermal diffusion solution normally used for thermal lens experiment. The results of FEA were used to optimize experimental parameters and calculate values of dn/dT for the glass by comparison with standard liquid samples.

ⁱCoauthored by Oluwatosin O. Dada, Mathew R. Jorgensen, and Stephen E. Bialkowski.

Reproduced with permission from *The Journal of Applied Spectroscopy*, vol. 62, p 1337.

Copyright 2007 Society for Applied Spectroscopy (see Appendix E).

INTRODUCTION

Some years back our laboratory started searching for standard materials that could be used to calibrate a photothermal lens apparatus without having to make-up liquid samples. It was thought that colored glass filters would serve as such a standard. Colored glass or volume-absorbing neutral density filters would be stable over time, could be easy to use, and the equivalent glass might be available to a number of researchers due to their wide-spread availability. If all researchers shared the same calibration, then measurements could be compared from laboratory to laboratory.

Two problems with using the glass optical filters were soon discovered. First, the colored glass and neutral density filters that we examined had anomalous physical properties. In particular, we find that these optical glasses have a positive temperature-dependent refractive index change coefficient. Second, heat transfer from a glass plate excited with a laser is far from the ideal situation described by the semi-infinite cylinder approximate models that are most often used to describe the photothermal lens experiment.

Nanoparticles of semiconductor materials are often responsible for the optical absorption in commercial colored glass filters. The chemical composition, size, and method of synthesis of the nanoparticles affect optical properties of the glass filters of which are mostly highpass wavelength cut-off filters used in spectroscopy and other optical technology.¹ Commercial colored glass wavelength cutoff filters utilize semiconductor nanoparticles on the order of 10 nm.²⁻⁵ Pereira *et al.*⁶ reported the

complexity of the solution to theoretical treatment of the thermally induced bistability in SDG due to thermal lens effect.

Photothermal lens spectrometry is based on the measurement of refractive index changes that occur upon optical excitation.^{7,8} When a medium absorbs electromagnetic radiation, all or a fraction of the excitation energy is converted to heat. The heat increases temperature and causes a refractive index change. A low-power probe laser is used to monitor the refractive index change. In the case of photothermal lens spectrometry, the probe laser will focus or defocus relative to the normal beam propagation due to the transient lens. The change in probe laser beam propagation allows the determination of the refractive index change. Models are used to calculate temperature changes resulting from the absorption of excitation laser power. The combination of experiment and theory, then, allows one to determine the temperature-dependent refractive index change, dn/dT , for the transparent sample.

Among the currently used thermo-optical techniques, thermal lens and thermal deflection have received enormous interest from many authors of which the most widely known and used is thermal lens.⁹ Theoretical models of thermal lens effects in fluids are well established though a number of approximations are commonly used to obtain tractable analytical results.^{10, 11} Obtaining accurate theoretical descriptions of thermal diffusion in solids excited by laser beams is still an active area of research. The use of thermal lens for analysis of transparent solid materials has been reported by some authors.^{12, 13}

We present in this chapter experimental and modeling investigations of thermal lensing in colored glass filters and ethanol solutions contained in sample cuvettes. The aim of this paper is to describe qualitatively the temperature profile and refractive index change in our sample due to absorption of laser light irradiation by the sample. Thermal lens spectrometry is modeled as simply being proportional to the inverse photothermal lens strength. The result in transmittance mode was compared with that of liquid in conventional cuvette. Thermal lens experiments in reflection mode and thermal deflection confirmed the induced thermal expansion in the sample and the heat transfer to the coupling fluid, in this case, air. Finite element analysis (FEA) is used to investigate analytical solution to the temperature profile in solution and solid samples. FEA modeling is described and model results are compared to the usual semi-infinite cylinder approximations.

THEORY

The photothermal lens signal is dependent on the spatial-dependent refractive index change produced when energy deposited in the absorbing sample produces a temperature change. The time- and space-dependent temperature change is described by the differential equation for thermal diffusion. In radial symmetry, appropriate using lasers for sample excitation, the equation describing heat diffusion is

$$\frac{\partial}{\partial t} \delta T(r, z) - D_T \nabla^2 \delta T(r, z) = \frac{U(r, z)}{\rho C_p} \quad (6-1)$$

In this equation, $\delta T(r, z)$ (K) is the spatially dependent temperature change. The radial coordinate is r (m) while the linear cylinder coordinate is z (m). The time, t (s), dependence is implicit. The rate of heat transfer is governed by the thermal diffusion coefficient, D_T ($\text{m}^2 \text{s}^{-1}$). The right-hand side of this equation is the temperature change source. $U(r, z)$ (W m^{-3}) is the spatially dependent energy density, ρ (kg m^{-3}) is density and C_P ($\text{J kg}^{-1} \text{K}^{-1}$) is heat capacity of the sample.

Optical absorption within the sample results in sample heating at a rate that mimics the excitation laser beam profile. The absorbed power density for collimated continuous Gaussian-profile laser irradiation propagating on the z -axis is

$$U(r, z) = \alpha e^{-\alpha z} \frac{2\Phi_0}{\pi w^2} e^{-2r^2/w^2} \quad (6-2)$$

Φ_0 (W) is the incident laser power, α (m^{-1}) is the exponential absorption coefficient and w (m) is the excitation beam waist at the sample position. The z -axis origin is taken to be at the entrance interface of the sample.

The strength of the photothermal lens element is found from the second radial derivative, evaluated on-axis. Integration over pathlength results in the inverse lens strength,

$$\frac{1}{f(t)} = \left(\frac{dn}{dT} \right) \int_{z=0}^{z=l} \left. \frac{d^2}{dr^2} \delta T(r, z; t) \right|_{r=0} dz \quad (6-3)$$

dn/dT (K^{-1}) is the temperature-dependent refractive index change also known as the thermal-optical coefficient. This equation is strictly valid for parabolic temperature change distributions. However, the temperature change is not necessarily parabolic. So the probe laser should have a smaller diameter than the temperature change distribution for Eq. 6-3 to be valid. This may be true with continuous excitation since thermal diffusion broadens the temperature change relative to the region of excitation.

The photothermal lens signal is related to the inverse focal length. While it is dependent on the beam propagation characteristics of the particular apparatus, the experimental signal, $S(t)$, calculated from

$$S(t) = \frac{\Phi_p(t=0)}{\Phi_p(t)} - 1 \quad (6-4)$$

is generally proportional to the inverse focal length as $S(t) \approx -2z'/f(t)$. In Equation 6-4, $\Phi_p(t)$ (W) is the irradiance of the probe laser passing through a pinhole aperture placed far away from the sample and the probe laser is focused a distance z' (m) in front of the sample.

The photothermal lens strength can be found by numerical integration of the heat diffusion differential equation with appropriate boundary conditions. Analytical solutions of the lens strength can be obtained by making several approximation assumptions. First, it is assumed that there is negligible thermal diffusion through the sample cell windows, or the sample-air interface in the case of solid (*e.g.*, glass plate) samples. Second, it is assumed that there is no significant attenuation of the excitation laser passing through the

sample. In this case the exponential term containing the optical absorption coefficient, α , is set equal to unity. With these assumptions, the solution to Eq. 6-1 using Eqs. 6-2 and 6-3 is⁷

$$\frac{1}{f(t)} = \left(\frac{dn}{dT} \right) \frac{\Phi_0 \alpha l Y_H}{\pi k w^2 (1 + t_c / 2t)} \quad (6-5)$$

The heat yield, Y_H , term is used to account for finite heat yield in cases where energy is lost through luminescence, l (m) is the sample pathlength, t_c (s) is the characteristic thermal diffusion time constant defined by

$$t_c = \frac{w^2}{4D_T} \quad (6-6)$$

$D_T = k/\rho C_p$ is the thermal diffusion coefficient and k ($\text{J K}^{-1} \text{m}^{-1} \text{s}^{-1}$) is the thermal conductivity.

With liquid sample, dn/dT is usually negative so that the thermal lens is negative where thermal expansion is the overriding contributing factor in dn/dT . For glass, it has been shown by L. Prod'homme¹⁴ that

$$\frac{dn}{dT} = \frac{(n_0^2 - 1)(n_0^2 + 2)}{6n_0^2} \left[\frac{1}{\gamma} \frac{d\gamma}{dT} - 3\beta \right] \quad (6-7)$$

where $\beta = 1/V(dV/dT)_P$ (K^{-1}) is the volume expansion coefficient and γ is polarizability. The form of this result implies that, depending on the glass structure, dn/dT can either be negative or positive. A structure with high expansive network will result in negative temperature-dependent refractive index. The later is normal for gases and liquids, and many solids as well. On the other hand, large positive temperature-dependent polarizability term can result in an overall positive dn/dT . With few exceptions, in particular near phase-change temperatures, most materials expand with increased temperature. But there are mechanisms for increasing refractive index with temperature. Solid phase changes, expansion induced stress, semiconductor conduction band population changes, and production of new states may result in a positive temperature-dependent refractive index change.

EXPERIMENTAL

Thermal Lensing Apparatus. The diagram in Figure 6-1 illustrates the apparatus setup for the thermal lens experiment. A continuous-wave Ar^+ laser (Coherent Innova 90, Model 90-6) operating at 514.5 nm is used as excitation source and 632.6 nm He-Ne laser (Uniphase, Model 1107P) is used to probe the resulting photothermal signal. We favor colinear dual-beam geometry for our thermal lens experiments. The distance between the sample and the photodiode detector is optimized to satisfy the far-field paraxial approximation. Two lenses (10 cm and 25 cm focal length) are used to focus the excitation beam in the sample and after the He-Ne beam focus.

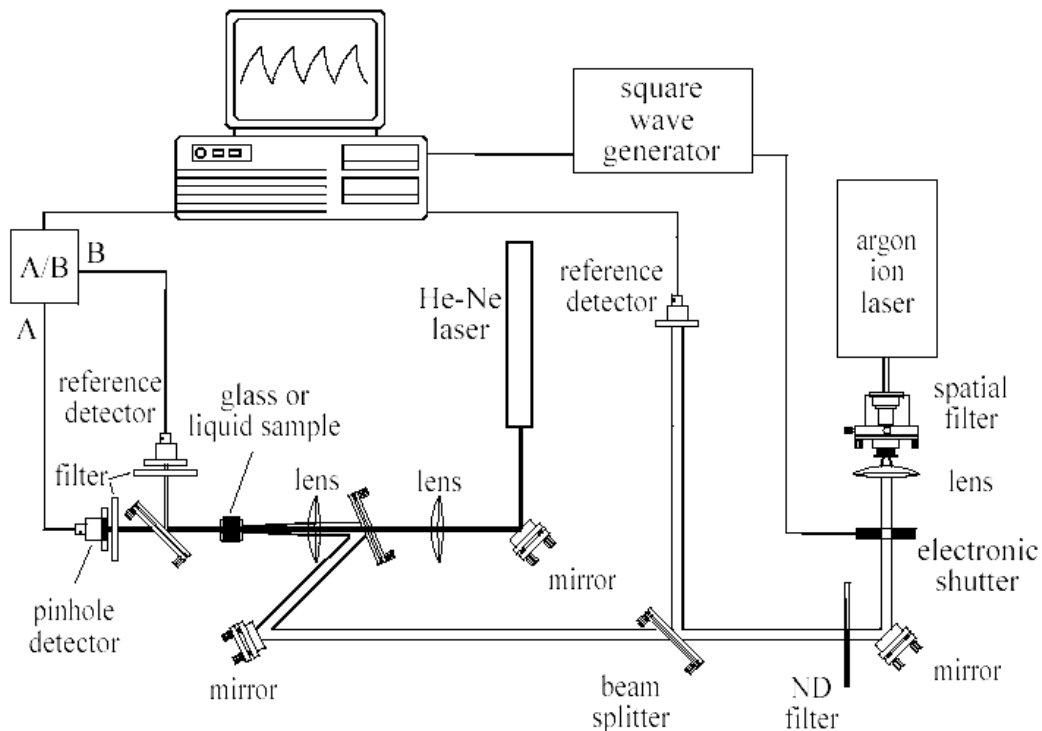


Figure 6-1. Apparatus for transmission thermal lens experiment. Detector 1 measures variation in He-Ne laser beam intensity. Detector 2 is set to measure the reference beam. The operational divider is used to process the signal as ratio of the real signal to the reference multiply by 10.

The excitation beam is modulated with Wavetek model 184 operated with Newport model 845 digital shutter and excitation source power is measured with a Scientech model 36-001 laser power monitor. The photothermal lens caused blooming or focusing of the probe laser. This is measured as a change in the power at the center of the beam. The center He-Ne beam power is measured using pinhole and a United Detector Technology (UDT) Model PIN-10DP photovoltaic photodiode detector. These detectors

have large, 1 cm diameter active areas for easy setup. A 632.8 nm laser line bandpass filter is used to prevent transmitted Ar⁺ laser beam from being detected by photodiode detector. A small fraction of the probe beam is split off prior to the pinhole aperture and a second bandpass filter/photodiode is used to monitor the probe laser power past the sample. Changes in the probe laser power are compensated for using an operational amplifier divider, the circuit which divides the thermal lens signal by the signal proportional to the He-Ne laser power. Photodiodes are often saturated by laser light sources. The photodiode signals are checked for linearity with neutral density filters.

This probe laser power compensated thermal lens signal is amplified and electronically filtered with a Tektronix model AM-502 differential amplifier. The analog signal is subsequently digitized with a 16-bit analog-to digital converter board and processed by multichannel analysis software. The latter averages several signal transients. Multichannel averaging was performed to improve the raw photothermal lens signal estimation precision. The photothermal lens signal was calculated from this raw data using a simple spreadsheet program.

Photothermal reflection lens experiments used an apparatus similar to that of the transmittance mode experiments. For these experiments the photothermal lens detector, consisting of the pinhole aperture, He-Ne laser line filter, and PIN photodiode, is positioned at an angle of about 10° to monitor variation in the power in the center of the probe laser beam reflected from the glass surface.

The transverse photothermal deflection (PDS) apparatus used in these studies is similar to those described by Boccara *et al.*¹⁵ The excitation and probe lasers are the same

as those used in the thermal lens experiment apparatus described above. Beam deflection angle is measured by a segmented position-sensing bi-cell detector (United Detector Technology PIN bi-cell detector with a Model 301-DIV analog processor). The resulting signal was also amplified with a Tektronix AM-502 differential amplifier and subsequently digitized with a 16-bit analog-to digital converter board with multichannel averaging software written in C++ computer language. Further data processing is performed on a PC with spreadsheet program.

Finite Element Analysis. Finite element analysis software provides numerical solutions to the heat transfer equations with the realistic boundary conditions imposed by the complicated experimental geometries. To better understand the transient temperature profile in the samples, finite element analysis is used to model stationary temperature changes. Result of finite element analysis is then compared to conventional analytical solutions to gage error. Experimental setup and apparatus constraints are guided by the error analysis. Analysis based on Comsol Femlab v 3.1 is carried out on a personal computer (Compaq Presario SR1330x, AMD Athlon XP 3200 processor). Analysis follows the steps below:

1. Define sample geometry and specify materials, boundary conditions, heat sources and sinks.
2. First solve problems with rough finite element definition and further refine elements and domain.
3. Get dT either at single time, time series, or at steady-state

The relative photothermal lens signal strength is found from Eq. 6-3. However the dn/dT is not known and so is taken as being unity. The path integral of the second radial derivative was found by either a) exporting two temperature change rays into a text file, reading the text file into a MS Excel spreadsheet, and calculating the second derivative from the ray data or b) using the Comsol Integration coupling variable to integrate 2nd derivative function of the temperature change ray.

To find the $d^2 \delta T/dr^2$ using the first method, the temperature change along two rays, one at $r = 0$, $\delta T(0)$ and the other at a small radius, $\delta T(r)$. The temperature change is assumed to be parabolic near the optical axis so that $\delta T(r) = a + br^2$, where a and b are constants. With the parabolic approximation, $d^2 \delta T/dr^2 = 2b$. It is easy to show that $b = [\delta T(0) - \delta T(r)]/r^2$ and thus $d^2 \delta T/dr^2 = 2[\delta T(0) - \delta T(r)]/r^2$. The only caveat is that the radius must be small.

Small square glasses (5 cm x 5 cm x 0.5 cm and 5 cm x 5 cm x 0.1 cm) were modeled using Comsol Multiphysics to represent the actual glass sample used in the experiment. For convenience, the glass was modeled with the origin at the center of one of the square faces so that the z -axis runs along the pathlength of the excitation and probe beams. The temperature profile of the glass square was obtained by having the FEA software solve the heat equation with the boundaries set at zero degrees (assuming no convective heat transfer at the surfaces) and heat input along the z -axis defined by Eq. 6-2 where $r = \sqrt{x^2 + y^2}$, and the other parameters remain as defined. This way, the temperature solution represents δT . The model was solved using steady state conditions,

not considering convection because the sample is solid. The values of α , Φ_0 , and w used were 29.7 m^{-1} , 75 mW, and 160 μm , respectively.

Samples. Commercial standard 5 cm \times 5 cm colored glass wavelength cutoff made with $\text{CdS}_x\text{Se}_{1-x}$ microcrystal in the order of 10nm is investigated as an absorbing solid material. Corning 3750 (CS3-79 5 mm thickness) and Schott NG 11 (1 mm thickness), glass filters were used. Solutions of iron (II) dicylopentadiene (FeCp_2) in ethanol were used as our liquid standards. Linear dilution is used to obtain lower absorbance from stock solutions of high enough absorbance to measure using a spectrophotometer in a conventional 1 cm pathlength liquid cuvette. NSG Precision Cells, Inc. 10 \times 5 mm and 10 \times 2 mm cuvettes were used to approximate the pathlength in the solid samples. The sample is positioned at the focus of the excitation beam for maximum temperature gradient, and the solid versus liquid experiment is carried out separately at room temperature under the same condition. Sample absorbances were recorded with Shimadzu UV-2401 spectrophotometer.

RESULTS AND DISCUSSION

Thermal lens theories were developed mainly with consideration of liquid phase experiment in which dn/dT is negative. For glasses, dn/dT can either be negative or positive due to many counteracting effects.^{17, 18} S. M. Lima *et al.*² gave an insight of different factors that can lead to positive refractive index gradient in solids.

Glasses are reported to exhibit high $\chi^{(3)}$ and photodarkening effects giving rise to optical phase conjugates. The nonlinear absorption coefficient and index of refraction

change in SDG are due to photodarkening effect. The latter is attributed to a photochemical process in the semiconductor microcrystallite.¹⁹

Trends in the nonlinear properties of SDG may also depend on the band-gap wavelength. Band-gap wavelengths of 490.1 nm and 713.9 nm at room temperature have been reported for CdS and CdSe, respectively, and linear interpolation between the two wavelengths can be used to estimate the band-gap wavelength for $\text{CdS}_x\text{Se}_{1-x}$.^{20, 21} The nonlinear refractive index change is expected to be positive in the SDG at excitation wavelength below the band-gap wavelength and negative at wavelengths above the band-gap wavelength.

We have presented thermal lens experiment and finite element modeling to investigate the temperature profile and change in refractive index in $\text{CdS}_x\text{Se}_{1-x}$ -doped glass. Figures 6-2, 6-3, and 6-4 show the experimental thermal lens signal for commercial colored glasses and FeCp_2 in transmittance mode with excitation beam operated at 514.5nm and excitation power of 75mW. Conventional thermal lens signal is expected to correspond with negative change in refractive index induced by a temperature gradient perturbation as a result of absorption of the excitation energy by the sample. Thermal lens signal (arbitrary unit) for FeCp_2 solution with measured absorbance of 0.000375 AU for 5 mm pathlength (Figure 6-2) indicates a decrease in refractive index of the sample. The thermal lens signals of Corning and Schott commercial glass filters, which have lower molar absorption compared to the liquid (Figure 6-3 & Figure 6-4) are inverted contrarily, which indicates increase in refractive index.

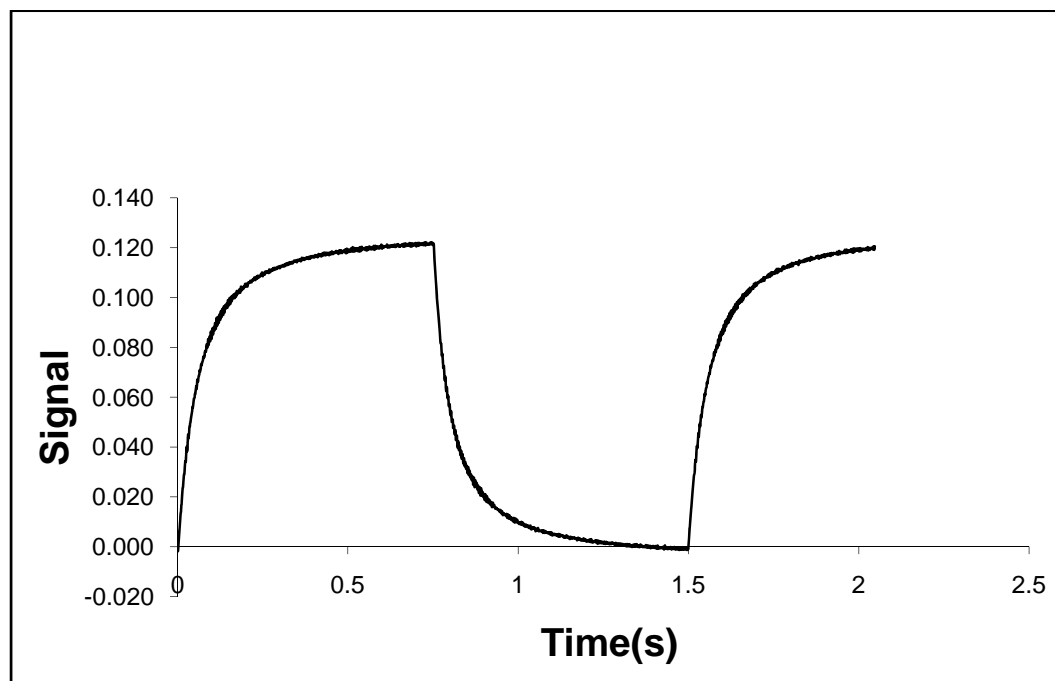


Figure 6-2. Experimental thermal lens signals for standard quartz cuvette containing a FeCp_2 ethanol solution in a quartz cuvette.

We observed the same trend in the signal for glass filters that are doped with other materials rather than the semiconductor microcrystals, for example the Schott's neutral density filters. This shows that positive dn/dT cannot only be as a result of semiconductor microcrystal.

S. M. Lima *et al.*² have reported positive dn/dT in their experiment due to counteracting induced stress in the glass material. The experimental FeCp_2 signal magnitude is large compared to glass at the same absorbance while the time constant for glass signal is shorter than the FeCp_2 solution due to the microcrystallites and thermal heat coupling with the surrounding fluid.

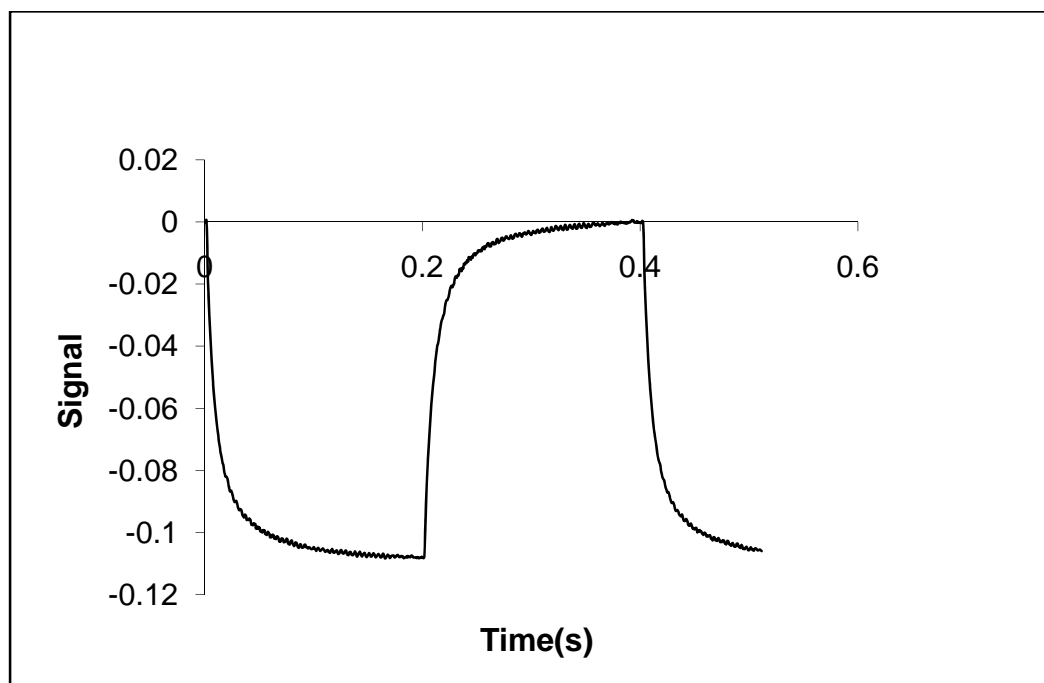


Figure 6-3. Experimental thermal lens signals for 5 mm thickness $\text{CdS}_x\text{Se}_{1-x}$ doped Corning glass filter.

The signal output in this experiment is consistent with previous methods reported.²¹ The excitation beam wavelength falls below the $\text{CdS}_x\text{Se}_{1-x}$ band-gap wavelength, which produces a positive refractive index change due to increased carrier density.

Photothermal reflection experiment which measures the variation in reflected beam due to “photothermal bump” on the surface of the glass confirmed induced thermal expansion within the glass. Indirect photothermal refractive index gradient measurements popularly known as photothermal deflection also confirm thermal heat transfer between

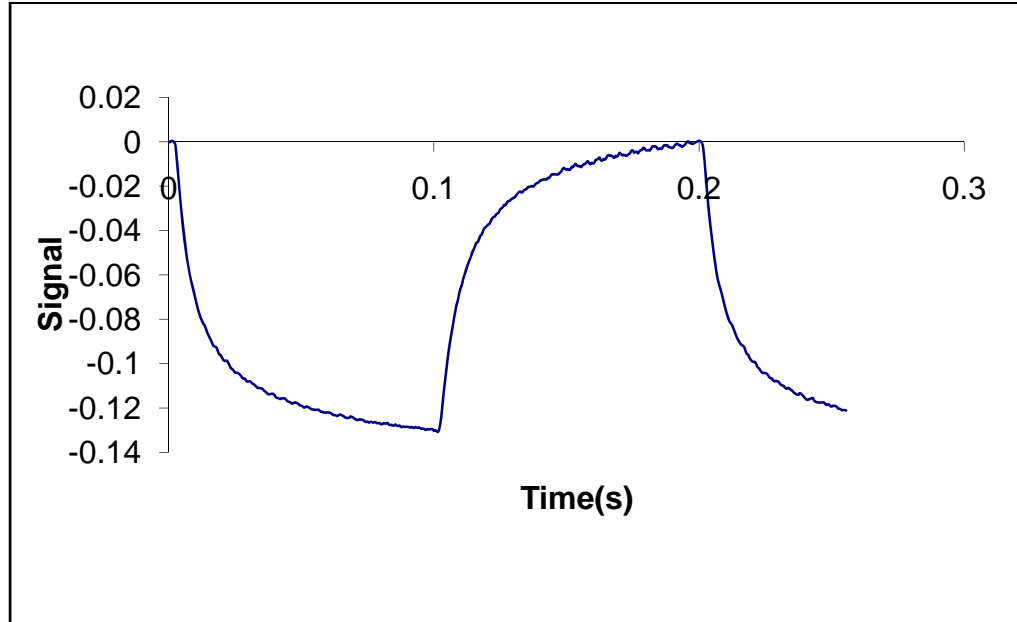


Figure 6-4. Experimental thermal lens signals for 1 mm thickness Metal-ion doped Schott NG 11 glass filter.

the glass surface and the coupling fluid, which shows another weakness in semi-infinite boundary condition normally assumed in thermal lens experiment that is not considered in this experiment. The signal versus time curve in thermal reflection and thermal deflection measurements are inverted compared to glass thermal lens signal in transmittance mode indicating expansion in the glass due to the temperature gradient and heat coupling to the surrounding.

The FEA thermal lens signals (Figure 6-5 & Figure 6-6) show a negative refractive index change in both liquid and glass which indicates ideal situations because those factors that contribute to positive refractive index change in glasses were not taken to consideration in the models.

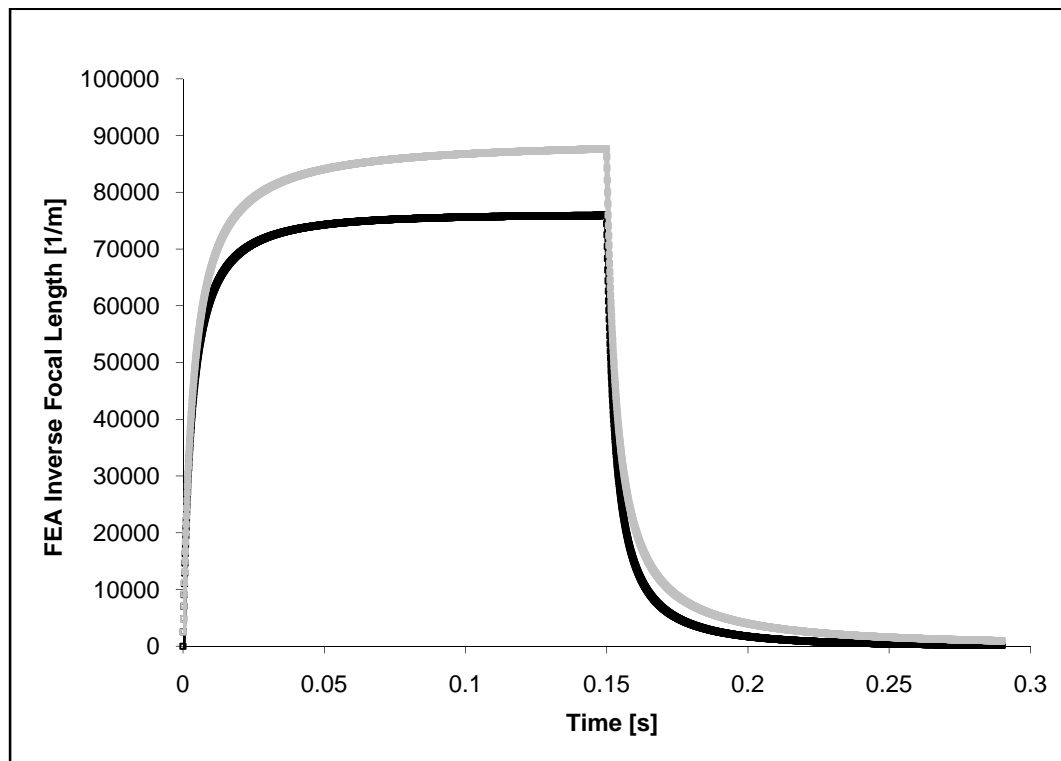


Figure 6-5. Finite element analysis thermal lens signal for (a) ♦ 5 mm thickness Corning glass CS-3-79, ♦ 1 mm thickness Schott NG 11.

The values of dn/dT for the glasses were estimated by comparing data obtained from thermal lens signals for the glasses and the well-established photothermal properties of ethanol. At steady state conditions, equation (6-3) indicates that the thermal lens signal is proportional to the integral of the second derivative of the radial temperature profile. The integration term from equation (6-3) may be obtained directly from finite element analysis modeling solution.

Corrected signal for each material was obtained by comparing the FEA signal with the experimental signal. dn/dT_g for the glasses were estimated by comparing the

corrected signals of the glasses with that of ethanol. The dn/dT_g was estimated using equation (6-8) with corrected signals.

$$\frac{dn}{dT_g} = \frac{dn}{dT_e} \frac{S_g}{S_e} \frac{k_g}{k_e} \frac{\alpha_e}{\alpha_g} \quad (6-8)$$

S is the corrected signal, subscripts *e* and *g* stand for ethanol and glass respectively. Other variables are as defined above. Table 5-1 shows the calculated dn/dT_g and the coefficient of electronic polarization, γ , for the glasses. Given β and n , from equation (6-8), electronic polarization coefficient, γ , was calculated using estimated dn/dT_g . The values of polarization coefficient are in agreement with L. Prod' homme's report on silica glasses with low expansivity. This accounts for the fact that electronic polarization is the dominant factor contributing to refractive index variation. Increase in electronic polarization causes the refractive index to increase in silica glasses.

Table 6-1. Thermo-optical constants for glass filters.

<i>Material</i>	$dn/dT \times 10^4$ (K^{-1})	$\beta \times 10^6$ (K^{-1})	<i>Refractive Index (n)</i>	$\gamma \times 10^5$
Ethanol	-4	990	1.361	
Corning CS-3-79	1.02	12	1.509	18.1
Schott NG 11	0.145	7	1.5	3.16

$dn/dT_e = -4 \times 10^{-4}$ (K^{-1}), $\kappa_g = 1.38$ ($W m^{-1} K^{-1}$), $\kappa_e = 0.167$ ($W m^{-1} K^{-1}$), $\alpha_e = 0.075$ (m^{-1}), α_g (corning) = 29.68 (m^{-1}) and α_g (schott) = 148.7 (m^{-1}).

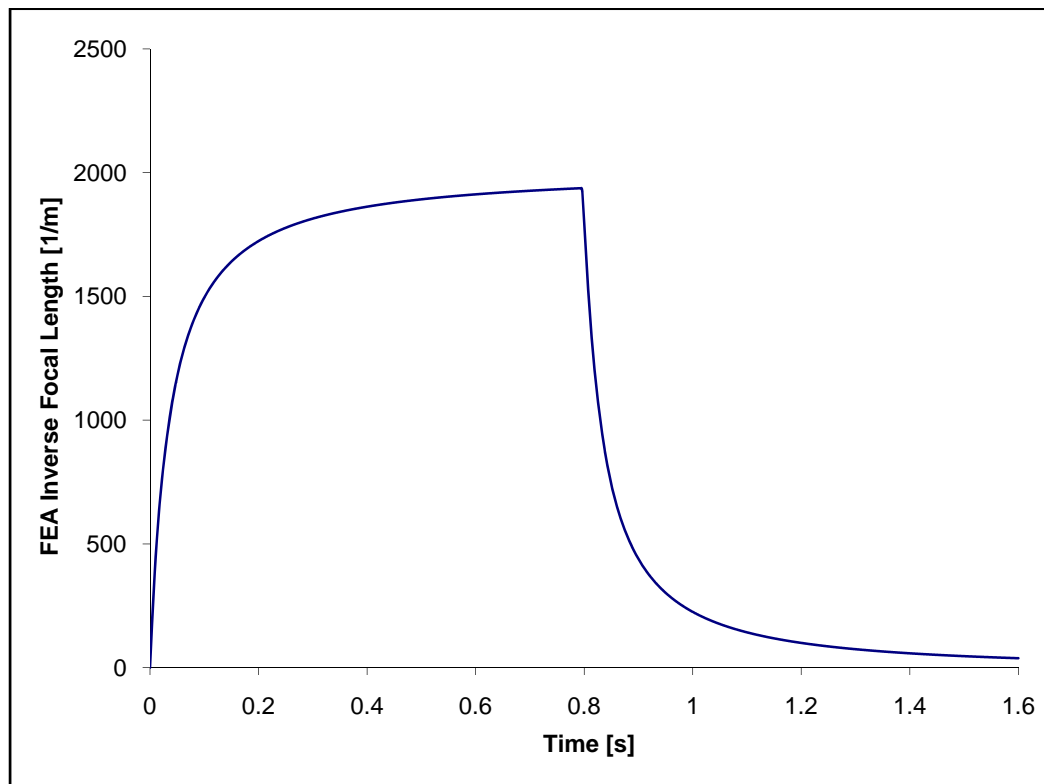


Figure 6-6. Finite element analysis thermal lens signal for ethanol in 5 mm pathlength cuvette

One of the key challenges of photothermal spectroscopy is obtaining the temperature change produced within the sample. The problem is complicated if the optical element, which is produced by refractive index change dissipates faster than change in temperature. Finite elemental analysis modeling also helps understanding the dynamics of the temperature distribution with experimental parameters such as beam waist, path length, and geometry. The results of inverse focal length as a function of excitation beam waist calculated using finite element modeling are shown in Figure 6-7. The results showed that glasses exhibit larger deviations from conventional analytical

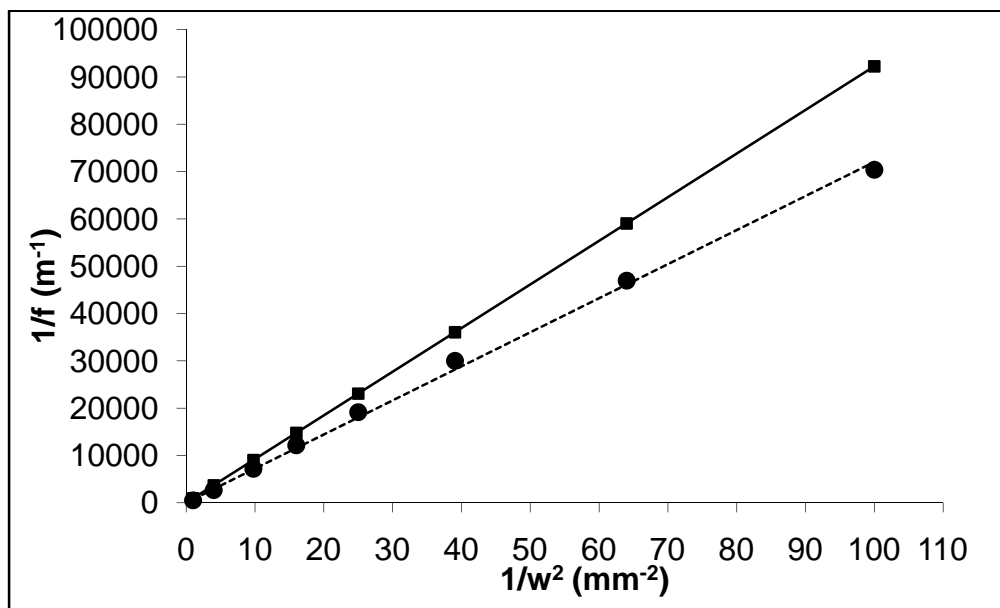


Figure 6-7. The plot of Inverse focal length versus inverse beam waist. ■ ($1/f$ Infinite Cylinder), — (Linear Infinite Cylinder), ● ($1/f$ Modeling), ----- (Linear Modeling)

solution due to direct sample-to-air contact. It is also shown that the approximation improves with increasing pathlength-to-radius ratio.

CONCLUSION

Thermal lensing measurement of commercial colored glass filters proves that the glasses may not be applicable as calibration standards for photothermal measurements since they do not produce negative lensing effect. The positive change in refractive index obtained in these glasses was initially thought to be caused by semiconductor microcrystals present in them. It turns out that this reason is not enough for the observed results because thermal lensing of other types of glasses doped with metallic colloids also

produce positive refractive index change. In addition, the results from finite element analysis models showed that the conventional semi-infinite approximation for thermal lens calculation do not hold for these glasses.

REFERENCES

1. C. J. Murphy, and J. L. Coffey, *Applied Spectroscopy* **56**, 16A (2002).
2. S. M. Lima, J. A. Sampaio, T. Catunda, A. C. Bento, L. C. M. Miranda M. L. Baesso, *Journal of Non-Crystalline Solids* **273**, 215 (2000).
3. P. Malý, F. Trojánek, and A. Svoboda, *Journal of Optical Society of America B* **10**, 1890 (1993).
4. P. Horan, and W. Blau, *Journal of Optical Society of America B* **7**, 304 (1990).
5. T. Moyo, K. Maruyama†, and H. Endo, *Journal Physical Condensed Matter* **4**, 5653 (1992).
6. F. Pereira, J. R. Salcedo, and M. Belsley, *Journal of Optical Society of America B* **16**, 228 (1999)
7. S. E. Bialkowski, *Photothermal Spectroscopy Methods for Chemical Analysis*. Wiley, New York (1996).
8. J. A. Sell, *Photothermal Investigation of Solids and Fluids*. Academic Press, New York (1989).
9. M. A. Proskurnin, and M. Y. Kononets, *Russian Chemical Review* **73**, 1143 (2004).
10. A. B. Chartier, and S. E. Bialkowski, *Optical Engineering* **36**, 303 (1997).

11. J. R. Whinnery, *Account of Chemical Research* **7**, 225 (1974).
12. S. M. Lima, J. A. Sampaio, T. Catunda, R. Lebullenger, A.C. Hernandez, M. L. Baesso, A. C. Bento, and F. C. G. Gandra, *Journal of Non-Crystalline Solids* **256**, 337 (1999).
13. M. J. Paz-Alonso, H. Michinel, and S. Bará, *Journal of Optical Society of America B* **20**, 2484 (2003).
14. L. Prod'homme. *Physics and Chemistry of Glasses* **1**, 119 (1960).
15. W. B. Jackson, N. M. Amer, A. C. Boccara, and D. Fournier, *Applied Optics* **20**, 1333 (1981).
16. M. Franko and C. D. Tran, *Review of Scientific Instruments* **67**, 1 (1996).
17. Fuxi Gan, and Fu-Hsi Kan, *Laser Materials*. World Scientific Publishing, Singapore (1995).
18. T.S. Izumitani, *Optical Glass*, American Institute of Physics, New York, (1986).
19. J. L. Coutaz and M. Kull, *Journal of Optical Society of America B* **8**, 95 (1991).
20. N. Finlayson, W. C. Banyai, C. T. Seaton, G. I. Stegeman, M. O'Neill, T. J. Cullen, and C. N. Ironside, *Journal of Optical Society of America B* **6**, 675 (1989).
21. W. D. St. John, B. Taheri, J. P. Wicksted, R. C. Powell, D. H. Blackburn, and D. C. Cranmer, *Journal of Optical Society of America B* **9**, 610 (1992).

CHAPTER 7

SUMMARY

The subject matter in this dissertation is the development of sensitive photothermal apparatus for *in situ* analysis of aerosols. First, a prototype of a small-size photothermal apparatus is constructed. The device uses no refractive focusing lens component. The prototyped apparatus produces comparable signal magnitude with conventional large size apparatus. The advantages of using short focal length optics are demonstrated in the archetypical apparatus by using short focal length aspheric focusing mirror. Predicted photothermal signals from finite element analysis modeling agree with expectation that the small apparatus should perform about the same as the conventional type. Presently, the nature and properties of off-axis parabola such as scattering, reflectivity, and asphericity are not taken into consideration. The optimum conditions for measurement have yet to be successfully obtained from experiment and in the future, sensitivity of the small apparatus will probably increase even further. There's ongoing research to test similar configuration for photothermal lens.

Second, a numerical modeling based on finite element analysis method was used to model photothermal spectroscopy of aerosols deposited on flat substrate. In order to understand how heat is transferred from aerosols to substrate and surrounding air, models of transient heat conduction through the aerosol into the substrate and the surrounding air are presented. The models compare heat transfer processes and resulting photothermal signals for low absorbance (absorption coefficient of 2676 m^{-1}) aerosols and high absorbance (absorption coefficient of $2.676 \times 10^7 \text{ m}^{-1}$) aerosols. Predicted signal show

large changes with aerosol's optical absorption coefficient, thermal properties, and inter-particle contact. The results show that the photothermal signal magnitude increases with logarithm of size for low absorbance aerosols and linearly increases with size of high absorbance aerosols. With respect to substrate's thermal properties, theoretical signal is relatively stable with heat capacity especially with high absorbance aerosols. Substrate's thermal conductivity has no effect on signal magnitude but changes signal decay time. It was also shown that increase in aerosol-substrate contact area results in decreased photothermal deflection signal. In spite of the signal reduction owing to particle-to-particle heat transfer, linear relationship with number of aerosols is still possible. CW excitation modeling results suggests substrates with low thermal conductivity as ideal for photothermal deflection.

A cross-geometry photothermal deflection version of the small configuration apparatus was then developed for aerosols analysis. The apparatus was tested with condensed-phase ammonium nitrate aerosols generated in the laboratory. Analysis of aerosols collected on flat-surface germanium disc in MOUDI impactor with non-rotating impaction plate produces higher signal with simple data analysis compared with rotating impaction plate. The sampling method, developed in our laboratory, was used to produce laboratory calibration aerosols of known size and physical-chemical properties. The pulse energy dependent signal results showed that the photothermal measurement can provide good measure of the relationship between the instrument's response and the aerosols concentration. However, the presented method does not account for multi-component aerosols that is typical of ambient samples. The limitation in resolving aerosols by

component is due to single line excitation wavelength used. Nevertheless this can be overcome by using broadband excitation wavelength or employing other methods like Confocal Raman Microscopy as a complimentary method to determine the percentage composition of multi-component aerosols.

A method for understanding thermo-optical phenomenon in thermal lens measurement of colored glass filters by applying finite element analysis is also investigated. FEA proved useful in understanding the physics of photothermal spectroscopy and validity of the conventional analytical solution used in thermal lens experiments. It was found that the conventional theoretical model used to calculate thermal lens signal is not adequate to account for the aberrant nature of results observed in glasses. Photothermal reflection measurements confirmed a positive thermal expansion when the glass is heated. The refractive index increases with temperature due to counteracting effects in the glass filters. Positive refractive index change in non-semiconductor doped glass filters can be attributed to stress-induced birefringence, structural components and electronic polarizability but the effect is complicated with semiconductor-doped glass filters due to other factors attributed to increase in carrier density of semiconductor microcrystal. “Long-lived trap states” have been proposed to account for photodarkening in $\text{CdS}_x\text{Se}_{1-x}$ –microcrystal glasses. However, it is difficult to fully understand the thermo-optical phenomenon in the glasses without prior knowledge of the properties and structural composition of the material. There is ongoing research on using finite-element model to further investigate the infinite cylinder approximation commonly used in thermal lensing measurements.

In conclusion, photothermal spectroscopy is ideal for measuring aerosols deposited on the surface of optically transparent substrate. The method is sensitive enough to detect single aerosol. The modeling results confirmed that the major difficulty in aerosol quantitation is due to the thermal interaction occurring between particles. It is not well known to what extent the heat cooperation in large sample loading will affect photothermal signal. Large sample modeling with finite element analysis may provide better information on how the signal is affected, and whether thermo-optical properties of aerosols can be determined from time-dependent signals. With analytical solution that adequately defines the signal, development of small detection system that can be replicated at low cost for wide range of aerosol detection is promising. Further studies will be required to examine whether multiple wavelength detection and multiple aerosol signals that as precise as individual aerosol measurement can be obtained.

APPENDIXES

APPENDIX A:

Figure Data

All Figure data are stored in the “MGD” media device that accompanies this dissertation.

APPENDIX B:

Dynamic Gas Mixer Operation

1. Have the analyte gas and the buffer gas ready
2. Make sure the pressure reader is properly connected to the vacuum system with no leakage
3. Prepare the gas sample cell and make sure there is no leakage
4. Connect the gas sample cell to the vacuum system output line and check if there is any leakage in the system
5. Connect the analyte gas tank to the analyte line and the buffer gas tank to the buffer line while the valves to both lines are closed
6. Then open the vacuum pump to degas the whole system
7. Close the vacuum pump when the pressure reader reads “zero”. If the pressure reader does not go back to zero then check for leakage
8. Open the analyte gas inlet while monitoring the pressure reading and fill the system with analyte gas. 100 torr recommended
9. Close the analyte gas inlet valve
10. Degas the system back to lower pressure. Note that filling and degassing the system is also filling and degassing the gas sample cell, and that the pressure of the system is the same as the pressure in the sample cell.
11. Begin gas dilution by filling the system with the buffer gas.

For example, to make 1 ppm of SO₂ gas in argon

Connect SO₂ gas source to the analyte line and argon source to the buffer line as described above.

If reading pressure with pressure gauge

1. Fill the system with SO₂ gas until the pressure gauge reads 100 torr
2. Degas the system until the pressure reads 10 torr
3. Start first dilution by filling the system with argon to return the pressure back to 100 torr. With the first dilution, the partial pressure of the analyte gas is 10% of the total gas mixture
4. Repeat steps 2 – 3 five more times to obtain 1 ppm of the analyte gas.

If reading pressure with voltmeter, make sure the equivalent pressure per volt is known.

Then run steps 1 – 4.

EnviroNics gas mixer, series 4000.

1. Connect gas cylinders to the appropriate port. Port 4 recommended for the gas of interest. Note the following MFC for each port:
1 – 5000, 2 – 2500, 3 – 500, 4 - 100
2. Turn on the instrument and refer to the user manual to configure gas library, ports, cylinders, and the instrument.
3. Run the instrument in the desired mode

APPENDIX C:

Comsol Multiphysics Files

Comsol Multiphysics files for finite element analysis modeling and AVI files for the temperature change animation results from Chapter 3 are stored in the “MGD” media device that accompanies this dissertation.

APPENDIX D:

Step-by step Procedure for Aerosol Generation

Make sure the apparatuses are properly setup as described in Chapter 4.

1. Prepare a stock solution of the compound to be produced with known concentration. Note that the concentration will also determine the amount of aerosols generated
2. Put a portion of the stock solution (25 – 40 mL recommended) in the atomizer and make sure the liquid level is below the atomizing nozzles
3. Open the dilution gas (air) and adjust the flow rate to the desired level
4. Open the nebulizing gas to start the atomizer (15 – 20 psi atomizer pressure recommended)
5. Allow the system to run for about 30 minutes for equilibration
6. Connect the impactor to the sampling port on the slow flow tube and adjust the impactor inlet flow rate to 30 L/min for standard operation. Note that other flow rate will require particle size calibration
7. Prepare and weigh the collection plate
8. Insert the collection plate into the impactor stage where aerosols are to be collected
9. Decide whether to operate the impactor with rotating plate or non-rotating plate (this is only applicable to impactors that have gear to rotate the plates)

10. Turn on the impactor power to start rotation if it has one
11. Turn on the vacuum system/pump to start collecting aerosols and be sure to monitor the collection time
12. Stop the vacuum system and the impactor to stop collection
13. Remove and weigh the loaded plate
14. Calculate aerosol mass loading by subtracting the mass of plate before loading from the mass after loading
15. Aerosol mass concentration is calculated as

$$\frac{\text{Mass loading (g)}}{\text{Impactor flow rate (m}^3\text{/min) x collection time}}$$

For example:

If the mass of plate before loading is M_1 and the mass of plate after loading is M_2 ,

For 30 minutes collection time and 30 L/min impactor flow rate

Aerosol mass concentration is calculated as

$$\frac{(M_2 - M_1) \times 1000}{30 \times 30}$$

APPENDIX E:

Permission Letters

Society for Applied Spectroscopy – Copyright Permission

From: "Oluwatosin" <oluwatosinusu@yahoo.co.uk>
 Subject: Permission to reprint applied spect. publication
 Date: Mon, March 3, 2008 6:07 pm
 To: exdir@s-a-s.org

Dear Bonnie Saylor,

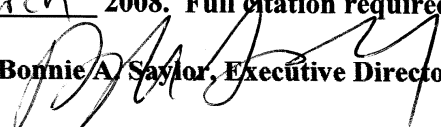
I am in the process of preparing my dissertation in the Chemistry and Biochemistry department at Utah State University. It is expected to be completed by the end of spring, 2008. I am writing to request SAS permission to include the manuscript of my paper entitle "Continuous Laser-Excited Photothermal Spectrometry of CdSxSe1-x Doped Glasses" in its entirety in my dissertation. The paper was published in Applied Spectroscopy Volume 61, Number 12, 2007. In addition a copy of the permission letter shall be printed in an Appendix to my dissertation.

I will be happy to answer any question or request regarding this letter.

Thank you for your consideration

**Permission granted for the use requested above:
 Permission granted this 10th day of
March 2008. Full citation required.**

SAS Bonnie A. Saylor, Executive Director



Oluwatosin Dada
 Department of Chemistry & Biochemistry
 Utah State University
 Logan, UT. 84322-0300

Attachments:

untitled-2	
Size:	4.6 k
Type:	text/html

Co – author permission

03 March 2008

Mr. Mathew R. Jorgensen
University of Utah
Department of Chemistry
315 So. 1400 E. Rm. 2020
Salt Lake City, Utah 84112-0850

Oluwatosin Dada
Utah State University
Dept. of Chemistry and Biochemistry
Logan, Utah 84322-0300

Dear Mr. Jorgensen,

I am in the process of preparing my dissertation in the Chemistry and Biochemistry department at Utah State University, which is expected to be completed by the end of spring, 2008.

You were a co-author with me on the manuscript entitled “Continuous Laser-Excited Photothermal Spectrometry of CdS_xSe_{1-x} Doped Glasses”. I am writing to request your permission to include the manuscript in its entirety in my dissertation. I will include acknowledgement of your contributions as an author to this manuscript as part of a footnote on the page for that chapter. In addition, a copy of this letter will be printed in an Appendix to my dissertation.

Please indicate your approval of this request by signing the endorsement below. I will be happy to answer any question or special request regarding this letter.

Thank you for your time and consideration.

Oluwatosin Dada

I hereby give my permission to Oluwatosin Dada to reprint the manuscript entitled “Continuous Laser-Excited Photothermal Spectrometry of CdS_xSe_{1-x} Doped Glasses”, co-authored by Mathew R. Jorgensen, and Stephen E. Bialkowski.

Signed Mathew R. Jorgensen

Date 3/11/2008

CURRICULUM VITAE

Oluwatosin Olubunmi Dada

Utah State University

Department of Chemistry and Biochemistry

Logan, Utah. 84322-0300

PROFESSIONAL STATUS: PhD Analytical Chemistry**PHONE:** 435-764-7464**EMAIL:** Oluwatosin@cc.usu.edu**AREAS OF INTEREST**

- Atmospheric Environmental Chemistry and Analysis
- Photothermal Spectroscopy
- Raman Spectroscopy
- Fluorescence Spectroscopy
- Infrared Absorption and Emission Spectroscopy
- GC and HPLC
- Gas-Phase Chemical Analysis
- Nanostructure materials

EDUCATION

- B. S., Industrial Chemistry, Olabisi Onabanjo University, Nigeria, 2001
- Ph. D., Analytical Chemistry, Utah State University, May 2008

PROFESSIONAL EXPERIENCE**Teaching Experience**

- Teaching Assistant, Utah State University, 2007-Present

- Teaching Assistant, Utah State University, 2004-2005

Research Experience

- Research Assistant, Utah State University, 2005-2007

Industrial Experience

- Chemist, West African Distillers Limited, Nigeria, 2001-2004
- Laboratory Technician, Eagle Paints Nigeria, 1999-2000

COMPUTATIONAL SKILLS

- Comsol Multiphysics (Finite element analysis modeling software)
- Code V (Optical design software)
- NCSS and SPSS (Statistical software)

PROFESSIONAL SOCIETY AFFILIATIONS

- Society for Applied Spectroscopy (SAS)
- American Chemical Society (ACS)
- American Association for the Advancement of Science (AAAS)

AWARDS

- Chemistry best student award, 2001
- School of Graduate Studies Honor Roll, 2005
- Federation of Analytical Chemistry and Spectroscopy Societies (FACSS 2007)
Outstanding Student Postal Presentation Award, 2007

PUBLICATIONS

- *Continuous laser-excited photothermal spectrometry of CdS_xSe_{1-x} doped glasses*, Oluwatosin O. Dada, Mathew Jorgensen, and Stephen E. Bialkowski. ***Applied Spectroscopy***, **61**(12), 1373, 2007.
- *Finite element modeling of pulse-laser excited mirage effect from condensed-phase aerosols*, Oluwatosin O. Dada and Stephen E. Bialkowski. **Accepted in *Applied Spectroscopy***

- *Development of infrared photothermal deflection spectroscopy (mirage effect) for condensed-phase aerosols collected in a micro-orifice uniform deposit impactor*, Oluwatosin O. Dada and Stephen E. Bialkowski. **Accepted in Applied Spectroscopy**

SCIENTIFIC MEETINGS AND PRESENTATIONS

- *Analysis of Condensed-Phase Aerosols Using Infrared Photothermal Spectroscopy with Optical Beam Deflection (Mirage Effects)*. Oluwatosin O. Dada and Stephen E. Bialkowski. **Federation of Analytical Chemistry and Spectroscopy Societies, Memphis, TN, 2007.**
- *Photothermal Deflection Spectrometry (Mirage Effect) of Condensed-Phase Aerosols*, Oluwatosin O. Dada, **Graduate Student Symposium, Utah State University. 2006.**